UNIVERSIDAD DE CONCEPCIÓN
DIRECCIÓN DE POSTGRADO
FACULTAD DE INGENIERÍA - PROGRAMA DE DOCTORADO EN CIENCIAS DE LA INGENIERÍA CON MENCIÓN EN INGENIERÍA QUÍMICA

HYDRODYNAMICS OF CAPILLARY IMBIBITION AT NANOSCALE

NABIN KUMAR KARNA
CONCEPCION - CHILE 2018

Tesis para optar al grado de Doctor en Ciencias de la Ingeniería con mención en Ingeniería Química

Tutor: Dr. Harvey A. Zambrano
Departamento de Ingeniería Química
Facultad de Ingeniería - Universidad de Concepción

Co-tutor: Dr. Jens H. Walther
Departament of Mechanical Engineering
Technical University of Denmark

Advisor : Dr. Harvey A. Zambrano

Co-advisor : Dr. Jens H. Walther

Examination Committee : Dr. Andés Mejía M.
: Dr. Roberto E. Rozas Cárdenas

"The eternal time factor has no beginning and no end. It is the representative of the Supreme Personality of Godhead. It creates the universe .. and likewise it dissolves the universe ..."

Shrimad Bhagavat Gita (3:29:45)

Abstract

The reduced length scale comparable to molecular dimensions at nanoscale flows, lead to several non-intuitive and fascinating phenomena not seen in classical hydrodynamics. Water is a polar liquid and despite being the most studied liquid, its properties remain mysterious as the characteristic length scale approaches the nano and molecular scales, which introduces further complications in describing nano flow related phenomena like capillary imbibition of nanochannels and nanopores. Capillary imbibition is ubiquitous in nature and has recieved wide spread attention due to its implications in many natural and technologial processes. Capillary forces and related process of liquid imbibition that occur at nanoscale are critical for a wide range of applications like lab-on-a-chip units, precise drug delivery and inkjet printing etc. The better understanding and further development of these novel applications need a detailed knowledge of the surface effects and interfacial interactions which strongly influence the behavior of the fluids at nanoscale, and hence widely known macroscopic theories of flow and mass transport phenomena cannot capture the hydrodynamics at this scale. In relation to this, researchers lack consensus on the explanation of several fundamental aspects like the early effects during the capillary imbibition like the momentum balance of the imbibing fluid, the dynamics of the development of meniscus contact angle, and the filling kinetics during the capillary imbibition in nanoconfinement. Hence, this work aims to contribute to the better understanding and provide explanations to the fundamental aspects of the early stage of capillary filling in nanochannels, as a comprehensive understanding to these phenomena is crucial to design and improve various existing and future nano-devices. The precise control over fluid steering and retention, over these scales, can form the basis for several applications related to efficient fluid transport, mixing of species in nanoconfinement, ultra precise drug delivery and energy conversion and harvesting. Taking this into account, we study the effect of an external electric field in nanocapillary flow of water. Our results suggest that the nanocapillary flow control is possible through changes in solid-liquid interfacial friction and viscosity of water molecules under the influence of external electric field. Most of the fluid transported in biological systems and nanofluidic devices involves electrolyte solutions which adds further complication to understand the physics behind the process and exploit it for technological applications. To address the contribution of type and concentration of ions during nanocapillary imbibition, we study the capillary filling of mono and multivalent ions at different concentrations in nanochannels at zero net charge on the walls. Our results indicate that the capillary filling of electrolyte solutions inside hydrophilic silica nanochannels is governed by the enhanced viscosity of the imbibing solution due to electroviscous effect that depends directly upon the nature and valency of cations. In this study, we develop comprehensive theoretical understanding of the nanocapillary fluid dynamics in hydrophilic channels and its implications that provides a route for futuristic experimental studies. The main contribution of this work will be the better understanding of nanocapillary imbibition at molecular level which has not been possible till now and propose a possible mechanism for flow control during imbibition process.

Acknowledgements

This dissertation is the result of my research work carried out in the Department of Chemical Engineering at University of Concepcion during the period March 2014 to August 2018, under the supervision of Associate Professor Harvey A. Zambrano and co-supervision of Professor Jens H. Walther.

First and foremost, I express my deepest gratitude to my supervisor Dr. Harvey A. Zambrano, who apart from being a great scholar, is an exceptional human being. I consider myself tremendously fortunate to have a teacher and advisor like him. The execution of this work would have been impossible without his contributions in the scientific discussions, and guidance during this period. He has always inspired me to explore my ideas freely, continuosly providing me with constructive comments, and have influenced my outlook in the years to come. His continuous support and patience helped me overcome many overwhelming challenges.

I would like to express my sincerest regards to Professor Jens H. Walther, who inspite of his busy schedule always supported through his guidance and permanent scientific discussions.

I sincerely express my heartfelt gratitude to Dr. Alex Berg for his emotional and moral support during the entire work and for influencing my approach to the scientific methods and philosophy. His ideas have shaped my ideosyncracy to deal with the problems in every aspect of my life.

I was extremely fortunate to join my friends: Elton, Enrique, Andres and Diego, in Computational Nanolab and am deeply thankful for their help and high quality scientific and non-scientific debates. I also express my sincere thanks to my colleagues from other research groups for all the academic and non-academic interactions. I express my gratitude to my all-weather friend Luis Pino Soto for supporting me throughout and for being such an honest critic.

I am eternally indebted to Ms. Olda Ortiz Santos for her love, patience, motivation and company during the bad and worse times.

This work was partially funded by CONICYT under the scholarship no. 21140427. I also thank computational support from Danish Center for Scientific Computing (DCSC), Denmark and from National Laboratory for High Performance Computing (NLHPC), Chile.

I acknowledge the help and assistance provided by the Professors of the Department of Chemical Engineering during my research work. I also place on record, my sense of gratitude to all, who directly or indirectly, are related to this journey.

University of Concepcion
Faculty of Engineering
Department of Chemical Engineering
August, 2018
Nabin K. Karna

Contents

Abstract **vii**

Acknowledgements **ix**

1 Introduction **1**
1.1 Outline 1
1.2 Hypotheses 3
1.3 Objectives 3
1.3.1 General Objective 3
1.3.2 Specific Objectives 3

2 Fundamental Theory and Literature Survey **5**
2.1 Basic Principles 5
2.1.1 Surface tension and Young's condition 5
2.1.2 Capillary pressure 6
2.1.3 Capillarity 7
2.1.4 Capillary imbibition in parallel plate 8
2.1.5 Different regimes of capillary filling 9
Viscous or Washburn's regime 9
Viscoinertial regime 11
Szekely's energy balance equation 11
Time demarkation of different regimes 12
Preinertial filling and energy loss at the entrance 13
Dynamic contact angle 13
Thermodynamic approach 14
2.1.6 Nanocapillary Imbibition 15
2.1.7 Influence of electric field in nanoflows 16
Effect of electric field in nanosized water droplets 16
Effect of electric field on flows in nanochannels 18
2.1.8 Influence of ions types on flows in nanochannels 19

3 Molecular Simulations **21**
3.1 Outline 21
3.1.1 Concept of ensembles 21
3.1.2 Molecular interactions 23
Bonded interactions 23
Non-bonded interactions 24
3.1.3 Neighbor list and Cut-off radius 25
Ewald Summation Method 27
3.1.4 Ewald methods based on Fast Fourier Transform (FFT) . . . 29
Particle-Mesh Ewald (PME) 29
3.1.5 Thermostats 30
Berendsen thermostat 31

3.1.6 Periodic Boundary Condition(PBC) 32
3.1.7 Initial Configuration 33
3.1.8 Constraint methodologies 33

4 Effect of the meniscus contact angle during early regimes of spontaneous imbibition in nanochannels 35
4.1 Outline 35
4.2 Introduction 35
4.3 Simulation details 38
4.4 Results and Discussions 39
4.5 Conclusions 42

5 Capillary imbibition of electrolyte solutions in hydrophilic silica nanochannels at point of zero charge 43
5.1 Outline 43
5.2 Introduction 43
5.3 Simulation methods 45
5.3.1 Water contact angle measurement 47
5.3.2 Imbibition of electrolyte solutions in capillary channel . . . 47
5.3.3 Surface tension measurement 48
5.3.4 Viscosity measurement 48
5.4 Results and Discussion 49
5.4.1 Nanocapillary imbibition of the electrolyte solutions 49
Radial Distribution Function 50
5.4.2 Effects of ions on viscosity of electrolyte solution 56
5.4.3 Effect of ion on the surface tension of electrolyte solution . . 58
5.4.4 Effect of ion on equilibrium contact angles made by electrolyte solutions on an amorphous hydrophilic silica slab . . 59
5.4.5 Effect of ions on the nanocapillary imbibition of electrolyte solutions into a hydrophilic silica channel 61
5.5 Conclusions 63

6 Effect of external electric fields on capillary imbibition of water in silica nanochannels 67
6.1 Outlines 67
6.2 Introduction 67
6.3 Computational method 70
6.4 Results and discussion 70
6.5 Conclusions 80

7 Concluding remarks and scope of future work 81
7.1 Summary of the major findings 81
7.2 Hypothesis validation 82
7.3 Scope of future work 82

A Supporting Information for Chapter 4. 83
A.1 Interaction potentials used in the study 83
A.2 Measurement of surface tension of fluids 84
Energy analysis of surface tension 85

B Supporting Information for Chapter 5. 87

B.1 S1. Types and concentration of ions used to study the nanocapillary imbibition in hydrophilic silica nanochannel 87

B.2 S2. Silica interaction parameters used for the amorphization of silica slabs 87

B.3 Lorentz-Berthelot mixing rule 87

B.4 Filling kinetics of water-electrolyte systems in hydrophilic silica nanochannel 90

B.5 Radial distribution functions of water-electrolyte systems 94

B.6 Orientation distribution functions of water around ions in their respective solutions 97

B.7 Viscosity of electrolyte solutions at different concentrations 98

B.8 Surface tension of electrolyte-ion systems at different concentrations 100

C Supporting Information for Chapter 6. 105

C.1 S1. Average velocity during the viscous regime during nanocapillary imbibition in amorphous silica channels 105

C.2 S2. Orientation distribution of angle between the water dipole vector and the vector normal to the silica surface at different distance from the silica-wall for case without applied electric field 106

C.3 S3.Orientation distribution of the angle between the vector normal to the silica wall and the vector joining the two hydrogen bonds for different applied field strength. 106

C.4 S4. Orientation distribution of angle between the water dipole vector and the vector normal to the silica surface distance between 0-0.5 nm from the silica-wall for different applied electric field 108

List of Figures

2.1 Mechanical definition of surface tension. Source: Own elaboration. 5
2.2 Formation of equilibrium contact angle on a solid surface. Source: Own elaboration. 6
2.3 A schematic diagram showing a differential increase in drop size due to pressure difference. Source: Own elaboration. 7
2.4 Capillary rise in cylindrical tubes of varying radius. Source: Own elaboration. 8
2.5 Dimensionless diagram showing an overview of the initial time stages of capillary rise. Source: Fries et al.[97] 13
2.6 Skematic diagram of electrical double layer at the vicinity of a surface wall. Source: Brown et al.[40] 20

3.1 Lennard Jones potential and its components. Source: Own elaboration. 25
3.2 The Verlet list on its construction, later, and too late. The solid line represents r_{cut} and the dotted line r_{list}. The potential cut-off range (solid circle), and the list range (dashed circle), are indicated. The list must be reconstructed before particles originally outside the list range (black) have penetrated the potential cut-off sphere. Source: Allen et al.[7] 26
3.3 Treatment of electrostatic interaction using Ewald summation method. Source: Berendsen et al.[23] 28
3.4 A conceptual representation of periodic boundary condition. Source: Berendsen et al.[23] 32

4.1 A snapshot of the capillary filling for a 6nm silica nanochannel. Source: Own elaboration. 37
4.2 Nanocapillary imbibition length as a function of time for different height of capillaries.The black dots represent the imbibition length as a function of time. The straight yellow dashed lines are visual guides to indicate the $l(t) = A_I t$, which also illustrate estimated times of inertial regime. The solid lines depict the fits of modified Bosanquet's equation to the experimental data. The colored dotted lines are visual guide lines to indicate the original Bosanquet's equation. Source: Own elaboration. 38
4.3 Measured contact angles (dotted lines) and those predicted by the model (solid lines) during the nanocapillary imbibition in silica nanochannels of different heights. The red, green,blue, pink and cyan lines represent the contact angles for 4, 6, 10, 14 and 18 nm channels respectively. Source: Own elaboration. 40
4.4 Calculated values of the constants as a function of channel height (H). The dotted lines represent linear fits while the coloured dots are the measured values. Source: Own elaboration. 41

5.1 A snapshot of the capillary filling for 6-nm silica nanochannel. In the above figure, H refers to the height of the channel while $l(t)$ is the time dependent filling length. Source: Own elaboration. 45
5.2 A snapshot of the contact angle measurement on a hydrophilic silica slab. Source: Own elaboration. 47
5.3 Capillary filling of 1.0 molar electrolyte solutions in a 6nm wide hydrophilic silica channel. Source: Own elaboration. 49
5.4 Capillary filling of different concentrations of $MgCl_2$ in a 6nm wide hydrophilic silica channel. Source: Own elaboration. 50
5.5 Radial distribution functions of Li^+-OW (left) and Na^+-OW (right). Source: Own elaboration. 51
5.6 Radial distribution functions of K^+-OW (left) and Mg^{2+}-OW (right). Source: Own elaboration. 51
5.7 Radial distribution functions of Ca^{2+}-OW (left) and Ba^{2+}-OW (right). Source: Own elaboration. 52
5.8 Radial distribution functions of Al^{3+}-OW (left) and Cl^--OW (right). Source: Own elaboration. 52
5.9 The angles considered to determine the orientation of the water molecules around specific ions. Source: Own elaboration. 54
5.10 Normalized angular distribution function of water dipoles around the ions used in this study. Source: Own elaboration. 55
5.11 Potential energy between ion-water for different concentrations for the electrolyte solutions under study. Source: Own elaboration. . . 55
5.12 Viscosity of the electrolyte solutions at different concentrations. The viscosity values are scaled with respect to the viscosity of pure water at 298 K. Source: Own elaboration. 57
5.13 Surface tensions of different electrolyte solutions at varied concentration under study at 300 K. Source: Own elaboration. 58
5.14 Contact angles of electrolyte solutions in relation to the concentration on a hydrophilic silica slab.Source: Own elaboration. 60
5.15 Interaction energy of the electrolyte solutions with the hydrophilic silica slab in relation to the concentration on a hydrophilic silica slab. Source: Own elaboration. 60
5.16 Cohesive potential energy of the electrolyte solutions in relation to the concentration on a hydrophilic silica slab. Source: Own elaboration. 61
5.17 Comparison of simulation data of capillary filling in a 6 nm wide hydrophilic silica nanochannel with that predicted by Bosanquet's model for LiCl solutions. BV refers to the Bosanquet's initial velocity at the channel entrance. The solid filled dotted lines are those predicted by the modified[159] Bosanquet's model[35], while the solid colored lines are simulation data. The dashed lines correspond to a linear regression in the constant velocity regime. Source: Own elaboration. 62

6.1 A snapshot of capillary filling for 7-nm silica nanochannel. The electric field (E) is applied in the direction of nanocapillary imbibition. Source: Own elaboration. 68
6.2 Water contact angle (WCA) on a hydrophilic silica slab at different electric field strength. The electric field is applied parallel to the surface. Source: Own elaboration. 71

6.3 Scaled viscosity calculated from the Periodic perturbation method at different electric fields. The dotted lines represent the linear tendency of the change in viscosity while the points are the measured values. Source: Own elaboration. 72
6.4 Nanocapillary imbibition length as a function of time in a 7 nm-high channel for different strength of electric field. The constant filling rates for all the cases of electric field indicates an inertial regime independent of initial conditions. Source: Own elaboration. 73
6.5 Measured dynamic contact angle (DCA) in a 7 nm-high channel at various electric field strengths. Source: Own elaboration. 73
6.6 Velocity profile of Poiseuille flow for a slit silica channel with height of 7 nm at different applied field strengths. The maximum velocity computed at the center of the channel decreases with increasing applied field strength. Source: Own elaboration. 75
6.7 The angles considered to determine the orientation of the water molecules are given in terms of the angles α_1 and α_2. ν_d,ν_n and ν_{HH} are the vectors corresponding to the dipole moment, normal to the surface and that connecting the two hydrogen atoms, respectively. Source: Own elaboration. 76
6.8 Probability distribution function of water dipole moment at a distance between 1.5–2.0 nm from the lower wall surface. Source: Own elaboration. 77
6.9 Coefficient of self-diffusion of water along channel width. The solid line represents the density of water and the dots with error bars represent the scaled self-diffusion coefficient of water calculated using the Stokes-Einstein relation. Source: Own elaboration. 78
6.10 Interfacial friction coefficient in water-silica interface under different external electric fields. Source: Own elaboration 80

A.1 A snapshot of the slab of the system used to calculate the surface tension of the electrolyte solutions. Source: Own elaboration. 85

B.1 Filling kinetics of 0.2M electrolyte system in silica-nanochannel. Source: Own elaboration. 90
B.2 Filling kinetics of 0.4M electrolyte system in silica-nanochannel. Source: Own elaboration. 90
B.3 Filling kinetics of 0.6M electrolyte system in silica-nanochannel. Source: Own elaboration. 91
B.4 Filling kinetics of 0.8M electrolyte system in silica-nanochannel. Source: Own elaboration. 91
B.5 Filling kinetics of LiCl solution in silica-nanochannel. The solid lines are fit of Bosanquet's equation, while the straight dotted line is the fit of initial velocity. Source: Own elaboration. 92
B.6 Filling kinetics of NaCl solution in silica-nanochannel. The solid lines are fit of Bosanquet's equation, while the straight dotted line is the fit of initial velocity. Source: Own elaboration. 92
B.7 Filling kinetics of KCl solution in silica-nanochannel. The solid lines are fit of Bosanquet's equation, while the straight dotted line is the fit of initial velocity. Source: Own elaboration. 93

B.8 Filling kinetics of $MgCl_2$ solution in silica-nanochannel. The solid lines are fit of Bosanquet's equation, while the straight dotted line is the fit of initial velocity. Source: Own elaboration. 93
B.9 Radial distribution functions of Li^+-OW (left) and Na^+-OW (right). Source: Own elaboration. 94
B.10 Radial distribution functions of K^+-OW (left) and Mg^{2+}-OW (right). Source: Own elaboration. 94
B.11 Radial distribution functions of Ca^{2+}-OW (left) and Ba^{2+}-OW (right). Source: Own elaboration. 95
B.12 Radial distribution functions of Al^{3+}-OW (left) and Cl^--OW (right). Source: Own elaboration. 95
B.13 The angles considered to determine the orientation of the water molecules around specific ions. Source: Own elaboration. 97
B.14 Probability distribution function of water dipoles around the ions used in this study. Source: Own elaboration. 97
B.15 Potential energy between ion-water for different concentrations for the electrolyte solutions under study. Source: Own elaboration. . . 98
B.16 Number of hydrogen bonds in electrolytic solutions in relation to the concentration. Source: Own elaboration. 100
B.17 Densities of the anions and cations of the systems under study along the direction perpendicular to film. Source: Own elaboration. . . . 101
B.18 Number of interfacial hydrogen bonds in electrolytic solutions in relation to the concentration. Source: Own elaboration. 102
B.19 Interaction energy of the electrolyte solutions with the hydrophilic silica slab in relation to the concentration on a hydrophilic silica slab. Source: Own elaboration. 102
B.20 Cohesive potential energy of the electrolyte solutions in relation to the concentration on a hydrophilic silica slab. Source: Own elaboration. 103

C.1 Average velocity during the viscous regime during the nanocapillary imbibition at different electric field strength applied parallel to the flow direction.The dotted lines represents the tendency of monotonic decrease of the maximum velocity observed during the process. Source: Own elaboration. 105
C.2 Distribution function of angle between the water dipole and the normal to the silica wall for case without applied electric field. Source: Own elaboration. 106
C.3 Orientation distribution function of the angle between the vector normal to the silica wall and the vector joining the two hydrogen bonds for different applied field strength. This function is calculated at a distance between 1.5–2.0 nm from the lower wall surface. Source: Own elaboration. 107
C.4 Distribution function of angle between the water dipole and the normal to the silica wall for different applied electric field at a distance between 0-0.5 nm from the silica surface. Source: Own elaboration. 108

List of Tables

4.1 Configurational details of water imbibition in silica nanochannels. H is the channel height, channel length was kept constant to 31.6 nm in all the cases . . . 39
4.2 Values of parameters during initial rise. E_v is the estimated value of velocity using the modified Bosanquet's equation, similarly, C_v is the calculated velocity. t_i is the inertial time period while, τ is the adjusting parameter given by equation 4.6. . . . 42

5.1 Salts and their concentrations used to study the nanocapillary imbibition in hydrophilic silica nanochannel. . . . 45
5.2 Interaction parameters for the electrolytes used in the study. (Si-Silicon, O - Oxygen, Li - Lithium, Na - Sodium, K - Potassium, Mg - Magnesium, Ca - Calcium, Ba - Barium, Al - Alumunium, Cl - Chloride ion) . . . 46
5.3 Comparison of characteristic peak values and positions of the ions in water at 300 K. . . . 53
5.4 Total interaction energy (kJ/mol) between ion- water pair in the first solvation shell at 300 K. . . . 54
5.5 Distance (nm) between the hydrogen atoms of the first shell and the adjacent oxygen molecules in the bulk at 300 K. . . . 56
5.6 Values of the important parameters during initial rise . . . 64

6.1 Parameters of equation 6.6 under different magnitudes of electric field at 300 K . . . 78

A.1 Silica-silica interaction parameters. . . . 83
A.2 Silica-water interaction parameters. . . . 84

B.1 Salts and their concentrations used to study the nanocapillary imbibition in hydrophilic silica nanochannel. . . . 87
B.2 Silica-silica interaction parameters. . . . 87
B.3 Interaction parameters for the electrolytes used in the study. . . . 88
B.4 Comparison of characteristic peak values and positions of the ions in water at 300 K. Source: Own elaboration. . . . 96
B.5 Total interaction energy (kJ/mol) between ion- water pair in the first solvation shell at 300 K. Source: Own elaboration. . . . 98
B.6 Distance (nm) between the hydrogen atoms of the first shell and the adjacent oxygen molecules in the bulk at 300 K. Source: Own elaboration. . . . 98
B.7 Viscosity of various electrolyte solutions at different concentrations at 300K . . . 99

List of Abbreviations

LAH	**L**ist **A**bbreviations **H**ere
Ca	**Ca**pillary number
EDL	**E**lectrical **D**ouble **Layer**
YL	**Y**oung-**L**aplace
WCA	**W**ater **C**ontact **Angle**
DCA	**D**ynamic **C**ontact **Angle**
MKT	**M**olecular **K**inetic **T**heory
LOC	**L**ab-**O**n-a-**C**hip
LJ	**L**ennard-**J**ones
MD	**M**olecular **D**ynamics
SPC/E	**S**imple **P**oint **C**harge **E**xtended
K.E	**K**inetic **E**nergy
P.E	**P**otential **E**nergy
SI	**S**upporting **I**nformation

Physical Constants

Speed of Light	$c_0 = 2.997\,924\,58 \times 10^{8}\,\mathrm{m\,s^{-1}}$ (exact)
Boltzmann constant	$k_B = 1.380\,648\,52 \times 10^{-23}\,\mathrm{m^2kgs^{-2}K^{-1}}$
Avogadro's constant	$N_A = 6.022\,140\,9 \times 10^{23}\,\mathrm{mol^{-1}}$
Acceleration due to gravity	$g = 9.82\,\mathrm{ms^{-2}}$

List of Symbols

γ	surface tension	N/m
v	velocity	$\mathrm{m\,s^{-1}}$
μ	viscosity	Pa s
μ_c	chemical potential	$\mathrm{Jkg^{-1}}$
λ_0	Equilibrium displacement frequency	Hz
θ_e	Equilibrium contact angle	°
θ_D	Dynamic contact angle	°
κ	Isothermal compressibility	$\mathrm{Pa^{-1}}$
T	Temperature	K
P	Pressure	$\mathrm{Nm^{-2}}$
F_f	Frictional force	$\mathrm{Nsm^{-3}}$
E	Energy	J
U	Potential Energy	J
M	Mass	kg
N	Number of particles	
u	Initial velocity	$\mathrm{ms^{-1}}$

Dedicated to Alex Berg for influencing my approach to life ...

Chapter 1

Introduction

1.1 Outline

Nanofluidics is the study of phenomena that involve fluid motion through or past structures with features that measure less than 100 nm in one or more directions.[84] Recent development of nanodevices and foreseeable applications in different biological and technological scenarios have led to intensive research in this new field particularly during the last two decades. The main drivers of research in nanofluidics are: 1) rapid evolution of nanobiotechnology and the interest in precise drug delivery 2) advances in nanofabrication techniques, interest in further miniaturization of microscale devices like Lab-on-a-Chip units, development of nanosensor technology, improvement in inkjet printing 3) the availability of new tools to investigate and describe fluid behavior at nanoscale, which allow continuum descriptions to be combined with molecular dynamics descriptions in multiscale simulation approaches of realistic devices, and the prediction of new phenomena at sub-nanometer length scale.[124] Capillary imbibition at nanoscale environments plays a crucial role for phenomena ranging from clay swelling, frost heave, and oil recovery to colloidal stability, protein folding, and transport in cells and tissues. Capillarity can be used to transport fluid at the expense of surface energy through channels, where other forms of mechanical or automatic actuation are not feasible. Molecular interactions at fluid-wall interface become important in nanofluidics because of the large surface-to-volume ratios found in these systems.[273] During nanocapillarity, the deviation from the bulk properties induced by the presence of surfaces confining ultra small amounts of fluid leads to deviation in boundary conditions at the interface accounting for the molecular flow. The familiar no-slip boundary condition of continuum hydrodynamics might be replaced by slip[321], multilayer sticking[113] or intermittent stick slip boundary conditions. Predicting the flow behavior by using classical Navier-Stokes equations[296] at nanoscale is not possible as the steric effects and the thermal fluctuations of the molecules become comparable to the size of the system due to which systematic distortions in the macroscopic physical properties like viscosity and density can be observed.[51,189] There is a large number of scientific publications, reporting both experimental and simulation results, trying to explain the anomalies observed in capillary imbibition, especially those at initial times, but none of them have satisfactorily explained the cause of these behaviors.[161,280] Two important examples of those anomalies are the slower than expected initial filling rate and the role of inertia in the momentum balance. The field of dynamics of filling has gathered momentum partly because, if the first question to be asked is how well a liquid will wet a solid[195,205,216], the second is usually how fast can it be made to fill the capillary, because this is frequently a limiting factor in nanodevice design.[5,180] The classical Washburn's force balance equation[319] to explain the capillary filling predicts infinite velocity at the pore entrance, while, Bosanquet[35] and Skezely's equation[286] predict a universal constant velocity and zero velocity respectively. But, none of these velocities have been observed neither experimentally nor through rigourous simulations.[11,161,279,288] Many authors argue that the dynamic behavior of capillary fillings is the cause of these anomalies. Moreover, the role of dynamic contact angle during capillary imbibition has been put forward in recent studies.[32,202] However, there still lacks a detailed study of the effect of initial filling conditions and the effect of dynamic contact angle of the liquid meniscus during the early stage of liquid uptake in nanocapillary imbibition. Hence, in the first part of this study we focus on describing the capillary filling process in its earliest time stage[35,223,245] and during the subsequent transition towards a fully developed flow regime.[168,202,319] Based on atomistic descriptions derived from molecular dynamic simulations, we propose a modified form of Bosanquet's equation of capillary intake that adequately describes the initial stage of liquid uptake of water in hydrophilic nanochannels. Fabrication of nanofluidic devices not only need a good understanding of fluid dynamics at nanoscale but also new methods to control the flow within them. Not much advance has been made in nanocapillary flow control, though some attempts have been devoted to study the particular aspects of these phenomena.[213,281] It has been well established that an external static electric field affects the wetting of solids due to change in the contact angle.[270,271,341] It has also been suggested that external electric fields not only modify the contact angle[86,100,325] of water but also modify hydrogen-bond orientation at nanoscale,[86,270] thus altering its viscosity.[217,352] As nanocapillary imbibition is dependent on contact angle, viscosity and the surface tension of the liquid in equilibrium with its vapor, it can deduced that nanocapillary imbibition is affected by the application of an external electric field. Hence, a detailed study of the effect of an external electric field in the nanocapillary imbibition is of great interest to explore the possible far field control of this phenomena in nanodevices. Moreover, a comprehensive understanding of capillary imbibition in nanochannels under the effect of electric fields could provide predictive tools to design functional nanosensors and nanopore-based devices. In the present study, we analyze the effect of an externally applied electric field on capillary flow of water in hydrophilic silica nanochannels. Our results indicate that the ordering of water molecules induced by the external electric field modifies the solid-liquid interfacial friction which combined with a substantial increase in bulk viscosity dominate the capillary force balance during water imbibition.

With the progress in bottom-up and top-down fabrication technology and the development of molecular self-assembly techniques, applications of nanoscale transport in laboratory and industrial applications have been increasing rapidly. One of the most important applications of nanoscale transport is nanoscale liquid pumping.[102] Water form the solute carrier in several devices in the areas of electronics and fabrication technologies.[1,251] These fluidic devices that carry electrolyte solutions have reduced the effective sizes of the circuits which has allowed the further miniaturization the present day lab-on-a-chip and plant-on-a-chip applications, with the potential to ensure the global needs of low-cost healthcare facilities.[2,76,118,169]

Having pointed out that the transport carriers in nanofluidic devices are in general electrolyte solutions, it is important to study the effect of the concentration and type of ions in flows under nanoconfinement. The presence of net surface charge on the walls of nanoconfined geometries, that develops naturally and depends upon the pH, type and concentration of ions, may supress the contribution of type of ions and their concentration during nanoflow processes due to the change in interfacial properties of wall-fluid interface. Hence, the absence of net charge on wall surface makes it easier to elucidate the effect of hydration effects, type and concentration of salts, which, in other case, might get screened. Therefore, in this thesis we study the capillary filling of electrolyte solutions at the point of zero charge.

Taking into account all the challenges discussed above, this study is based on the following hypotheses:

1.2 Hypotheses

- The lower than expected velocity during the capillary filling of nanochannels can be explained through modification of Bosanquet's force balance equation.
- The hydration related to the presence of ions in water may affect the filling kinetics in hydrophilic nanochannels.
- An external electric field reorients the water molecules and affect the dynamic properties of water which in turn affects the filling kinetics of water in hydrophilic nanochannels.

1.3 Objectives

1.3.1 General Objective

The main aim of this thesis is to study the effect of nanoconfinment on capillary imbibition of water solutions inside hydrophilic slit silica nanochannels.

1.3.2 Specific Objectives

- Identify and explain the factors that induce lower than the predicted filling rate during nanocapillary imbibition in amorphous silica nanochannels.
- Elucidate the effect of an external electric field during the nanocapillary imbibition of water in amorphous silica nanochannels.
- Illustrate the effect of the presence of electrolyte in the bulk properties of water and their effect in the nanocapillary imbibition in hydrophilic silica slit channels.

Chapter 2

Fundamental Theory and Literature Survey

2.1 Basic Principles

2.1.1 Surface tension and Young's condition

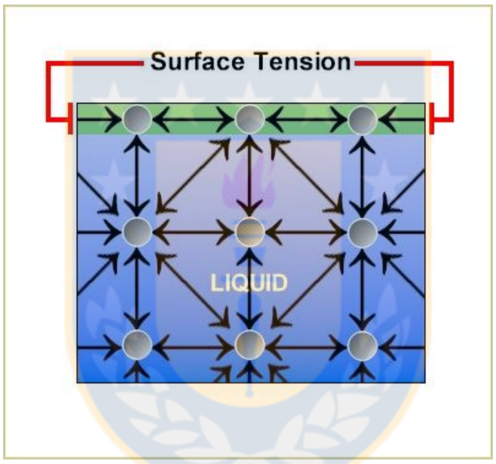

FIGURE 2.1: Mechanical definition of surface tension. Source: Own elaboration.

The force responsible for the capillarity is the result of non-symmetric action of molecular forces.[146] Let's imagine a liquid/gas system (cf. figure 2.1), a molecule in the liquid bulk benefits from interactions with all its neighbors and finds itself in a "happy state" and it contains a certain amount of cohesive energy, let's call it U, and wanders around. By contrast, one on the interface loses half of its cohesive interaction and thus, this extra energy accumulates on the surface which is proportional to the area of the exposed surface. This makes the surface of a liquid membrane with "high potential energy". Naturally, this system tends to reduce its surface energy and thus its surface area, for better stability, as objects do not remain in positions of high potential energy unless the force by the virtue of which they possess that energy is balanced by some other equal and opposite force.[71] It should be noted that when this minimum area is reached, the molecules on the surface are still attracted inwards and possess potential energy with respect to those in the interior. Hence, the excess potential energy per unit area of the exposed surface can be defined as surface tension (γ_{lv}). The S.I. unit of surface tension is Nm^{-1}. Surface tension can also be defined as the mechanical work parallel to the liquid-vapor interface required to increase the unit surface area of liquid.

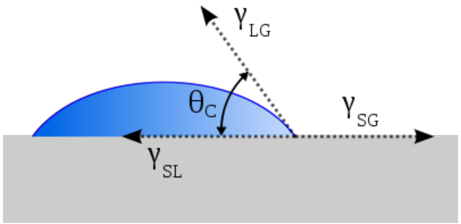

FIGURE 2.2: Formation of equilibrium contact angle on a solid surface. Source: Own elaboration.

This surface tension experienced by the liquid at the interface is the cause of cohesion among the molecules of a liquid and adsorption or adhesion between molecules of that liquid at any bounding solid surface. If we consider a point where three phases meet, ideally, solid (s), liquid (l) and vapor (v) (cf. figure 2.2) the liquid makes a certain angle (θ_{YL}) at equilibrium with the solid and vapor which is given by the famous Young-Laplace (YL) relation:

$$\gamma_{lv} \cos \theta_{YL} = \gamma_{ls} - \gamma_{vs} \tag{2.1}$$

where $\gamma_{\alpha\beta}$ is the surface tension of the interface between the two indicated phases: α and β. The liquid is considered to wet the solid if the angle predicted by equation 2.1 is less than 90° and the liquid coats the surface. On the other hand, if the θ_{YL} is greater than 90°, the liquid does not wet the surface and tends to form a sphere. However, the YL equation is applicable only on ideal surfaces and does not apply directly to many physical situations as most real solid surfaces are rough and heterogenous due to different causes including chemistry and crystal defects, among others.[214] This heterogenity is known to be responsible for the so called phenomenon of contact angle hysteresis, which is defined as the difference in the advancing and receeding angles for a contact line moving in opposite direction with the same velocity on a surface.[231] It is also worth noting that the interfacial tensions mentioned in equation 2.1 are evaluated far from the contact line.[322]

2.1.2 Capillary pressure

To explain the concept of capillary pressure, let's suppose a drop of liquid expanding under the influence of a pressure difference (ΔP) and radius of curvatures R_I and R_{II} respectively, as shown in figure 2.3. We can neglect the effect of gravity if we consider micro/nano droplets. Assuming $dxdy = 0$, the change in surface area of the drop as shown in figure 2.3 can be calculated to be:

$$\Delta A = ydx + xdy \tag{2.2}$$

The work required to change the surface area shall be:

$$dW = \gamma_{lv} \cdot \Delta A \tag{2.3}$$

From the figure 2.3, it can be deduced that:

$$\frac{dx}{x} = \frac{dz}{R_I} \tag{2.4}$$

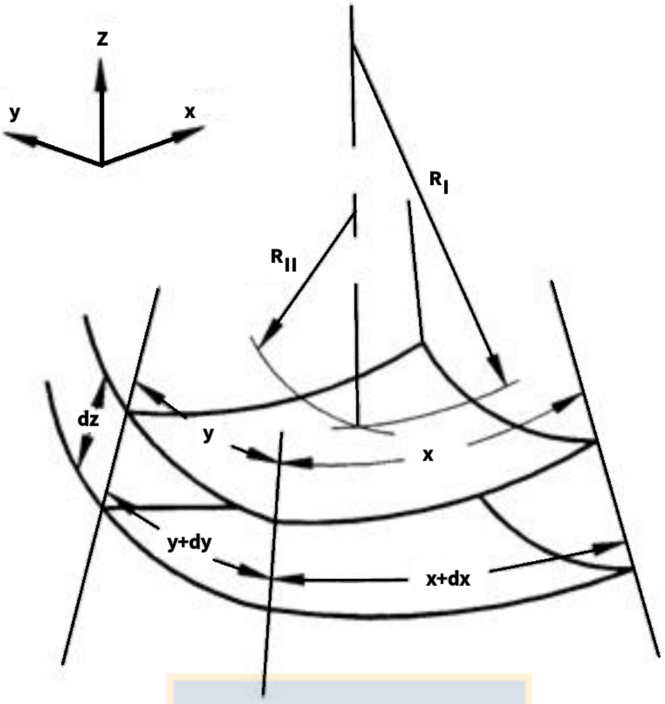

FIGURE 2.3: A schematic diagram showing a differential increase in drop size due to pressure difference. Source: Own elaboration.

$$\frac{dy}{y} = \frac{dz}{R_{II}} \tag{2.5}$$

The work done due to displacement on the area xy over the distance dz by the pressure difference ΔP (capillary pressure) across the surface is given by:

$$\delta W = \Delta P xydz \tag{2.6}$$

For the surface to be in equilibrium across this differential change, the equations 2.3 and 2.6 must be equal which leads to the following equation:

$$\Delta P = \gamma_{lv}\left(\frac{1}{R_I} + \frac{1}{R_{II}}\right) \tag{2.7}$$

It is important to note the sign convention in equation 2.7. The direction of the force is opposite to the normal surface vector due to which for concave surface the radius is taken to be negative and for convex surface, it is taken to be positive. It is due to the same reason that in a vertical concave meniscus, the force is directed upward which produces the capillary rise.

2.1.3 Capillarity

Capillarity or capillary imbibition is the tendency of liquids to flow into narrow confinements under the action of surface forces. This phenomenon is of great practical use as it is used in many industrial and day to day applications. If a tube of radius R is kept in contact with a reservoir of liquid, the invasion of liquid inside the tube occurs if the surface energy of the wall decreases as the liquid comes in contact with the solid surface ($\gamma_{sl}<\gamma_{sv}$).

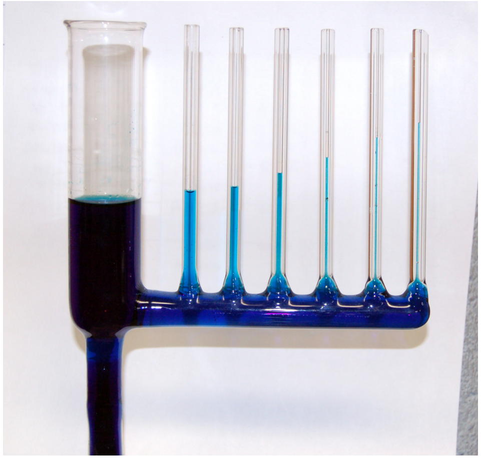

FIGURE 2.4: Capillary rise in cylindrical tubes of varying radius.
Source: Own elaboration.

2.1.4 Capillary imbibition in parallel plate

Let's consider capillary filling of two parallel plates of width ω and separated by distance H.

If we analyze the system macroscopically, we find some forces opposing the motion of the liquid inside the channel. They are: i) inertia of the liquid itself ($F_{inertia}$) ii) Force due to viscosity ($F_{viscous}$) and iii) In case the channel is vertical, the force due to gravity ($F_{gravity}$). If the liquid in the tube moves with an average velocity v, then the equation of motion can be written as:

$$F_{inertia} + F_{viscous} + F_{gravity} = F_{capillary} \tag{2.8}$$

where, $F_{capillary}$ is the capillary force due to the pressure difference across the imbibing liquid meniscus. For the systems smaller than the capillary length scale (κ), as in the case of microscale or nanoscale liquid imbibitions, gravitational force can be neglected and hence, the capillary force is balanced by the inertia and the viscous force. Hence, equation 2.8 for infinite parallel plate separated by height H becomes:

$$F_{inertia} + F_{viscous} = F_{capillary} \tag{2.9}$$

$$\frac{d(Mv)}{dt} + 12\frac{\mu\omega}{H}l\frac{dl}{dt} = 2\omega\gamma cos\theta_e \tag{2.10}$$

In the above equation, $M = \rho H\omega l$ refers to the mass of water imbibing inside the channel, and θ_e is the equilibrium contact angle made by the liquid in contact with the solid surface and l is the filling length of the liquid inside the parallel plate.

2.1.5 Different regimes of capillary filling

Inertial regime

During the early times of capillary imbibition, it has been demonstrated that the viscous force can be neglected,[159,223,244] and therefore, equation 2.10 takes the following form:

$$F_{inertia} = F_{capillary} \tag{2.11}$$

$$\frac{d(Mv)}{dt} = 2\omega\gamma cos\theta_e \tag{2.12}$$

which leads to

$$\frac{dl}{dt} = v = \sqrt{\left(\frac{2\gamma_{lv}cos\theta_e}{\rho H}\right)} \tag{2.13}$$

The driving force and the velocity during this regime remain constant[159] but the mass is time dependent, which makes this equation non-linear. The mass of the liquid in the capillary tube is related to time as $dM/dt = \rho\omega H dl/dt$. However, the weight of the liquid and the viscous friction can be neglected in this regime and we can interpret that the surface energy is converted into kinetic energy in this regime at the entrance of the capillary tube.[107,244] Having said so and assuming a constant velocity during this regime, the problem can be analysed from conservation of energy standpoint. If we consider dl to be the differential length covered by the liquid at initial time dt and dM, the mass of the liquid entered into the capillary system at time dt, then, according to the law of conservation of energy:

$$F_{capillary} * dl = \frac{1}{2}dmv^2 \tag{2.14}$$

which leads to :

$$v = \sqrt{\left(\frac{4\gamma_{lv}cos\theta_e}{\rho H}\right)} \tag{2.15}$$

Equations 2.13 and 2.15 are dimensionally similar except for the numerical coefficient. This decrepency suggests that some of the energy is lost by the liquid at the channel entrance.[72]

It is worth noting that a constant velocity (zero acceleration) has been observed experimentally[245] and have been implicitly assumed to derive equations 2.13 and 2.15. However, an unbalanced capillary force during inertial regime due to the absence of viscous force implies a finite acceleration acting on the imbibing liquid. Nevertheless, factors like interfacial contact line friction[11] and the increasing mass of the imbibing liquid[35,168,244] with time may be responsible for counteracting the unbalanced capillary force which inturn gives rise to a constant velocity during this regime.

Viscous or Washburn's regime

The viscous forces start to balance the capillary force after the inertial regime. If the amount of liquid imbibed during the early times of filling is quite small to be taken into account, equation 2.10 becomes:

$$F_{viscous} = F_{capillary} \tag{2.16}$$

$$\frac{12\mu\omega}{H} l \frac{dl}{dt} = 2\omega H \gamma cos\theta_e \tag{2.17}$$

which ultimately leads to the well known Washburn's law for capillary rise,

$$l(t) = \sqrt{\left(\frac{\gamma_{lv} H cos\theta_e}{3\mu}\right)}\sqrt{t} \tag{2.18}$$

which leads to the following expression of velocity v during the capillary imbibition,

$$\frac{dl}{dt} = v = \sqrt{\left(\frac{\gamma_{lv} H cos\theta_e}{12\mu}\right)}\frac{1}{\sqrt{t}} \tag{2.19}$$

For sufficiently long channels, this equation satisfactorily describes the experimental findings[95,228] of the liquid intake in a microcapillary tube which starts fast and subsequently slows down, $l(t)\alpha\sqrt{t}$. This behavior was also observed earlier in experiments by Bell and Cameron.[22] It seems ironical to discuss inertial regime, as mentioned by many of the investigators of capillarity to be an important drawback of Washburn's law, as Washburn in his seminal paper[319] clearly states that the law is held for the systems where the inertial regime is not important or in other words the law holds only in the region where - in his words "Liquid's velocity, which was initially very high owing to the small resistance encountered, will have dropped to such a value that the conditions of flow postulated in Poiseuille's law will have been established and these conditions will thereafter persist". In his pivotal paper, Washburn also states that the region not described by the law "perhaps disclose the two regions of turbulent flow and the slip flow" and "which are separated from each other and from the Poiseullie's region by rather pronounced breaks". It is therefore important to note that initial time, $t = 0$, for Washburn's law is not literally the value of time when the liquid enters the capillary tube, but when the liquid enters in the region described by Poiseuille's law. This situation has been addressed by Zhmund,[349] as "unfortunate" as "the underlying assumptions this equation rests on are not always kept in mind during its application". He states that the Washburn's law is not applicable to all the situations and its application depends on the physics of the system under consideration. As one studies the capillarity phenomenon in micro or nano-scale, many assumptions and modifications have to be made in Washburn's law as many physical phenomena like dynamic contact angles, slip length, precursor films and disjoining pressure irrelevant at macroscopic scale may become important at micro and nanoscales.[304] However, many researchers have successfully applied Washburn's equation to their experimental[288] and simulation results.[279] It can be considered ironical from theoretical point of view, as, i) Washburn's law is based on the viscous dissipation and does not account for loss in acceleration due to inertial force, which can be seen in capillaries with larger diameters.[223] ii) It is assumed that the equilibrium contact angle is established instantaneously which is far from being true. iii) Even if one assumes the above two points to be true, the velocity diverges at pore entrance, as it tends to infinity as time t →0 (ca. equation 2.19).

Viscoinertial regime

In the above sections, we have discussed two important regimes during the capillary imbibition: i) Inertial regime: where the inertial effects of the imbibing fluid is dominant and ii) The viscous regime: where the filling kinetics is determined by the viscous loss in the channel. However, in between these two regimes, there exists a region where the inertial and viscous forces compete with each other to balance the capillary force and can be denominated as visco-inertial regime. In this case, equation 2.10, takes the following solution:

$$l(t)^2 = \frac{2A^2}{B}\left(t - \frac{1}{B}(1 - \exp\left(-Bt\right)\right) \tag{2.20}$$

where,

$$A = \sqrt{\frac{2\gamma_{lv} cos\theta_e}{\rho H}} \qquad \text{and} \qquad B = \frac{12\mu}{\rho H^2} \tag{2.21}$$

This equation is also called "Bosanquet's equation" after the author who first introduced the effect of inertial and viscous forces in capillary filling of fluid in cylindrical pores.[35] Equation 2.9 reduces to equation 2.13 at very short times and equation 2.20 at longer times. This equation takes into account the effects of both, inertia and viscosity, due to which it best represents the transition zone between the perfectly inertial and perfectly viscous regime. The term "A" defined in Bosanquet's equation is a constant velocity term, hence this equation predicts a constant velocity during the inertial period of the liquid intake. However, it has been observed the constant velocity attained by the fluid after the nucleation is far less than the velocity predicted by Bosanquet as shown elsewhere.[11,223] This discrepancy might be due to the lack of consideration of the relation between the initial Bosanquet velocity and the momentum associated with the liquid moving towards the capillary cone.[168] Bosanquet's equation solves the velocity divergence in Washburn's solution at the pore entrance, but as already mentioned, the initial velocity predicted by this equation is much higher than the those observed experimentally. We consider that the early effect like the formation of a premeniscus at the pore entrance might be responsible for the reduced Bosanquet velocity. However, the effect of contact line friction[11,44,120,293] and dynamic contact angle[36,194,202] cannot be neglected and have to be taken into account.

Szekely's energy balance equation

Szekely et al.[286] obtained a rigorous equation for capillary rise based on the energy balance of the system which can be stated as,

$$\frac{d(KE + PE)}{dt} = -\Delta\left(\frac{u^2}{2} + gh + \frac{P}{\rho}\right) m - W_o - E_o \tag{2.22}$$

where, KE is the Kinetic energy and PE is the Potential energy associate with the liquid. Δ is the finite differential operator, u is the fluid velocity, w is the mass flow rate i.e. (velocity density cross-sectional area), W_o is the rate of work done against the surrounding, and E_o is the rate of work done against frictional forces within the fluid.[286]

For cylindrical system with radius r_o, equation 2.22 can be written as:

$$\left(l + \frac{7}{6} r_o\right) \frac{d^2 l}{dt^2} + 1.225 \left(\frac{dl}{dt}\right)^2 + \frac{\mu}{\rho r_o^2 l} \frac{dl}{dt} = \frac{1}{\rho} \left(\frac{2\gamma_{lv} cos\theta_e}{r_o} - \rho g l\right) \tag{2.23}$$

where, l is the filling length of the liquid inside the system. Equation 2.22 has no analytical solution and hence has to be solved numerically. Szekely et al.[286] used the following boundary conditions to numerically solve the equation:

$$l(t) = 0 \qquad at \qquad t = 0 \qquad (i) \tag{2.24}$$

$$\frac{dl(t)}{dt} = 0 \qquad at \qquad t = 0 \qquad (ii) \tag{2.25}$$

Although rigorous, the second boundary condition used to solve the equation cannot be correct, as it implies the existence of a regime of pure acceleration before attaining a constant velocity or inertial regime. The regime of pure acceleration has not been observed neither experimentally[11,245] nor in simulation studies.[159,223] No further development of this equation has been found in literature. The most important contribution of this equation is the inclusion of the energy loss at pore entrance.

Time demarkation of different regimes

Many researchers have tried to split the capillary filling into different regimes[66,245] but in general, capillary filling can be subdivided into three distint zones as described above: i) purely inertial regime ii) visco-inertial regime and iii) purely viscous regime. For a cylindrical capillary, let's suppose that t_1 is the time where purely inertial regime persist, t_2: where visco-inertial regime holds and t_3 where the flow is purely dominated by viscous force (ca. figure 2.5). In figure 2.5, the dimensionless scales of done by assuming the following relations:

$$t^* = \frac{8\mu t}{\rho R^2} \tag{2.26}$$

$$h^* = \sqrt{\frac{16\mu^2 h^2}{\rho R^3 \sigma \cos\theta}} \tag{2.27}$$

where, h is the filling length during the fluid imbibition, and R is the radius of the cylindrical capillary. Similarly, t_1 and t_3 are given by the following equations:

$$t_1 = 0.0232 \frac{R^2 \rho}{\mu} \tag{2.28}$$

$$t_3 = 2.2251 \frac{R^2 \rho}{\mu} \tag{2.29}$$

Then, according to Fries and Dryier,[97] the inertial regime and the visco-inertial regime deviate from their respective behavior described at time t_1 and t_3 given by equations 2.28 and 2.29 respectively. These equations are based on different assumptions by Bosanquet,[35] Quere[244] and Washburn,[319] and yet requieres experimental or simulation validity.

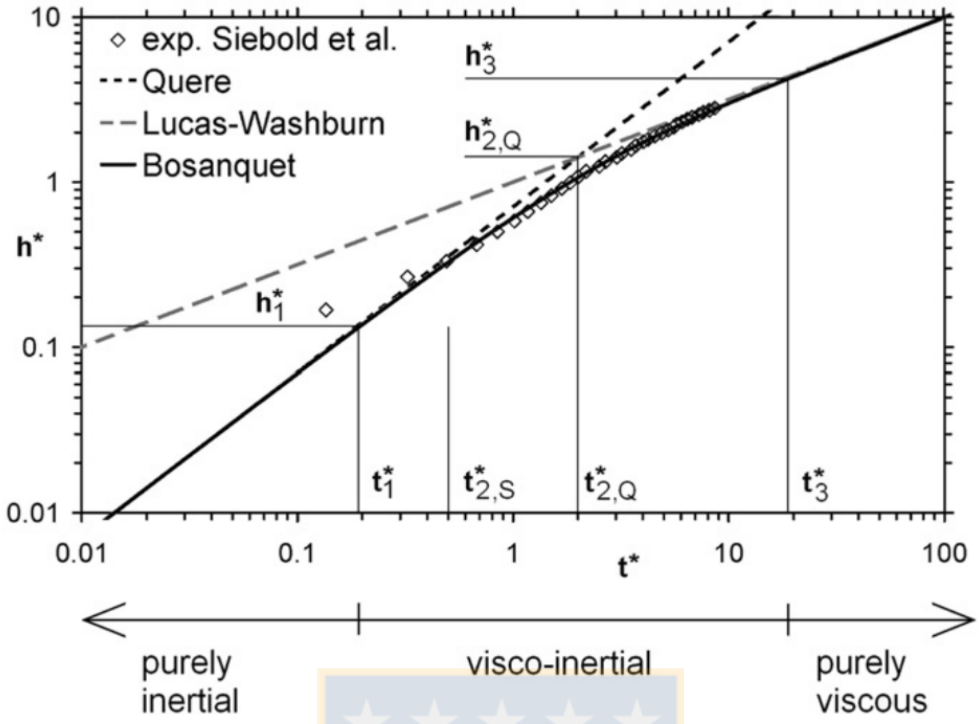

FIGURE 2.5: Dimensionless diagram showing an overview of the initial time stages of capillary rise. Source: Fries et al.[97]

Preinertial filling and energy loss at the entrance

Quere[244] argues that there should be an accelerating regime just before inertial regime as the latter takes some time to set up due to the necessity of formation of a well-defined meniscus such that the length (l) variation in this regime of pure acceleration should be proportional to t^2. Das et al.[66] argue that this regime of pure acceleration need not necessarily be proportional to t^2, as predicted by Quere but any polynomial of degree t^n would satisfactorily fulfill the requirement of velocity continuity at $t = 0$. The actual dependency of this regime of pure acceleration with time remains an open debate. Moreover, the formation of vena contracta and the form factor of the entrance[168] lead to energy loss at the pore entrance. There still lacks a detailed study of how these factors affect the capillary filling at large time. Although Szekely et al.[286] have included an energy loss term at the entrance, it has not been confirmed by other studies.

Dynamic contact angle

The determination of the contact angles is one of the most difficult nuts to crack in wetting phenomenon. In capillary fillings of nanochannels, the viscous dissipation at the contact line is large as compared to that in the bulk fluid.[202] In such cases, the classical equations of capillary rise dynamics do not accurately describe the penetration.[11] To overcome this problem, such classical equations must be modified to account for dynamic contact angle (DCA). Recent studies of capillary phenomena under nanoconfinement[101,223,279] suggest replacement of the static contact angle in the classical equations with a funtion describing instantaneous values of the dynamic contact angles to satisfactorily explain the kinetics of liquid rise. There are two main approaches for defining the dynamic contact

angle. They are i) hydrodynamic approach ii) thermodynamic approach
i) **Hydrodynamic approach**
Because of the conflict between a contact line that moves and the conventional no-slip boundary condition between a liquid and a solid, stresses are unbounded at the wetting line, and the force exerted by the liquid on the solid becomes infinite.[140] One approach to dealing with this singularity has been the truncation of the Navier-Stokes equation's solution artificially at the molecular scale where the continuum description breaks down.[312,313] Alternatively, the capillary flow equations and the boundary conditions have been modified by relaxing the no-slip condition in the vicinity of the contact line.[66,68,71,81] In this case, the force exerted on the solid is then finite, though the stresses in the liquid remain unbounded. In both cases, the capillary number is presumed to be small, so that far from the wetting line the liquid–gas interface takes its static shape. The macroscopic dynamic contact angle is then determined by extrapolating the static interface to the solid surface. The flow equations are solved using the method of matched asymptotic expansions. The main focus of the hydrodynamic approach is to relate the capillary number to the velocity of the advancing fluid. There exist many empirical and semi-empirical equations from hydrodynamic stand point to describe the wetting kinetics.[36,62,149,153] The most used hydrodynamic models are listed below:

Jiang et al.[149]

$$\tanh(4.69Ca^{0.702}) = \cos\theta_e - \frac{\cos\theta_D}{\cos\theta_e + 1} \tag{2.30}$$

Bracke et al.[36]

$$2Ca^{0.5} = \cos\theta_e - \frac{\cos\theta_D}{cos\theta_e + 1} \tag{2.31}$$

Seebergh et al.[265]

$$2.24Ca^{0.54} = \cos\theta_e - \frac{\cos\theta_D}{\cos\theta_e + 1} \tag{2.32}$$

Cox et al.[62]

$$\theta_D^3 = \theta_e^3 + 9Ln\frac{R}{l}\frac{\mu}{\gamma}\frac{dH}{dt} \tag{2.33}$$

In the above equations μ, v and γ are the liquid viscosity, capillary filling speed and surface tension of the liquid respectively. Similarly, θ_D refers to dynamic contact angle and Ca refers to capillary number and is given by:

$$Ca = \frac{\mu v}{\gamma} \tag{2.34}$$

Thermodynamic approach

Originally based on the Molecular Kinetic Theory (MKT) of wetting developed by Blake and Haynes,[31] this approach introduces a new model of frictional losses at three phase contact line, which is beyond the scope of hydrodynamics. The basic idea behind the thermodynamic approach is that contact line movement occurs from an activated rate perspective involving molecular scale jumps. The key parameters in this model are κ_0, the equilibrium frequency of the random molecular displacements occurring within the three-phase zone, and λ, the average distance of each molecular displacement. In its simplest form, the model is based on the idea that the velocity-dependence of the dynamic contact angle is due to the disturbance of adsorption-desorption equilibria and, hence, to changes in the local surface tensions as the wetting line moves across the solid surface. This approach discards dissipation due to viscous flow and focuses instead on that occurring in the immediate vicinity of the moving contact line due to the process of attachment or detachment of fluid particles (molecules) to or from the solid surface. Hence, there are just two length scales: the molecular scale, where the dissipation occurs, and the macroscopic scale where its effects are seen. The main result of this model is shown in the following equation:

$$U = 2\lambda_0 \xi exp \frac{E}{k_B T} sinh \left(\frac{\gamma \xi^2 (cos\theta_e - cos\theta_D)}{2k_B T} \right) \tag{2.35}$$

where, U is the velocity of the three phase contact line, λ_0 is the equilibrium displacement frequency, $(1 \setminus \xi^2)$ is the number of solid-liquid interaction sites per unit area, k_B is the Boltzmann's constant and T is the absolute temperature. In this relation, θ has to be interpreted as truely microscopic angle defined in molecular scale, which is fundamentally different from the macroscopic contact angle (θ_{ap}). It is important to note that λ and ξ have not been physically defined and values cannot be consistently predicted.[82] However, there have been other studies on combining the thermodynamic and the hydrodynamic approach to better define the evolution of DCA.[39]

2.1.6 Nanocapillary Imbibition

Would the laws that govern the fluid flow during capillary imbibition at macro scale behave in the same manner at nanoscale? How do variations in fluid properties due to nanoconfinement affect the imbibition process? Are there additional effects that need to be taken into account to describe capillarity at this scale? There exist many queries regarding flows at nano-confinement, as the basic understanding of flows in nanopores is still the subject of open debate and many research groups around the world are trying to unreveal the mysteries behind this.[159,223,279]
Depending upon the range of action of short and long range forces, many physical phenomena come into play, like possible changes in physical properties of the liquid, the validity of macroscopic contact angle, the presence of thin film changing the effective diameter and contact line friction among other. Moreover, diffusion of fluid molecules and viscosity are found to change significantly near the channel walls,[122,310] (several folds increase for hydrophilic channels). It modifies the interfacial dynamics of the fluid altering the boundary condition near the channel walls. Hence, stick and slip boundary conditions have been observed for hydrophilic and hydrophobic channels respectively.[28,56,150,224]
Classical force balance relations like Lucas-Washburn's (LW) and Bosanquet's equations that describe the capillary imbibition fail to explain the filling kinetics at this scale owing to the effect of nanoconfinement on fluid dynamics.[66,223,279,288] Infact, the imbibition kinetics of capillary experiments performed in nanoconduits qualitatively follows the LW model.[121,227,288,290] However, these experiments reported lower filling speed of the fluids in hydrophilic nano-conduits than those predicted

by classical LW equation. To explain this anomalous behavior of filling kinetics at nanoscale, various explainations have been put forward over the years but a general consensus on the matter has not been established yet. The slower filling rates are attributed to electroviscous effect induced by the walls on the fluid[288] and further enhanced by other effects, as pointed out in experimental study by Perssons et al.[227] In contradiction to the explanations by Tas et al.[288] and Persson et al.,[227] Mortensen and Kristensen[210] argued that the electroviscosity due to wall-effects contributes less than 1% to the apparent viscosity and suggested that electroviscosity cannot count for the observed slower than expected filling rates. In another study, Thamdrup et al.[290] attributed the slower filling rates to the formation of nanobubbles during the capillary filling. However, in contrast to the results by Thamdrup et al.,[290] Chauvet et al.[48] in their experiments with sub-100 nm channels, showed that the slower filling rates cannot be attributed to the nanobubble formation but could possibly be caused by enhanced vicosity near the solid-liquid interface due to higher ordering of water molecules. Using molecular simulations, Oyarzua et al.[223] found that the lower filling rates in hydrophilic nanochannels could not be explained even by the presence of highly pressurized gas in front of the advancing capillary meniscus. Gruener et al.[113] proposed possible negative slip length which seems to be close to the explanation provided by Haneveld et al.[121] for the observed rate of capillary filling in silica-nanochannels.

Studies in carbon nanotubes (CNTs) showed rapid rise of water[284] which indicated that the classical Washburn description no more holds good for systems with nanoconfinement as hydrophobic nanochannels can behave as frictionless pipes displaying a rapid rise in fluid column. Stukan et al.[280] included the effect of both slip and surface roughness to study capillary flows. However, their equation contained adjustable parameters which were fitted from simulation data. Despite these studies which suggest the qualitative validity of LW model, there are studies which dismiss the extrapolation of the proportionality law between meniscus height and square of time to nanometer length scales.[159,223,284]

However, other studies have tried to explain the role of line tension,[78,226] precursor films,[31,53] dynamic contact angle[82,234,279] and effect of displaced air.[48,141] Therefore, a comprehensive explanation to the deviation from the expected capillary rates observed in the filling of nanochannels compared to the LW equation predictions remains an open question.

2.1.7 Influence of electric field in nanoflows

Effect of electric field in nanosized water droplets

Interaction of a liquid droplet with an external electric field forms the basis for many microelectronic and nano-optoelectronic technologies, such as inkjet printing,[300] electrostatic painting,[17] nanoimprinting and nanomanufacturing.[171] The effect of applied electric field on the spreading of a macroscopic drop of polar liquid on a solid surface is known to be described by Young-Lippmann equation as follows:[68]

$$cos\theta = \frac{\gamma_{sg} - \gamma_{sl}}{\gamma_{lg}} - \frac{\langle \epsilon\epsilon_0 E \cdot E \rangle}{2\gamma_{lg}} \tag{2.36}$$

where, γ is the surface tension and the subscripts s, l, g refer to solid, liquid and gas respectively. Similarly, ϵ and ϵ_0 are permittivity of the medium and permittivity of the free space respectively, and E is the applied electric field. In terms of change in electrostatic energy per unit area associated with surface spreading of the liquid wetting both walls W_{el}(V), Lippmann's equation can be written as:

$$cos\theta = cos\theta_0 - \frac{W_{el}(V)}{\gamma_{lg}} \tag{2.37}$$

where, θ_0 is the contact angle in absence of external electric field. Precise form of $W_{el}(V)$ depends on the system geometry and material properties but is generally presumed to be proportional to the areal electric capacitance of the space (c) and potential drop across the space squared, $W_{el}(V) \sim cV^2/2$.[212,266] In macroscopic experiments, capillary effects due to electric field originates in a thin surface layer where the local strength of electric field is high.[146,212] On micro and nanopores on the other hand, the field extends throughout the whole aqueous slab. Not withstanding its weak ionization, pure water in a nanopore can be considered to behave as a dieletric of relative permittivity ϵ. The electric field E_0 can induce charges on the plates of a capacitor[19] or can be attributed to charges in the nearby environment. Water can enter the confinement from external field-free reservoir at ambient temperature and pressure, hence the state of confined water is fully described by specifying the values of chemical potential μ, volume $A\ w\ D$, (where Aw is the plate area and D is the interplate separation such that $A\ w \gg D^2$, temperature T, and field strength E. For a uniform field, the continuum level approximation for the difference between electrical energies of water-filled (l) and empty (e) channels treated as capacitor (c) with areal capacitance

$$c_e = \frac{\epsilon_0}{D} \qquad \text{and} \qquad c_l = \epsilon_r \epsilon_0 D \qquad \text{gives:} \tag{2.38}$$

$$W_{el} = W_l - W_e \approx \frac{D}{2}(\epsilon_r \epsilon_0 E^2 - \epsilon_0 E_0^2) \approx \frac{-\epsilon_0 D}{2} E_0^2 \tag{2.39}$$

In equation 2.39, $E_0 = V_0/D$ is the applied electric field across the slit. The above equations assume that bare surface tension $\gamma_{ab}(a, b = s(solid), l(liquid), v(vapor))$ remain unaffected by the field. While the latter is usually true for the solid-vapor term (γ_{sv}), the alignment of water molecules in response to the field can modify molecular interactions at the surface and hence further affect γ_{sl} and γ_{lv}. Favorable interaction of a polar liquid with the electric field also results in increased liquid density (ρ), which is given by:

$$dln\rho = \frac{\kappa\rho}{8\pi} \frac{\partial\epsilon}{\partial\rho} d(E^2) \tag{2.40}$$

where E is the local field and κ is isothermal compressibility. Equations 2.36 and 2.39 combined with appropiate estimate of areal capacitance of the surface, provide the basis for techniques to tune hydrophobic/hydrophilic surfaces by applying electric potential.[83,170,212,266] However, MD studies have shown that the Young-Lippmann equation generally does not hold true for spreading behavior of a nanosize droplet in an electric field.[67] This is attributed to the large surface to volume ratio in a nanosized liquid drop and to a particular orientation of hydrogen bonds near the solid-liquid-vapor triple point. For an electric field applied parallel to the solid surface, the liquid spreads to the surface asymmetrically with the leading contact angle differing from the trailing one. This is in direct contrast with equation 2.36 which suggests that the contact angle is determined solely by the magnitude of the applied electric field. Using MD simulations, Yen[341] studied the solid-liquid contact angle of a nanosized drop on a solid surface and found that the liquid-solid contact angle depends both on the polarity and field strength of the applied electric field. His results further reveals that for a perpendicular field, the contact angles first decreases and then increases as the field strength becomes higher, and also the magnitude of the change in the contact angle is different when the polarity switches for the same field strength.

Effect of electric field on flows in nanochannels

Water molecules are electrically neutral with uneven distribution of electron clouds between the hydrogen and oxygen molecules which give rise to their polar nature. In liquid state, the hydrogen atoms are constantly being exchanged between the water molecules due to protonation/deprotonation process, the rate of which depends upon the pH of water.[299] This rate of exchange of hydrogen molecules is lowest at pH 7 where the average time for the atoms to remain in a molecule is only about a millisecond. This period is found to be much longer than the timescales encountered for the formation/disruption of hydrogen bonding among the water molecules,[14,93,292] and hence, water is usually treated as a permanent structure. As water is a polar molecule, the presence of an external electric field has long been known to reorient the water molecules depending upon the polarity and strength of the applied field.[67,83,270] This reorientation of water molecules affects the ordering of molecular dipole and modifies the fluid anisotropy and biaxiality.[253] However, studies[37,155,274,352] suggest that the intramolecular structural nature and liquid phase of water under these conditions is not altered. In an interesting study of Poiseuille flow of water in carbon nanotubes, Ritos et al.[253] found that the application of an external electric field close to the entrance of a CNT membrane preorders water molecules before they enter the CNT, significantly reducing the entrance losses and consequently increasing the flow rate through the nanotube membrane for the same applied pressure difference. On the other hand, applying the same fields over the entire nanotube system increases the frictional and the exit losses, balancing the gains from reduced entrance losses and, therefore, leading to little or no increase in the flow rate. Finally, when the same fields are applied over the nanotube only, the flow rate decreases relative to the case with no electric field, and the flow rate reduction is independent of the field strength. A similar study by MacElroy et al.[198] also suggest the presence of a friction force in flow inside CNTs due to long-range electrostatic interactions.

Garate et al.[104] simulated water-self-diffusion through single-walled carbon nanotubes (CNTs) using molecular dynamics (MD) simulations in the presence of an external electric field, and found that the permeation of water into the smaller nanotubes is enhanced by electric fields due to a decrease in the fluctuations of the number of water molecules inside the nanotubes, whereas the larger extent of rotational freedom of the water molecules in the larger nanotubes allows an improved dipole alignment with the electric fields, resulting in a reduced water self-diffusion flux. Similary, it has been shown experimentally that the application of an external electric field on a fluid under nanoconfinement influences its physical properties like wettability,[67,235] adhesion and fluid-wall friction.[196] Furthermore, an study by Vaitheeswaran et al.[301] revealed a decrease in the density of the nanoconfined fluid between two hydrophobic planes in an open system in the presence of external electric field. In the same study, the authors also showed that the free energy barrier for the capillary evaporation is reduced by the application of electric field. This indicates that the application of electric field influences the key properties of the fluid which, in turn, may modify the flows through nanoconfinements.

External static electric fields have been successfully applied to influence the transport of ionic species through nanoconduits[342] and selective DNA translocation through silicon nanopores,[193] in addition to electroporation for molecular and ionic transport through lipid bilayer membranes,[269] which further demonstrates the valuable contributions that careful application of external electric and electromagnetic fields can make to nanotechnology and nanoscience.

2.1.8 Influence of ions types on flows in nanochannels

Most of the nanofabrication processes and integrated nanodevices involve ionic solutions or water containing significant amount of ionic species which forms the basis of the present day concept of lab-on-a-chip (LOC).[148,289] This concept holds the promise to insert all the functional clinical stages in a single device with very fast response and ultra portability which could revolutionize the medical and general health care practice[2,118,169] and engineering services.[109,151,246]

We have discussed the capillary flows of pure water in previous sections. The presence of ions in water under nanoconfinement adds further complications to the analysis of flows as the distribution of ions on the channel walls and the bulk may give rise to phenomena like changes in surface tension, altered viscosity by ion hydration and other associated phenomena.[154,232,242,243,291] One of the most common phenomenon that affects the flow of electrolyte solution under nanoconfinement is the formation of an electrical double layer (EDL)[137,158,326](ca. figure 2.6). The EDL model is used to describe the aqueous-electrolyte environment in the vicinity of a surface.[73,146,197,346] From the wall surface, the first layer is known as Stern layer and can be subdivided into internal and external Helmholtz planes. This layer is characterized by very high interfacial viscosity and can be interpreted as adhesion of partially hydrated and non-hydrated counterions to the surface of the wall.[197] Adjacent to the Stern layer is the diffuse layer which extends till the bulk where electroneutrality prevails. This zone is characterized by the presence of co-ions and hydrated counterions, with the concentration of counterions slightly greater to balance the residual surface charge not screened by the Stern layer. Although most of the studies report the formation of EDL near charged surfaces, recently EDL has also been reported in systems without net surface charge.[154,164] Under nanoconfinement, where the size of the EDL is comparable to the nanoscopic length scale, the high concentration of counterions near the walls highly affect the transport characteristics due to selective charge distributions. Charge distributions are the key physical descriptors of nanochannel transport as they govern axial ion transport rates, total ionic current (both advective and electromigration current), and bulk flow. In an interesting study of capillary filling of electrolyte solutions in partially and totally wetting walls, Bakli et al.[16] unveiled a remarkable finding of the amplified rate of capillary filling in a partially wettable nanochannel compared to a completely wettable one by capturing an intricate interconnection between the interfacial slip and electrostatic force, revealing the complex ion–water interactions over the nanometer scale.

The main forces that determine the dynamics of solution containing ions in nanoconfinement are the van der Waals and Coulombic forces. It has been suggested that an interplay between hydration, Coulombic and van der Waals forces in these systems are responsible for observed flow anomalies at nanoscale.[15,131,154,243] As the

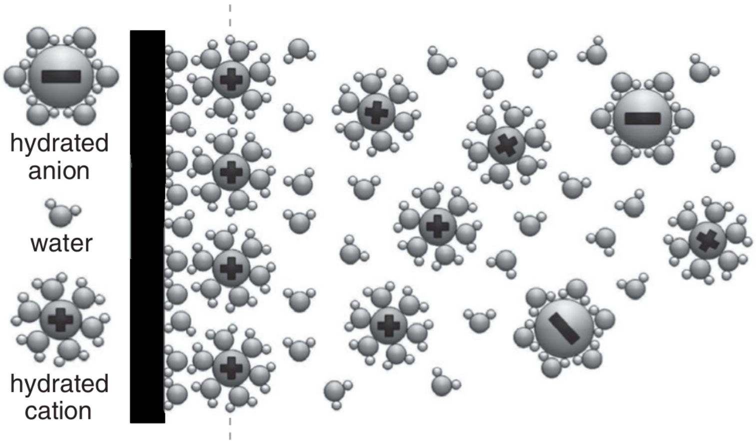

FIGURE 2.6: Skematic diagram of electrical double layer at the vicinity of a surface wall. Source: Brown et al.[40]

transport carriers in most of the nanofluidic devices, such as already mentioned LOC units, are electrolyte solutions,[99,125,186,320] it becomes important to study the influence of the type and concentration of ions in the flows under nanoconfinement.

Solid surfaces in contact with electrolyte solutions develop a net surface charge. Depending upon the type of ions and pH of the solution,[192] the effect of these surface potential may influence the distribution of dilute ionic species and their concentration at solid-liquid interface during the nanocapillary filling process.[15,154] However, study of the contribution of the hydration of ions and its effect on the nanochannel flows of electrolyte solutions becomes imperative for the adequate exploitation of the nanodevices in diverse fields of engineering and biological sciences.

Hence, in order to exclude the effects of the net surface charge on the dynamics of filling kinetics, it is important to study capillary flows at the point of zero charge (PZC) of the channel walls. At PZC, the net surface charge density of the wall becomes zero which removes the contribution of the surface potential and the excess of ions at interface in the flow under nanoconfinement. We are particulary interested in the nanocapillary flows inside hydrophilic amorphous silica nanochannels in this study, therefore, we limit this work to explore the hydration and concentration effects of mono and multielectrolyte solutions in slit nanochannels at the PZC.

Chapter 3

Molecular Simulations

3.1 Outline

Molecular simulation is a collection of (computer based) techniques for deriving, representing and manipulating the structures, reactions, behaviors and properties of molecules and their interactions. Computational methods for molecular simulations to solve real world problems have extensively been used in the recent decades[7,191,260,328,342] and have been an important tool in interpreting material behavior at molecular level.[79,327] It serves as the bridge between theory and experiments and reveals hidden details not "observed" in experiments.[7] It also helps to examine a particular theory by using a previously tested model with experimental results. Depending upon the computational capabilites, the molecular simulations can be made as exact as possible[6] to obtain the desired details of the phenomenon under study. Although the molecular modeling is easy to perform with currently available computer tools, the difficulty lies in getting the right model and proper interpretation. In general, a molecular simulation consists of a computational representation of a system wherein realistic molecular positions are used to extract structural, thermodynamic and dynamic information.[3]

The purpose of this chapter is to discuss briefly the molecular modeling technique used to study capillary imbibition under different conditions. Specifically, Molecular Dynamics (MD) simulations are performed to study the system behavior and properties in and out of equilibrium in this thesis. For detailed description of each concept, the readers are referred to classical text book on the matter.[7,23,175,259]

3.1.1 Concept of ensembles

In a molecular dynamics simulation, one often wishes to explore the macroscopic properties of a system through the molecular evolution of position and velocities, for example, to calculate changes in the binding free energy of a particular drug candidate,[80] or to examine the energetics and mechanisms of conformational change.[262] The connection between microscopic simulations and macroscopic properties is made via statistical mechanics which provides the rigorous mathematical expressions that relate macroscopic properties to the distribution and motion of the atoms and molecules of the N-body system;[174] molecular dynamics simulations provide the means to solve the equation of motion of the particles and describe the temporal evolution of a particular system. With molecular dynamics simulations,[7] one can study both thermodynamic properties and/or time dependent (kinetic) phenomenon.

The thermodynamic state of a system is usually defined by a small set of parameters, for example, the temperature T, the pressure P, and the number of particles N. Other thermodynamic properties may be derived from the equations of state or fundamental thermodynamic equations. The mechanical or microscopic state of a system is defined by the atomic positions q, and momenta p; these can also be considered as coordinates in a multidimensional space called phase space.[119] For a system of N particles, this space has 6N dimensions. A single point in phase space, describes the state of the system. An ensemble is a collection of points in phase space satisfying the conditions of a particular thermodynamic state. A molecular dynamics simulations generates a sequence of points in the phase space as a function of time; these points belong to the same ensemble, and they correspond to the different conformations of the system and their respective momenta. Several different ensembles[23,130] are described below:

Microcanonical Ensemble (NVE): The thermodynamic state characterized by a fixed number of atoms N, a fixed volume V, and a fixed energy E. This corresponds to an isolated system and in a dynamical system, the system visits all the regions of phase space with constant energy.

Canonical Ensemble (NVT): This is a collection of all systems whose thermodynamic state is characterized by a fixed number of atoms N, a fixed volume V, and a fixed temperature T. The temperature is maintained constant with an external heat bath connected to the system. This ensemble can be represented as two NVE ensembles connected to each other with heat exchange between them, assuming that the second system is much larger than the first system with $N_2 >> N_1$, $V_2 >> V_1$ and $E_2 >> E_1$.

Isobaric-Isothermal Ensemble (NPT): This ensemble is characterized by a fixed number of atoms N, a fixed pressure P, and a fixed temperature T.

Grand Canonical Ensemble(μ_c P T): The thermodynamic state for this ensemble is characterized by a fixed chemical potential μ_c, a fixed volume V, and a fixed temperature T.

In statistical mechanics, averages corresponding to experimental observables are defined in terms of ensemble averages;[298] one justification for this is that there has been good agreement with experimental results. The average values are defined as ensemble averages. An ensemble average is an average taken over a large number of replicas of the system considered simultaneously. The ensemble average is given by[23]:

$$\langle A \rangle = \int \int d\vec{p}^N d\vec{r}^N A(\vec{p}^N, \vec{r}^N) \rho(\vec{p}^N, \vec{r}^N) \tag{3.1}$$

where, $A(\vec{p}^N, \vec{r}^N)$ is the observable of interest and it is expressed as a function of the momenta $\mathbf{p}$, and the positions $\mathbf{r}$, of the system. The integration is over all possible variables of $\mathbf{r}$ and $\mathbf{p}$. The probability density ρ is given by:

$$\rho(\vec{p}^N, \vec{r}^N) = \frac{1}{Q} exp \left[\frac{-H(\vec{p}^N, \vec{r}^N)}{k_B T} \right] \tag{3.2}$$

where H is the Hamiltonian, T is the temperature, k_B is Boltzmann's constant and Q is the partition function specific to each ensemble.

One of the fundamental theorem in MD simulations is the ergodicity[55,119] which states that "Ensemble average of a thermodynamic quantity is equal to its time average" is used to predict the thermodynamic properties, the time average being given by:

$$\langle A \rangle_{time} = \lim_{\tau \to \infty} \int_{t=0}^{\tau} A(\vec{p}^N(t), \vec{r}^N(t))dt \tag{3.3}$$

The basic idea is that if one allows the system to evolve in time indefinitely, that system will eventually pass through all possible states.[247]

3.1.2 Molecular interactions

The molecular dynamics is a simulation method based on Newton's second law or the equation of motion "**F = ma**", where **F** is the force exerted on the particle, **m** is its mass and **a** is its acceleration.[7] Knowing the force on each atom, it is possible to determine the acceleration of each atom in the system.[7,247] Integration of the equations of motion then yields a trajectory that describes the instantaneous positions, velocities and accelerations of the particles.[59,257] The value of the force to compute the acceleration of a particle is derived as the negative divergence of potential.[96]

$$\vec{F} = -\Delta \cdot \Phi \tag{3.4}$$

$$\vec{F} = -\frac{\delta}{\delta \vec{r}_{ij}} \mathcal{U}(\vec{r}^N) \tag{3.5}$$

$\mathcal{U}$ for each system is defined by potential functions for the systems under study. The potential functions describe the potential energy between two interacting particles i and j separated by distance $\vec{r}_{ij}$, where, $\vec{r}_{ij} = |\vec{r}_j - \vec{r}_i|$. The total potential energy of the system is given by:

$$\mathcal{U}_{total}(\vec{r}_{ij}^N) = \mathcal{U}_{bonded}(\vec{r}_{ij}^N) + \mathcal{U}_{non-bonded}(\vec{r}_{ij}^N) \tag{3.6}$$

Bonded interactions

The $\mathcal{U}_{bonded}$ is the sum of three terms[23,96]:

$$\mathcal{U}_{bonded} = \mathcal{U}_{bond-stretch} + \mathcal{U}_{angle-bend} + \mathcal{U}_{rotation} \tag{3.7}$$

$\mathcal{U}_{bond-stretch}$ is a harmonic potential representing the interaction between atomic pairs where atoms are separated by one covalent bond, i.e., 1,2-pairs. This term is the approximation to the energy of a bond as a function of displacement from the ideal bond length b_0 . The force constant K_b, determines the strength of the bond.

$$\mathcal{U}_{bond-stretch} = \sum_{1,2-pair} K_b(b - b_0)^2 \tag{3.8}$$

In the above equation $b = |\vec{r}_1 - \vec{r}_2|$. Both ideal bond lengths b_0 and force constants K_b are specific for each pair of bound atoms, i.e. depend on chemical type of atoms constituents.

$\mathcal{U}_{angle-bend}$ is associated with alteration of bond angles θ from ideal values θ_0, which is also represented by a harmonic potential. Values of θ_0 and K_0 depend on chemical type of atoms constituting the angle.

$$\mathcal{U}_{angle-bend} = \sum_{1,2,3} K_0(\theta - \theta_0)^2 \tag{3.9}$$

where,

$$\theta = acos\left(\frac{\vec{r}_{12} \cdot \vec{r}_{23}}{r_{12}\, r_{23}}\right) \tag{3.10}$$

$\mathcal{U}_{rotation}$ represents the potential function of the torsion angle which models the presence of steric barriers between atoms separated by 3 covalent bonds (1,4 pairs) and (ϕ) is the angle between the plane vectors $1,2,3$ and $2,3,4$. This potential is assumed to be periodic and is often expressed as a cosine function.

$$\mathcal{U}_{rotation} = \sum_{1,4-pairs} K_\phi(1 - cosn\phi) \tag{3.11}$$

Non-bonded interactions

The energy term representing the contribution of non-bonded interactions potential function has two components, the van der Waals interaction energy and the electrostatic interaction energy.[7,119,247]

$$\mathcal{U}_{non-bonded} = \mathcal{U}_{vander-waals} + \mathcal{U}_{electrostatic} \tag{3.12}$$

$\mathcal{U}_{vander-waals}$: The van der Waals interaction between two atoms arises from the temporal fluctuation of electronic charge inducing transient dipoles of variable strengths.[8,129] The repulsive force arises at short distances where the electron-electron interaction is strong. The attractive force, also referred to as the dispersion force, arises from the fluctuations in the charge distribution in the electron clouds. The fluctuation in the electron distribution on one atom or molecules gives rise to an instantaneous dipole which, in turn, induces a dipole in a second atom or molecule giving rise to an attractive interaction.[8] Each of these two effects is equal to zero at infinite atomic separation **r** and become significant as the distance decreases. The attractive interaction is longer range than the repulsion but as the distance become short, the repulsive interaction becomes dominant. This gives rise to a minimum in the energy. Positioning of the atoms at the optimal distances stabilizes the system at equilibrium. Both, the value of energy at the minimum $\mathbf{E}^*$ and the optimal separation of atoms $\mathbf{r}^*$ (which is roughly equal to the sum of van der Waals radii of the atoms) depend on type of atoms.[160]

$$\mathcal{U}(r_{ij}) = 4\epsilon\left[\left(\frac{\sigma}{r_{ij}}\right)^{12} - \left(\frac{\sigma}{r_{ij}}\right)^{6}\right] \tag{3.13}$$

$$A = 4\epsilon\sigma^{12} \qquad C = 4\epsilon\sigma^{6} \tag{3.14}$$

In molecular simulations, the van der Waals interaction is most often modelled using the Lennard-Jones 6-12 potential which expresses the interaction energy using the atom-type dependent constants **A** and **C**. Values of **A** and **C** may be determined by a variety of methods, like non-bonding distances in crystals and gas-phase scattering measurements.[233] The Lennard-Jones 6-12 potential is expressed

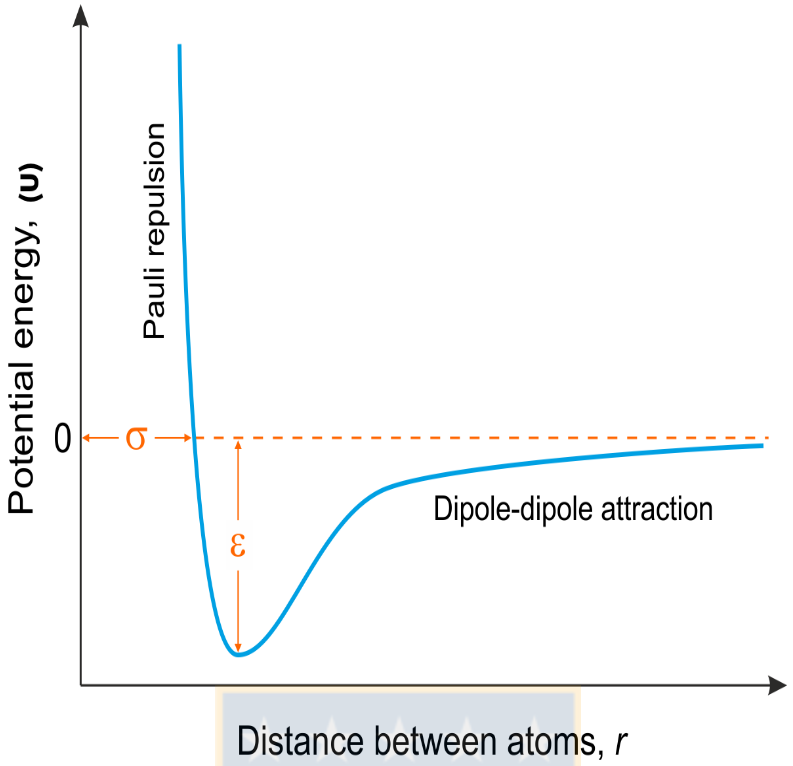

FIGURE 3.1: Lennard Jones potential and its components. Source: Own elaboration.

as equation 3.13, where ϵ is the depth of the potential well, σ is the finite distance at which the inter-particle potential is zero and r_{ij} is the distance between the particles.

$U_{electrostatic}$: All charged particles in a molecular system interact through a Coulomb potential ($\mathcal{U}_c$) given by:

$$U_c(r_{ij}) = \frac{q_a q_b}{4\pi\epsilon r_{ij}} \tag{3.15}$$

where, q_a and q_b represent the partial charges in atoms of type a and b respectively, ϵ is the permittivity of the medium, and r_{ij} the interatomic distance. Since Coulomb interactions decay slowly in comparacion to van der Waals interactions, Coulomb force computation is the most time consuming part of the force calculation process in molecular dynamics.[259] Many methods have been implemented to handle this problem, the most common of which is implementation of a cut-off distance which means that the force is computed until a fixed distance after which it is neglected. The truncation methods are very popular in MD simulations however, they are not suitable in many systems and phenomena where long intermolecular interactions are important such as ionic liquids, electroosmotic flow and electrophoresis.[7,9]

3.1.3 Neighbor list and Cut-off radius

Scalability is an important factor for N-body MD simulations. However, the computational cost and computing time become very high if we consider all the $\frac{1}{2}N(N-1)$ possible interactions.[7] Fortunately, some interatomic forces decrease strongly with distance (van der Waals, covalent interactions etc). We can thus, limit the interactions to be considered within a certain distance, the cut-off radius (r_c). It should be noted that the simple truncation is not acceptable as it would imply a finite force for an atom pair crossing the discontinuity.[23] A simple truncation of the potential creates a new problem though; whenever a particle pair "crosses" the cut-off distance, the energy makes a little jump. A large number of these events is likely to spoil the conservation of energy in a simulation.[7,119] So the potential should be modified in such a way that the potential and force are continuous at the cut-off distance; e.g. by shifting the potential as in equation below:

$$V_{SF}(r) = U_{LJ}(r) - U(r_c) - (r - r_c)U'(r_c), \quad for \quad r < r_c \tag{3.16}$$

$$V_{SF}(r) = 0 \quad for \quad r \geq r_c \tag{3.17}$$

$$V'_{SF}(r) = 0 \quad for \quad r \geq r_c \tag{3.18}$$

$$\tag{3.19}$$

where, V_{SF} is the shifted potential.

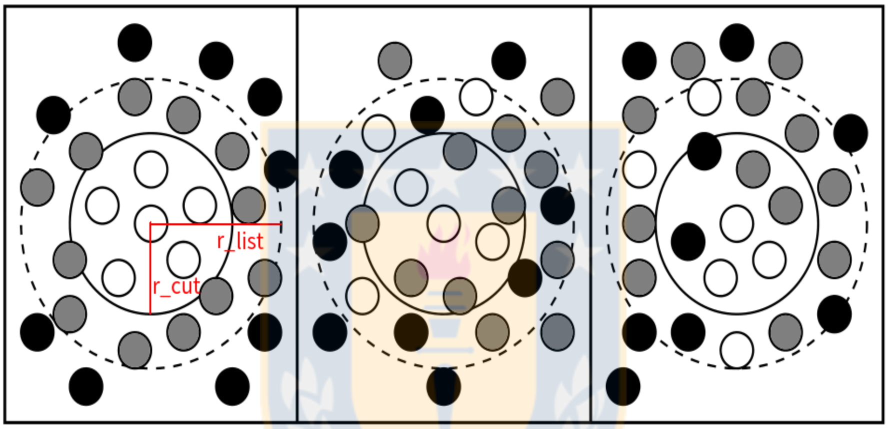

FIGURE 3.2: The Verlet list on its construction, later, and too late. The solid line represents r_{cut} and the dotted line r_{list}. The potential cut-off range (solid circle), and the list range (dashed circle), are indicated. The list must be reconstructed before particles originally outside the list range (black) have penetrated the potential cut-off sphere.
Source: Allen et al.[7]

Special care should be taken to establish the cut-off radius as for high-density NVT, the cut-off distance has insignificant influence on the radial distribution function (g(r)). However, the corresponding pressure calculated from the NVT ensemble is found to be strongly dependent on the cut-off distance used.[136] It is also to be noted that all properties of a fluid, including the radial distribution function (RDF) and thermodynamic properties, depend significantly on the attractive forces for NPT ensemble. The most common used cut-off radius in MD simulations is 2.5σ.[295] However, for large systems, this calculation still implies large calculation of forces. Hence, to reduce the number of calculation and the calculation time/cost, an additional strategy of neighbour lists can be implemented. In this approach, the cut-off sphere is surrounded by a sphere of radius r_{list} (figure 3.2).[7] In the first step of MD simulations, a neighbour list for each atom in the box is created such that the separation between the atoms is less than r_{list}.[6] It restricts the force calculation just within the neighbour list encompassed by r_{list}. The selection of this r_{list} has inherent problem that, frecuently a large number of neighbourlists need to be constructed periodically. There should be a trade-off between the computational efficiency and precision for an adequate selection of

r_{list}, as large r_{list} requieres low actualization frequency and greater precision,[54] but there is no significant saving of computation time. An alternative to overcome this issue in large systems (N > 1000) is to divide the computational box in cell lists wherein the box is divided into cells with dimensions larger than r_c and the particles are designated in the corresponding cells.[7,338] The force calculation in this case, is performed only between the particles in the same cells and the particles in the neighbouring cell list. The cell actualization is rapid and hence can be performed in each step.

Ewald Summation Method

In most of the MD simulations, calculation of the long range interactions (Coulombic interactions) are the computationally most intensive tasks during the processing.[294] In order to improve the quality and efficiency of the systems involving a N-body system with periodic boundary condition (PBC), it is important to consider methods that are computationally less expensive with better accuracy than the cut-off methods.
The total Coulombic energy of a cubic cell of size N containing N particles and their replicas in PBC is given by:[96]

$$\mathcal{U}_{electrostatic} = \frac{1}{4\pi\epsilon} \sum_{n}^{\prime} \sum_{i=1}^{N} \sum_{j=1}^{N} \frac{q_i q_j}{|r_{ij} + nL|} \tag{3.20}$$

In the above equation, r_{ij} is the distance between two particles, q_i is the charge of the particle i, and n is the cell-coordinate vector with $n = n_1 L_x + n_2 L_y + n_3 L_z$ where, $_x$, L_y and L_z are the simulation box lengths. Equation 3.20 is conditionally convergent and depends upon the order of summation.[7] The use of 3.20 in order to compute electrostatic magnitudes is know as *Direct Sum Method*. The direct sum method, although simple to implement, suffers from a major drawback: the numerical evaluation of equation 3.20 is excessively computer demanding. This problem can be "solved" by introducing Ewald sum[89] which is an alternative way to calculate these interactions.[7,23,119]
Ewald sum is a faster method to compute electrostatic quantities such as energies or forces and is based on splitting the slowly convergent equation 3.20 into two series which can be computed much faster (at level of accuracy fixed).[294] In the Ewald summation approach, the basic cell containing N/2 each of positive and negative charges in some spatial arrangement is interpreted as a single crystallographic element surrounded by an infinite number of identical copies of itself.[165]
The potential energy represented by equation 3.20 is given by two rapidly converging series plus a constant term:[96,119,175]

$$U_{Ewald} = U_r + U_m + U_o \tag{3.21}$$

The Ewald sum therefore, can be written as the sum of three parts: the direct space sum (U_r), the reciprocal or Fourier space sum (U_m), and the constant term also called self-term (U_o). The functions that best describe the real, reciprocal and the self terms are as follows:

$$U_r = \frac{1}{2} \sum_{i,j}^{N'} \sum_{n} q_i q_j \frac{erfc(\alpha r_{ij,n})}{r_{ij}, n} \tag{3.22}$$

$$U_m = \frac{1}{2\pi V} \sum_{ij}^{N} q_i q_j \sum_{m \neq 0} \frac{exp(\pi m/\alpha)^2 + 2\pi i m \cdot (r_i - r_j)}{m^2} \tag{3.23}$$

$$U_o = \frac{-\alpha}{\sqrt{\pi}} \sum_{i=1}^{N} q_i^2 \tag{3.24}$$

The self-term (U_o) is a correction term that cancels out the interaction of each of the introduced artificial counter-charges with itself. The complimentary error function decreases monotonically as x increases and is defined by :

$$erfc(x) = 1 - erf(x) = 1 - \frac{2}{\sqrt{\pi}} \int_0^x e^{-x^2} dx \tag{3.25}$$

For further details in this method, the readers are suggested to refer to the studies by Kittel[165] and Berendsen et al.[23]
The physical interpretation of decomposition of potential energy into two rapidly converging sum is shown in figure 3.3. Each point charge in the charge system is assumed to be surrounded by a Gaussian charge distribution of equal and opposite sign with charge density ρ_i such that:[240]

$$\rho_i(r) = q_i \alpha^3 exp(\alpha^2 r^2) / \sqrt{\pi^3} \tag{3.26}$$

In equation 3.26, α represents a positive parameter which determines the width of the charge distribution while, r is the position relative to the center of the distribution. Such induced Gaussian charge distribution screens the interaction between the neighboring point charges and their images in the real space converges rapidly. To compensate this induced Gaussian charge distribution, a second Gaussian charge distribution of the same sign and magnitude as the original point charge is induced and the sum is performed in reciprocal space using Fourier transforms.[119,165]

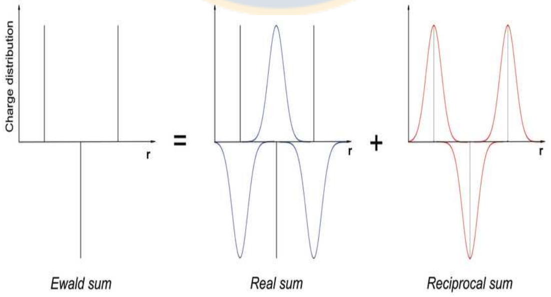

FIGURE 3.3: Treatment of electrostatic interaction using Ewald summation method. Source: Berendsen et al.[23]

By suitably adjusting α, optimal convergence of both series may be achieved which depends upon the three parameters included in Ewald's sum. Those are: n_{max}, an integer which defines the range of the real-space sum and controls its maximum number of vectors (i.e. image cells), in the similar manner m_{max}, an integer defining the summation range in the reciprocal-space and its number of vectors, and α the Ewald convergence parameter, which determines the relative rate of convergence between the real and reciprocal sums.[323] The Ewald parameters should be carefully choosen depending on several considerations and requirements of the MD simulations. Some of the important considerations to be taken into account while choosing the Ewald parameters are:[294]

- System size: Larger the system size (N), larger should be α and cut-off radius r_c. This will limit the pairwise interactions and the real space sum converges faster.
- Desired accuracy: Larger values of r_c, n_{max} and m_{max} although may yield accurate results, might lead to computational inefficiency.
- Computational time: From equation 3.22, it can be deduced that larger α leads to lesser calculations done in real space, which reduces the computational time.

Many variations of this approach like PPPM[132], PME[65], SPME[88] etc have been presented to accelerate the calculating process. The main idea behind this is splitting the slowly convergent equation into two series which can be computed much faster (at level of accuracy fixed). The trick basically consist on splitting the interaction $1/r$ as:

$$\frac{1}{r} = \frac{f(r)}{r} + \frac{1 - f(r)}{r} \tag{3.27}$$

3.1.4 Ewald methods based on Fast Fourier Transform (FFT)

The basic idea of these methods is to apply the Fast Fourier transform (FFT) to accelerate the reciprocal space part of the Ewald sum. This technique reduces the computational complexity to O(N log(N))[103], provided that the parameters are optimized. Use of FFT to accelerate the reciprocal allows for larger α, corresponding to a smaller r_c and thereby reducing the cost of real space sum calculation. All the methods based on Fast Fourier Transform are inspired by Particle-Particle-Particle Mesh Ewald (P3M)[132] developed by Hockney and Eastwood and Particle Mesh Ewald developed by Darden et al.[65] Among different methods for the 3d-periodic case are the widely used Smooth Particle Mesh Ewald[88] (SPME) method and the Spectral Ewald (SE)[188] method. The underlying principle of all the FFT-based methods are the same, wherein, irregular charges are interpolated to a uniform grid and the Poisson equation are then solved on this grid in Fourier space.

Particle-Mesh Ewald (PME)

In the Particle-Mesh Ewald (PME) method,[88] the potential energy is divided into Ewald's direct sum and reciprocal sum series and the conventional Gaussian charge distribution is used. In this method, the direct sum is calculated explicitely using cut-off while the reciprocal sum is approximated using FFT with convolutions on a grid, where charges are interpolated to the grid points. The charge interpolation function used originally in PME is Lagrange interpolation.[294] PME calculates the force analytically differentiating the energies and thus reducing memory requirements drastically. It has been argued that PME is capable of achieving higher accuracy with relatively low increase in computational cost.[294]
In this method, the Ewald parameter α is chosen large enough so as to reduce the

complexity of direct sum from $\mathcal{O}(N^2)$ to $\mathcal{O}(N)$. Similarly, the reciprocal sum is computed using 3D-FFT and is given by:

$$E_{recipro} = \frac{1}{2\pi V} \sum_{m \neq 0} \frac{exp(-\pi m/\alpha)^2}{m^2} S(m)S(-m), \tag{3.28}$$

where $S(m)$ represents the structure factor and can be approximated by:

$$S(m) = \sum_{k_1,k_2,k_3} Q(k_1,k_2,k_3) exp(2\pi i)\left(\frac{m_1k_1}{K_1} + \frac{m_2k_2}{K_2} + \frac{m_3k_3}{K_3}\right) \tag{3.29}$$

In equation 3.29, the Q matrix is a three dimensional matrix that is obtained by interpolating the point charges to a uniform grid of dimensions $K_1 \times K_2 \times K_3$ that fills the simulation cell.
However, there exists an enhanced PME method known as Smooth Particle Mesh Ewald (SPME)[88] that uses B-spline interpolation function for the charge interpolations to the grid, which is smoother and allows higher accuracy by simply increasing the order of interpolation function. The smoothness of B-spline interpolation function allows the force to be calculated smoothly by differentiating the real and reciprocal energy equations rather than using finite differentiation techniques.

3.1.5 Thermostats

At a particular point during MD simulations, the temperature of the particles is related to their kinetic energy through their momenta as follows:[23,119]

$$\sum_{i=1}^{N} \frac{|p^2|}{2m} = \frac{k_bT}{2}(3N - N_c) \tag{3.30}$$

where N_c is the number of constraints and so $3N - N_c = N_{df}$ is the total number of degrees of freedom. The average temperature (T) is identical to the macroscopic temperature. Although the standard MD simulation is performed in NVE ensemble, it is not applicable to all cases, as there are very few cases in the nature whose conditions correspond to this ensemble. Hence, most of the experiments are performed in NVT or canonical ensemble, which is performed at a constant temperature. A thermostat is required to guarantee constant temperature in MD simulations.

When a thermostat is used to control the temperature of the system, conceptually, the system (or some part of the system) is connected to a fictitious heat bath to maintain the target temperature as an time-average of instantaneous kinetic energy of the coupled degree of freedom.[142] This is achieved by altering Newton's equations of motion during the simulations so that the kinetic energy is steered toward its target. The total energy generated in a thermostatted system should follow the Boltzmann distribution for that system and generate kinetic energy consistent to Maxwell-Boltzmann distribution maintaining the erogodicity of the system.[96]
In simulations where the correct representation of transport properties are important, then the thermostat should maintain the correct kinetic energy distributions and operate in such a way that alters minimally the Newtonian dynamics.[18] Thermostats can be divided into two major groups depending upon the algorithms used to control the temperature:[69]

i) The first group consists of velocity rescaling thermostats like Berendsen[25] and Nose-Hoover.[133,218] The velocities of the particles are rescaled at regular intervals to bring the average temperature back towards the target value. This can be done by directly scaling the velocity of every particle individually, or more commonly by rescaling them together by a common factor such that the target temperature is automatically achieved.
ii) In the second group of thermostats, the velocites of the particles are randomised rather than being scaled. Typical example of this group include Anderson[9] and Langevin thermostats[282,305].

It has been suggested that the Berendsen's thermostat adequately reproduces the dynamic properties of liquid water during MD simulations as compared to other thermostats.[18] For most of the simulations in this project, Berendsen thermostat will be used, as it guarantees an efficient temperature relaxation during the equilibration of molecules.

Berendsen thermostat

In this type of thermostat,[18,25] the system is maintained at a constant temperature by coupling it to an external heat bath with a fixed temperature T_0. The velocities are scaled at each step, such that the rate of change of temperature is proportional to the difference in temperature as shown below:

$$\frac{dT}{dt} = \frac{1}{\tau}(T_0 - T(t)) \tag{3.31}$$

where τ is a coupling parameter whose value determines how tight the system is coupled to the bath. Berendsen theromostat provides an exponential decay of the temperature to the desired temperature. The temperature decay at successive step is given by:

$$\Delta T = \frac{\delta t}{\tau}(T_0 - T(t)) \tag{3.32}$$

The scaling factor for the velocity is given by:

$$\lambda^2 = 1 + \frac{\delta t}{\tau}\left[\frac{T_0}{T(t - \frac{\delta t}{2})}\right] \tag{3.33}$$

In the above equation, τ is used as an empirical parameter to adjust the strength of the coupling and special care should be taken to specify its value[211] in order to correctly predict the dynamic properties of water. In the limit $\tau \rightarrow \infty$ the Berendsen thermostat becomes inactive and the system approaches microcanonical ensemble which implies temperature fluctuations until they reach the appropriate value of a microcanonical ensemble[182]. However, they will never reach the appropriate value for a canonical ensemble. On the other hand, too small values of τ will cause unrealistically low temperature fluctuations.[142] If τ is set to be equal the timestep (δt), the Berendsen thermostat reproduces the simple velocity scaling with no temperature fluctutation and hence diverges from the reality[38]. Values of $\tau \cong 0.1ps$ are typically used in MD simulations of condensed-phase systems.

3.1.6 Periodic Boundary Condition(PBC)

The foremost item to consider during the simulation is overall shape of the system and the boundary conditions applied to it, as long range interactions highly depend on these configurations.[7,13,96] We generally tend to consider systems with size larger than we can afford to simulate with the present available computational power. The simplest and most used conditions during MD simulations are *periodic boundary conditions*, where the system is exactly replicated in three dimension, thus providing periodic lattice consisting of *unit cells*.[21] This choice of boundary conditions eliminates the surfaces and is one of the most popular choice of boundary conditions which is used to simulate a small part of a large system.[23] The basic concept of the periodic boundary conditions can be interpreted by figure 3.4. All atoms in the computational cell are replicated throughout the space to form an infinite lattice. That is, if atoms in the computational cell have positions r_i, the periodic boundary condition also produces mirror images of the atoms at positions defined as:

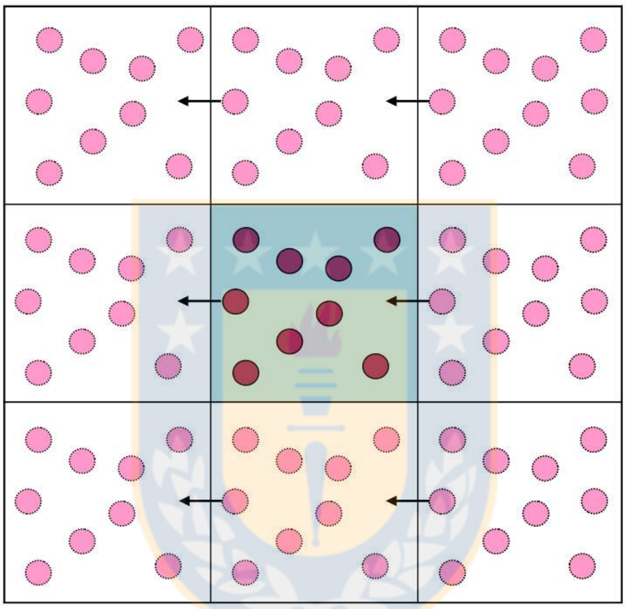

FIGURE 3.4: A conceptual representation of periodic boundary condition. Source: Berendsen et al.[23]

$$r_i^{image} = r_i + l_a + m_b + n_c \tag{3.34}$$

where, where a, b, c are vectors that correspond to the edges of the box; l, m, n are any integers from $-\infty$ to ∞. Each particle in the computational box is interacting not only with other particles in the computational box, but also with their images in the adjacent boxes and the choice of the position of the original box has no effect on forces or behavior of the system.

Although PBC eliminates the influence of artificial boundaries like vaccum space condition or reflecting walls, it adds the additional artifact of periodicity. In general, PBC has the following limitations:[23]

i) PBCs suppress all motions in neighboring unit cells that are different from the motions in the central cell.[23]

ii)The size of the computational cell should be larger than $2r_c$, where r_c is the cutoff distance of the interaction potential. In this case any atom i interacts with only

one image of any atom j. And it does not interact with its own image.
iii)The characteristic size of any structural feature in the system of interest or the characteristic length-scale of any important effect should be smaller than the size of the computational cell.

3.1.7 Initial Configuration

The integration of Newton's equation requires initial information about positions and velocities of the particles, hence they should be defined before launching a simulation at $t = 0$, and the same is called $initial\ configuration$ of the system. The best selection of the initial configuration is that of near equibrium conditions as it saves computational time.[175] A standard lattice structure is selected to represent homogenous liquids that posses large number of the identical molecules. However, in absence of experimental structure, the initial configuration is selected among the most used lattice structure like face-centered cubic (fcc), etc. It is important to determine the type of simulation to be performed and the kinds of properties to be evaluated to include the minimum number of particles and their initial positions to optimize the simulation and the results.

3.1.8 Constraint methodologies

The time step in MD simulations are chosen in such a way that no atoms moves more than a small distance Δr over which the forces on the atoms do not change significantly. It is very common in MD simulations not to represent intramolecular bonds through some bonding potential due to their high vibrational frequency of these bonds which limits the time step applied to integrate the equations of motion during the simulations. Hence, in many cases it is suitable to impose certain restrictions on the motion of particles maintaining a particular equilibrium distance between them.[7] It is generally done by imposing algebric constraints that removes the associated rapid vibrational modes, enabling the use of longer timesteps without substantially altering important physical characteristics of the motion. The most used contraints for small molecules in MD simulations are SHAKE[257], RATTLE[10] which is a velocity version of SHAKE algorithm and LINCS.[128]
SHAKE is simple and numerically stable because it resets all constraints within a prescribed tolerance. It has been shown that, when the iteration is carried to convergence, SHAKE in combination with Verlet algorithm is symplectic and time reversible.[181] In all of the simulations executed during this thesis, SHAKE algorithm shall be implemented to restrict the water structure unless specified otherwise.

Chapter 4

Effect of the meniscus contact angle during early regimes of spontaneous imbibition in nanochannels

Parts of this chapter have been published in: Effect of the meniscus contact angle during early regimes of spontaneous imbibition in nanochannels (N. K. Karna, E. Oyarzua, J. H. Walther and H. A. Zambrano, Phys. Chem. Chem. Phys., 2016, 18, 31997–32001.)

4.1 Outline

Nanoscale capillarity has been extensively investigated, nevertheless many fundamental questions remain open. In spontaneous imbibition, the classical Lucas-Washburn equation predicts a singularity as the fluid enters the channel consisting in an anomalous infinite velocity of the capillary meniscus. The Bosanquet's equation overcomes this problem by taking into account fluid inertia predicting an initial imbibition regime with constant velocity. Nevertheless, the initial constant velocity as predicted by Bosanquet's equation is much greater than those observed experimentally. In the present study, large scale atomistic simulations are conducted to investigate capillary imbibition of water in slit silica nanochannels with heights between 4 and 18 nm. We find that the meniscus contact angle remains constant during the inertial regime and its value depends upon the height of the channel. We also find that the meniscus velocity computed at the channel entrance is related to the particular value of the meniscus contact angle. Moreover, during the subsequent visco-inertial regime, as the influence of viscosity increases, the meniscus contact angle is found to be time dependent for all the channels under study. Furthermore, we propose an expression for the time evolution of the dynamic contact angle in nanochannels which, when incorporated in Bosanquet's equation, satisfactorily explains the initial capillary rise.

4.2 Introduction

Advances in micro- and nanofabrication techniques provide the ability to develop a variety of structures with well-defined features. Promissory integration of micro- and nanofluidic structures into complex nanofluidic systems such as nano-Lab On a Chip (LOC) and nanosensor devices, requires a comprehensive

understanding of the driving mechanisms for fluid transport in nanoconfinement. Due to large surface to volume ratio inherent to nanofluidics, the influence of surface effects and interfacial liquid dynamics presents fundamental challenges to the application of macroscopic theories of capillary flow in nanoconfinement. Indeed, in the topic of capillarity, the classical Lucas-Washburn (LW) equation[319], which is derived assuming a single force balance between viscous friction and capillary pressure, has proved adequate for describing the uptake of viscous fluids in relatively large capillaries and porous solid materials[168]. Nevertheless, the LW equation fails to describe the initial stage of liquid penetration[66,97,223]. The main drawback of the LW equation is the prediction of a singularity at the liquid uptake which has been attributed to not taking inertia into consideration[179,244,245,267].
Bosanquet's equation, which is equivalent to Washburn's equation for long filling times[35], describes the imbibition kinetics taking inertia effect into account therefore overcoming the singularity present in the LW equation. Recently, it has been shown that the imbibition kinetics is divided into three main flow regimes[97,223]. An initial stage, the inertial or inviscid regime, where the capillary force is balanced only by the inertial drag and characterized by a plug flow velocity profile. Thereafter, a regime, in which, the force balance has contributions from both inertia and viscous friction. Subsequently, a regime wherein viscous forces dominate the capillary force balance[97,168,223].
It is noteworthy that during the inviscid flow regime, the Bosanquet solution predicts a constant velocity[66,97,168,223] therefore, in a non-accelerating imbibing fluid the capillary force must be exactly balanced by fluid inertia. It seems contradictory to the usually assumed immediate and continuous variation of the meniscus contact angle right from the channel entrance[101,202,279] as, continuously increasing capillary force due to Laplace pressure cannot exactly balance the inertial force induced by the fluid inertia[35,66,168,223,250]. Therefore, it implies that all the other factors during the capillary imbibition kept constant, there should exist a meniscus with constant contact angle during the inertial regime. Furthermore, it has been found that the initial constant velocity is lower than that predicted by Bosanquet's equation[48,168,223,250].
In this study, we address this problem by performing large scale molecular dynamics simulations of the initial imbibition of nano-confined water into silica channels. We report the time evolution of the capillary front and meniscus contact angle during the capillary filling of nanochannels with heights ranging from 4 to 18 nm. Providing an atomistic description of the capillary filling process in its earliest time stage and during the subsequent transition towards a fully developed flow regime, our study allows a complete characterization of the kinetics of liquid imbibition in nanochannels which explains the initial meniscus formation and its relation to the constant velocity during the inertial regime.
Bosanquet's equation: Bosanquet's solution of capillary imbibition for infinite rectangular capillary, takes the form of equation (5.6)[223].

$$l(t)^2 = \frac{2A_I^2}{B}[t - \frac{1}{B}(1 - \exp(-Bt))] \tag{4.1}$$

A_I and B in the above equation are given by

$$A_I = \sqrt{\left(\frac{2\gamma\cos\theta}{\rho H}\right)} \tag{4.2}$$

$$B = \frac{12\mu}{\rho H^2} \tag{4.3}$$

where, A_I corresponds to the initial velocity just at the entrance. The equilibrium contact angle in this equation is assumed to be attained instantaneously which is contrary to more recent studies[36,63,81,82,149,265,267]. Hence, it is important to account for dynamic contact angle (DCA) in Bosanquet's equation to adequately explain the capillary rise. We propose that DCA, which can only be seen after the inertial regime, can be modeled by equation (4.4) and (4.5).

$$cos\theta_d = cos\theta_i \quad \text{for} \quad \text{t} \leq t_i \tag{4.4}$$

$$cos\theta_d = cos\theta_e \left(1 - exp\left(-\frac{t}{\tau}\right)\right) \text{for} \quad \text{t} > t_i \tag{4.5}$$

In the above equation, τ should be proportional to characteristic time for fully developed flow and is given by equation (4.6)[20], t_i refers to the time during which the inertial regime persists and θ_i is the initial contact angle made by the liquid with the nanocapillary walls.

$$\tau = K_1\left(\frac{H^2\rho}{\mu}\right) \tag{4.6}$$

We consider this correlation after the inertial regime as viscous force starts playing a significant role and inertia becomes negligible.

Inertial regime: Inertial regime refers to the "inviscid regime" and is characterized by constant velocity (U_o), where the filling is driven by a balance between the inertial force and capillary forces, which results in,

$$U_o \sim \sqrt{\left(\frac{\gamma}{\rho H}\right)} \tag{4.7}$$

Assuming $l \sim H$, during the inertial regime and taking into account $U_o = l/t_i$, we obtain,

$$t_i = K_2\sqrt{\left(\frac{H^3\rho}{\gamma}\right)} \tag{4.8}$$

where, K_2 is the proportionality constant.

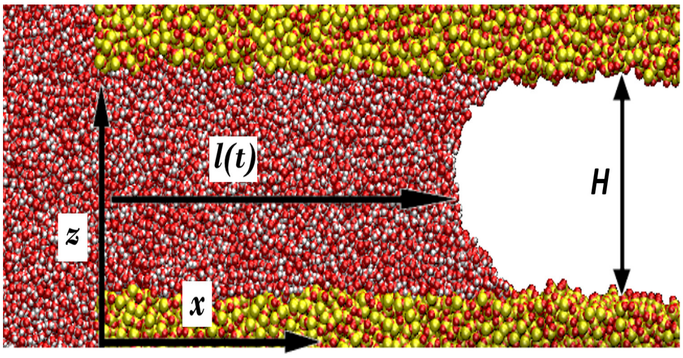

FIGURE 4.1: A snapshot of the capillary filling for a 6nm silica nanochannel. Source: Own elaboration.

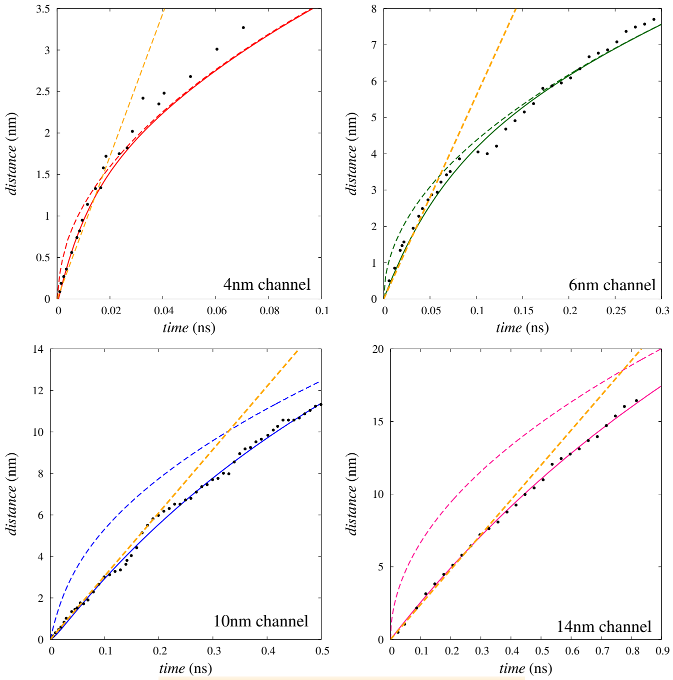

FIGURE 4.2: Nanocapillary imbibition length as a function of time for different height of capillaries.The black dots represent the imbibition length as a function of time. The straight yellow dashed lines are visual guides to indicate the $l(t) = A_I t$, which also illustrate estimated times of inertial regime. The solid lines depict the fits of modified Bosanquet's equation to the experimental data. The colored dotted lines are visual guide lines to indicate the original Bosanquet's equation. Source: Own elaboration.

4.3 Simulation details

To study the validity of these models and investigate the initial imbibition in silica nanochannels we conduct a series of MD simulations using the MD package FASTTUBE[223,316,324,343,344]. The potential parameters used in the present study have been calibrated in our previous study[343] wherein the silica-water interaction potential was calibrated using as criterion the water contact angle reported by Thamdrup et al.[290]. Water is described using a modified version[184] of the simple point charge SPC/E model[24] and silica by the TTAMm model developed by Guissani and Guillot[114]. For further details of the potentials used, we refer the reader to Zambrano et al.[343] and Oyarzua et al.[223]. The interaction potentials used for this study is tabulated in $SI.A.1$. Periodic boundary condition (PBC) has been applied to all the simulations in this study.

Rectangular nanochannels of different heights (4,6,10,14,18 nm) were built by amorphous silica slabs (Fig. 4.1). For the details of slab construction, an annealing procedure is implemented[139,343], wherein the two silica slabs are coupled to a Berendsen heat bath with a time constant of 0.1 ps. The cristobalite is heated to 3000 K keeping the temperature constant during 10 ps, and subsequently, quenching the system from 3000 K to 300 K by imposing a cooling rate of 70 K ps^{1} until the equilibrium state is reached. In the simulations, the equilibration of water is performed first in NVT ensemble at 300 K using a time step of 2 fs, coupled to a Berendsen heat bath[24] during 1 ns; then, the thermostat is disconnected and the simulations are conducted in the microcanonical ensemble (NVE) for the next 1 ns until the system is relaxed and the dynamic properties of water are attained. Subsequently, the water slab is released from the rest to move spontaneously towards the silica channels. The number of water molecules used in each simulations depends upon the height of the channel and is listed in Table 4.1. The nanocapillary imbibition simulations are performed in microcanonical ensemble to avoid the perturbations induced by the application of thermostat in the motion of liquid particles and hence, their effect in hydrodynamics.

Other properties that influence the nanocapillary imbibitions are: surface tension of the vapor-liquid interface and viscosity of the fluid. In this study, we calculate the viscosity and surface tension of water for SPC/E water molecules using Stokes-Einstein relation and stress-tensor calculation method respectively. For details of viscosity and surface tension calculations, readers are referred to $SI.A.2$. The viscosity of water at 300 K is calculated to be 72.6 mPas while the surface tension of the water-vaccum interface is calculated to 62.8 respectively. These values are inline with those determined in other studies[127,306,352].

TABLE 4.1: Configurational details of water imbibition in silica nanochannels. H is the channel height, channel length was kept constant to 31.6 nm in all the cases

Case No.	H(nm)	No of H_2O molecules
1	4	18000
2	6	22000
3	10	32000
4	14	52000
5	18	56000

Source: Own elaboration

4.4 Results and Discussions

The initial velocity and the inertial time (t_i) for each simulation were estimated from the atomic trajectories. Subsequently, the value of τ in equation 4.6 was approximated such that the dynamic contact angles predicted by equations (4.4) and (4.5) fitted those obtained from the simulation results. Then, the values of K_2, as indicated in equation (4.8) was calculated using the values of t_i estimated from the simulation results. The contact angle at time t_i was obtained as an average value of angles determined from snapshots taken each 2 ps[270] during the inertial regime from three different simulations using exactly the same protocol and parameters. The velocity at inertial regime was estimated from the slope of the filling kinetics during the inertial regime and compared with those calculated using equation (5.8) for each channel. Instantaneous position of advancing capillary front is tracked along the direction perpendicular to the flow of water to find the penetration length of water. An example of the meniscus is shown in Fig. 4.1. In Fig. 4.2, we plot the temporal evolution of the imbibition length as a function of time for all the channels under study. The time evolution of penetration lengths during early time periods, as displayed in the figures, is linear which indicates a capillary flow with constant velocity thus, confirming the existence of inertial regime as predicted by Bosanquet[35,168,223]. It can be observed that the inertial regime is more prominent in channels of greater height. Duration of inertial time (t_i) for all the cases were directly calculated from the simulation data. The slope

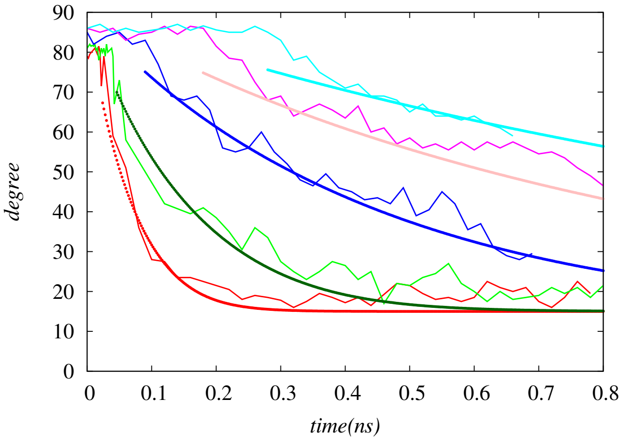

FIGURE 4.3: Measured contact angles (dotted lines) and those predicted by the model (solid lines) during the nanocapillary imbibition in silica nanochannels of different heights. The red, green,blue, pink and cyan lines represent the contact angles for 4, 6, 10, 14 and 18 nm channels respectively. Source: Own elaboration.

of the plot of inertial time against $\sqrt{H^3\rho/\gamma}$, gives an estimated value of K_1, mentioned in equation (4.8), and is approximately found to be 1 (Fig. 4.4). Hence, the inertial time is given by equation (4.9)

$$t_i = \sqrt{\left(\frac{H^3\rho}{\gamma}\right)} \tag{4.9}$$

$$Ca = \frac{\mu v}{\gamma} \tag{4.10}$$

As mentioned earlier, the velocity during the inertial regime remains constant (cf. Fig. 4.2) which implies that the dynamic contact angle observed during this regime remains constant (cf. Fig. 4.3) which is consistent with the hydrodynamic models of contact angle development[63,149,312], that relates DCA with capillary number (ca. equation 4.10),[200] and constant velocity during the inertial regime predicted by Bosanquet's equation[35]. In other words, the DCA remains constant during the inertial regime when the velocity is constant and gradually lowers with low velocity when viscous losses in the bulk become significant till it apparently attains the equilibrium value. A constant contact angle during the inertial regimes implies that this angle should be achieved right at the channel entrance when the liquid comes in contact with the upper and lower solid walls. For a channel with constant height, the imbibition velocity depends only on the contact angle made by fluid with the walls[244]. It has been shown by Oyarzua et al.[223] that the initial velocity decreases with channel height, as seen in table 4.2, the contact angle which determines the velocity during inertial regime[244], should increase with channel height. This has been confirmed in the present study and can be seen in Fig. 4.3. It leads to an interesting conclusion that the initial angle made by water at the channel entrance is different to 90° and depends on the height and material of the channel[194]. It also concludes that during inertial filling, capillary force is balanced by inertial force as predicted by Bosanquet. From the simulation data, we find that the product of cosine of the initial contact angle made by the fluid with the nanochannel walls and the height of the channel remains constant for imbibition

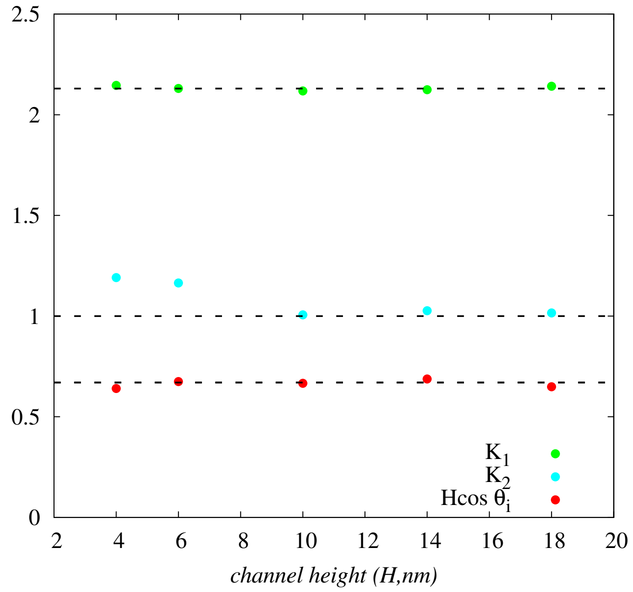

FIGURE 4.4: Calculated values of the constants as a function of channel height (H). The dotted lines represent linear fits while the coloured dots are the measured values. Source: Own elaboration.

of water in hydrophilica silica nanochannels and is given by

$$Hcos\theta_i = C \tag{4.11}$$

where, C is a constant and most probably depends upon the interaction of fluid and wall at the entrance and the pre-imbibition conditions[168,194,287]. For the silica-water system, this constant is approximately equal to 0.67 (Fig. 4.4). This also explains the low velocity observed during the capillary filling which cannot be explained by the original Bosanquet's equation. Hence, we propose that the effective Bosanquet's velocity is given by equation (4.12)

$$A = \sqrt{\left(\frac{2\gamma cos\theta_i}{\rho H}\right)} \tag{4.12}$$

where, θ_i is the initial contact angle made by liquid surface with the nanochannel walls. The above equation satisfactorily explains the observed and predicted velocity during the inertial regime as can be seen in table 4.2. The initial constant angle determined by equation (4.11) remains constant for time t_i that can be predicted by equation (4.9) after which dynamic contact angle is observed and is described by equation (5.9). The values of τ mentioned in this equation can be estimated by equation (4.13), substituting the average value of K_1 from fig (4.4).

$$\tau = 2.132\left(\frac{H^2\rho}{\mu}\right) \tag{4.13}$$

Similar results has been observed by Fries[97] for cylindrical channels when the capillary filling is determined by the balance between the viscous and capillary

TABLE 4.2: Values of parameters during initial rise. E_v is the estimated value of velocity using the modified Bosanquet's equation, similarly, C_v is the calculated velocity. t_i is the inertial time period while, τ is the adjusting parameter given by equation 4.6.

H(nm)	$E_v(nm/ns)$	$C_v(nm/ns)$	$t_i(ns)$	$\tau(ns)$
4	76	77.5	0.025	0.047
6	56	54	0.047	0.105
10	33	35	0.11	0.29
14	23	25	0.19	0.57
18	18	20	0.28	0.95

Source: Own elaboration

forces. This time (t_f) as determined by Fries[97] is given by:

$$t_f = 2.1151\left(\frac{H^2\rho}{\mu}\right) \tag{4.14}$$

The constant angle observed during the inertial regime and good approximation of initial velocity obtained from the simulations and those calculated by modified Bosanquet's equation confirm that the predominant force during the inertial regime are inertial and capillary forces and other forces are not relevant during the initial filling, contrary to the predictions made by other researchers[11,120,349]. It can be observed that Bosanquet's equation modified by including a dynamic contact angle satisfactorily describes the initial regimes of capillary imbibition (Fig. 4.2). In table 4.2, E_v refers to the estimated velocity using equation 4.12 and C_v refers to the calculated velocity from the simulation data.

4.5 Conclusions

In summary, the present study revealed that the velocity and contact angle remain constant during the initial time of nanocapillary imbibition, thus confirming the predictions by Bosanquet that the predominant forces during the inertial regime are inertial and capillary forces. We find that dynamic contact angle is observed after inertial regime when viscous dissipation becomes more prominent. The dynamic contact angle is found to be height and time dependent for the channels under study. The incorporation of the proposed time dependent relation for DCA in Bosanquet's equation successfully predicts the initial filling kinetics of silica-water system as well as the initial velocity at the entrance. Initial contact angles different from 90 ° have been observed for all the channels which establishes that, for a given system, initial contact angle depends on the height of the channel.

Chapter 5

Capillary imbibition of electrolyte solutions in hydrophilic silica nanochannels at point of zero charge

Parts of this chapter are included in the manuscript under preparation: Nabin Kumar Karna, Jens H. Walther and Harvey A Zambrano. Capillary imbibition of electrolyte solutions in hydrophilic silica nanochannels at point of zero charge.

5.1 Outline

Water is a polar fluid which responds to the strong electric field around the ions dissolved in it. This particular behavior results in modified ordering of water molecules around the ions compared to pure water. Although most of the studies involving flow of electrolyte solution at nanoscale deal with the effect of net surface charge, the understanding of the physics behind the flow requires the knowledge of hydration effects of dissolved ions, as it may significantly affect the dynamic properties of water, not only due to nanoconfinement but also due to the specific ionic species present in the solution.
The main goal of this study is to elucidate the effect of the respective hydration shell of dilute ions during nanocapillary imbibition. The presence of a net surface charge on the channel walls during the imbibition process may conceal the influence of the hydration of ions and their concentration on the hydrodynamics of the electrolyte solution. Therefore, in the present work, we study nanocapillary imbibition of dilute solutions of electrolytes in water at the point of zero charge (PZC) of the channel walls. In this work, we employ series of molecular dynamics simulations to study the imbibition of different concentrations of mono and multivalent cations in amorphous silica nanoslit channels. Our results suggest that the capillary filling of electrolyte solutions inside hydrophilic silica nanochannels is governed by an enhanced viscosity as the result of electroviscous effect that depends directly upon the type, valency and concentration of cations.

5.2 Introduction

The development of promising technologies such as nanoscale lab-on-a-chip devices[118] and nanoarrays platforms for biological analysis,[236] is directly related to recent advances and rapid sophistication of the nanofabrication techniques.[29]

Nevertheless, the success of lab-on-a-chip designs is subjected to the possibility of efficient handling of tiny amounts of aqueous-electrolyte solutions through nanoconduits[209] among other factors. A comprehensive understanding of fluid dynamics of electrolyte solutions at nanoconfinement is required to meet these demanding challenges. For instance, nanocapillarity, an essential transport mechanism in nanofluidic devices which plays a key role in a broad variety of biological[276,311] and technological processes,[105,238,308] has been a subject of extensive study for years now, however, a fundamental understanding of the physics governing early stages of liquid imbibition remains challenging.[159,244,286] In nanocapillarity, a balance between the pressure difference across the curved advancing capillary front and a drag with variable contributions from inertia and viscosity governs the filling.[35,223,279] The inertial effects becomes negligible as the filling length becomes sufficiently large.[35,223,319] Consequently, as the characteristic inviscid time is elapsed, capillary force is gradually dominated by viscous losses. Aqueous electrolyte solutions are present in many nanofluidic applications.[148,289,320] The design and characterization of silica nanochannel-based devices and sensors require understanding of silica-electolyte interfacial dynamics and the nanoconfinement effects on the transport properties of hydrated ions.[77,154,309] Furthermore, it has been found that depending on the ionic valency, the strong electric field surrounding ions dissolved in polar fluids influences the fluid viscosity and diffusion[163] by altering the structure of water molecules around the ions. As the transport carriers in most of the nanofluidic devices are electrolyte solutions,[99,125,186,320] it becomes important to study the influence of the type and the concentration of ions in the flows under nanoconfinement. Ions, in general, can be classified as kosmotrope or chaotrope, respectively, depending upon their ability to order (structure makers) or disorder (structure breakers) the water structure (hydrogen bond network) in the solution.[201] For instance, K^+ and Cl^- ions are known to disrupt the hydrogen bonding network in water, and hence are classified as chaotropes,[135] while ions like Li^+, Na^+, Mg^{2+}, Ca^{2+} and Al^{3+} are classified as kosmotropes as they are known to increase the ordering of hydrogen bridges in water.[26,201,261]

The main forces that determine the dynamics of solution containing ions in nanoconfinement are van der Waals and Coulombic forces. The behavior of Coulombic force may depend on the type of electrolyte, concentration or the pH of the solution.[15] Solid surfaces in contact with electrolyte solutions develop a net surface charge, depending upon the type of ions and pH of the solution,[192] which may conceal the hydrodynamic effects exerted by the presence of ions and their particular concentrations during capillary flow processes.[15,154] In this work, we aim to study the effect of the hydration of ions on the nanocapillary imbibition of electrolyte solutions in hydrophilic silica channels. At the point of zero charge (PZC), the net surface charge density of the wall becomes zero. Hence, in order to exclude the effects of the net surface charge on the dynamics of filling kinetics, it becomes imperative to study the capillary imbibition of electrolyte solutions at PZC of the channel walls. Moreover at PZC, the partial charges on the individual surface atoms are not screened that might reveal the long range effects of these atoms which may have significant effect on the static and dynamic properties.[154]

To this end, we perform a systematic study of the influence of cations on the capillary imbibition of dilute electrolyte solutions in silica nanochannels at the PZC using molecular dynamics simulations. In our simulations, the nanochannels consist of neutral silica walls and electrolyte solutions of mono and multivalent ions with concentrations ranging from 0-1 molar. From the MD trajectories, we extract the evolution of the advancing meniscus position in the channels for different concentrations and types of electrolyte solutions. Furthermore, we determine the wettability, viscosity and surface tension of the imbibing solutions and analyze the influence of the ionic charge density on the fluidity of water in nanocapillary imbibition.

5.3 Simulation methods

We study capillary filling of electrolyte-aqueous solutions of 7 different types of salts at 5 different concentrations in a 6 nm high amorphous silica channel. The types and concentration of the salts used in this study are listed in table 5.1.

TABLE 5.1: Salts and their concentrations used to study the nanocapillary imbibition in hydrophilic silica nanochannel.

Salts		Concentration			
LiCl	0.2	0.4	0.6	0.8	1.0
NaCl	0.2	0.4	0.6	0.8	1.0
KCl	0.2	0.4	0.6	0.8	1.0
$MgCl_2$	0.2	0.4	0.6	0.8	1.0
$CaCl_2$	0.2	0.4	0.6	0.8	1.0
$BaCl_2$	0.2	0.4	0.6	0.8	1.0
$AlCl_3$	0.2	0.4	0.6	0.8	1.0

Source: Own elaboration

To elucidate the effect of dissolved multivalent electrolytes in water on capillary imbibition in a hydrophilic silica channel, we construct an amorphous silica slit nanochannel as shown in figure 5.1. For the slab construction and amorphization protocol of silica walls, we refer the readers to our previous studies.[159,223,342,343] Water is described using the simple point charge SPC/E model[303] and silica by the TTAMm model developed by Guissani and Guillot.[114] For heteronuclear interactions without specified interaction parameters, we use Lorentz-Berthelot mixing rule (see **SI** B.3).[7,33] The individual parameters used for the interaction of ions in the system is listed in table 5.2.

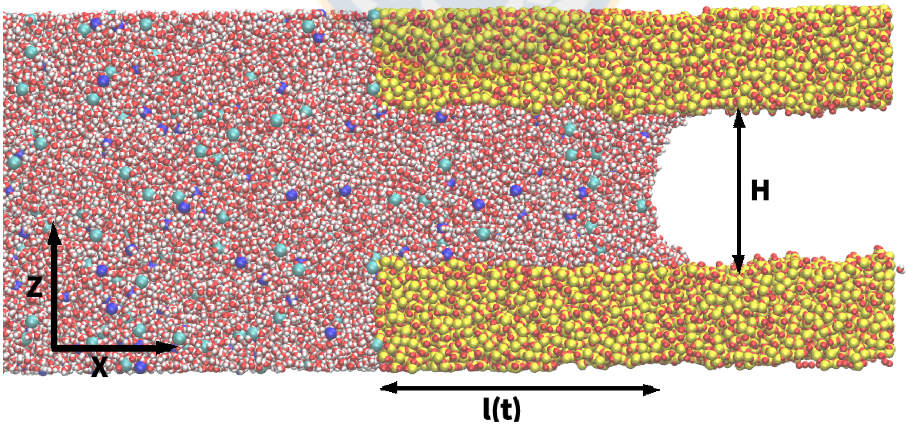

FIGURE 5.1: A snapshot of the capillary filling for 6-nm silica nanochannel. In the above figure, H refers to the height of the channel while $l(t)$ is the time dependent filling length. Source: Own elaboration.

TABLE 5.2: Interaction parameters for the electrolytes used in the study. (Si- Silicon, O - Oxygen, Li - Lithium, Na - Sodium, K - Potassium, Mg - Magnesium, Ca - Calcium, Ba - Barium, Al - Alumunium, Cl - Chloride ion)

$a-b$	σ_{ab} (nm)	ϵ_{ab}(kJ/mol)	Reference
Li-Li	0.2343	0.0249	Pethes[230]
Li-Cl	0.3097	0.2353	Pethes[230]
Li-O	0.23300	0.6694	Pethes[230]
Li-Si	0.26505	0.60710	Pethes[230]
Na-Na	0.258	0.0617	Bonthius[34]
Cl-Cl	0.4401	0.4184	Aluru et al.[154]
Cl-O	0.3785	0.5216	Aluru et al.[154]
Cl-Si	0.3895	1.0118	Aluru et al.[154]
Na-O	0.2875	0.2003	Aluru et al.[154]
Na-Si	0.38861	0.2983	Zambrano et al.[342]
K-K	0.3334	0.4184	Aluru et al.[154]
K-Cl	0.3866	0.4184	Aluru et al.[154]
K-O	0.325	0.5216	Koheshan et al.[167]
K-Si	0.3359	1.0118	Aluru et al.[154]
Mg-Mg	0.1398	3.6610	Gavryushov[106]
Mg-Cl	0.2900	1.2376	Prakash et al.[239]
Mg-O	0.2282	1.5428	Prakash et al.[239]
Ca-Ca	0.2361	1.8810	Gavryushov[106]
Ca-Cl	0.3381	0.8871	Prakash et al.[239]
Ca-O	0.2764	1.1059	Prakash et al.[239]
Ba-Ba	0.3790	0.1970	Zhu et al.[351]
Ba-Cl	0.4096	0.2871	Zhu et al.[351]
Al-Al	0.14472	0.9054	Faro et al.[92]
Cl_{Li}-Cl_{Li}	0.3852	2.2240	Pethes[230]

Source: Own elaboration

For further details of the potentials used for amorphization of silica slabs and equilibration of water, we refer the readers to table **SI** B.2.[223,343] The slab of water with electrolytes of interest at particular concentration is equilibrated at NVT ensemble using a Berendsen thermostat[25] for 2 ns at 300 K, after which the system is allowed to relax in NVE ensemble for the next 2 ns. Subsequently, the density and the potential energy of the electrolyte solutions are measured to verify that the system has attained equilibrium.

5.3.1 Water contact angle measurement

Imbibition rate of water into nanochannels is very sensible to the equilibrium contact angles made by water droplets with the silica walls as the latter determine wetting of the capillary walls and hence, the capillary force responsible for driving the process. To study the effect of ion-type and ionic concentration on the water contact angle (WCA) of electrolyte solutions on hydrophilic amorphous silica slab at PZC, we perform MD simulations of a cylindrical water drop consisting of 3000 water molecules and ions according to the required concentration, on a silica slab of size 37.92 nm x 2.584 nm x 3.5 nm in vacuum. We adopt the same methodology as described in the previous section for the amorphization of the silica slab and equilibrium of water molecules.

After equilibration of water molecules, the drop is placed at a distance of 0.5 nm to the silica-wall and allowed to spread spontaneously on the silica slab with zero net charge, under NVE ensemble for 2 ns. Posterior to this, WCA is measured as the average values of snapshots taken every 50 time steps during the last 0.5 ns.[270] A snapshot of contact angle measurement is shown in figure 5.2.

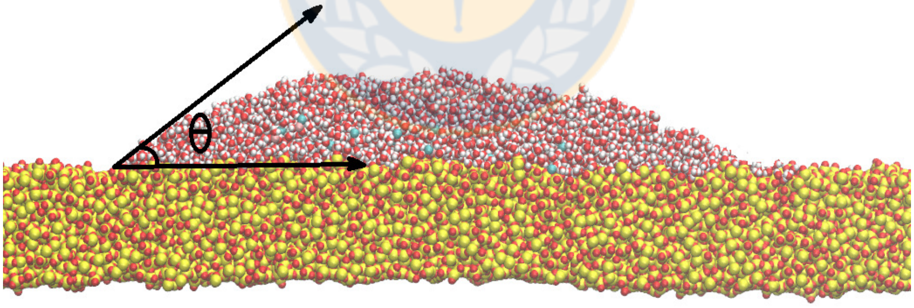

FIGURE 5.2: A snapshot of the contact angle measurement on a hydrophilic silica slab. Source: Own elaboration.

5.3.2 Imbibition of electrolyte solutions in capillary channel

To study the capillary imbibition of electrolyte solutions in silica nanochannels, water slabs with particular concentration of ions are equilibrated at 5 nm from the silica nanochannels at NVT ensemble for 2 ns with a Berendsen thermostat[25] connected to the system. Subsequently, the water slabs are relaxed for 2 ns in NVE ensemble which, not only establishes the equilibrium properties of water with ions, but also guarantees a homogenous dispersion of ions in water. After equilibration, the positions of water and ion molecules are shifted and the water slab with ions is placed at 0.5 nm from the hydrophilic silica nanochannels. The slab with electrolytes is then released for the imbibition process to take place in the NVE ensemble. In an attempt to extract the behavior of fluid containing dissolved electrolytes, we simulate a system whose walls do not chemically interact with the fluid or the ions present in it, and hence are electrically neutral. For details of wall-ion interactions, the readers are referred to **SI** B.2. We keep the silica walls frozen during the simulations of water equilibration and imbibition of water into the channel. The temporal evolution of the position of water meniscus inside the silica nanochannel during the imbibition is tracked. The initial velocity (ν_0) and the duration of inertial time (t_i) for each simulation during nanocapillary imbibition are estimated from the atomic trajectories.

5.3.3 Surface tension measurement

One of the most important properties of a fluid and the cause of capillary force that drives the fluid into the capillary channels[150,173,190,304] is interfacial free energy which can be translated into surface tension.[116,145,248] Hence, it becomes important to study the effect of electrolyte solutions on surface tension of water to predict its role in nanocapillary imbibition of these solutions. Surface tension of pure water has been studied in previous studies and various authors have sucessfully predicted values of the surface tension for different models of water molecules.[4,7,203,306] In this study, we calculate the surface tension of aqueous electrolyte solutions using pressure tensor method. For details into surface tension measurement we refer the readers to **SI** A.2.

5.3.4 Viscosity measurement

Viscosity is one of the key kinetic properties of fluids and computationally, one of the most difficult properties to estimate. There have been many efforts of estimation of viscosities of water and other fluids through molecular dynamic simulations and other computational techniques.[12,115,122,131,162,272,347,352] Although there have been extensive experimental studies on the effect of ionic concentration on the viscosity of electrolyte solution, atomistic simulations studies to delve into the molecular details of the effect of ions on the viscosity of electrolyte solutions remain scarce. We calculate the viscosity of all the solutions using the periodic perturbation method, a non-equilibrium molecular dynamics technique proposed by Gosling et al.[110] and developed by Hess.[127] As in our simulation of wetting and nanocapillary filling, water molecules are described using the SPC/E water molecule model, we use the same for our viscosity calculations. For further details into the periodic perturbation method, readers are referred to the study by Hess[127] and Sunda et al.[283]

In this study involving viscosity measurement, all simulations were carried out in a cubic simulation box with a side of 5 nm. Adequate numbers of ions and water molecules were inserted in the box to get the desired concentration and density of the electrolyte solutions. Temperatures of all the systems were controlled by a Berendsen thermostat[25] during equilibrium stages and then a Nose-Hoover thermostat[133,218] were used for the production simulations. The pressure during the equilibrium stages of electrolyte solution were controlled using a Berendsen barostat.[25] Periodic boundary conditions (PBCs) were applied in all the three directions of the simulation boxes.

The systems were equilibrated for 5 ns at NVT and the outputs were then subjected to NVE ensemble at 300 K to relax for 1 ns. We monitor the potential energy and density during all the simulations to verify that the equilibrium is attained. In order to calculate the viscosity of water, we run NEMD simulations for 10 ns. The first 5 ns were dropped from the analysis and the viscosity was analysed over the next 5 to 10 ns.

5.4 Results and Discussion

5.4.1 Nanocapillary imbibition of the electrolyte solutions

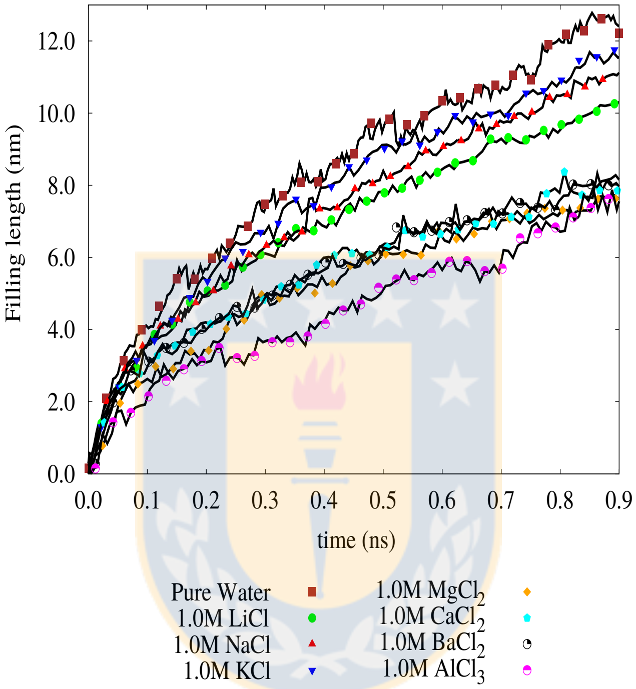

FIGURE 5.3: Capillary filling of 1.0 molar electrolyte solutions in a 6nm wide hydrophilic silica channel. Source: Own elaboration.

We constructed a 6 nm wide silica nanochannel and performed imbibition studies of various electrolyte solutions at five different concentrations (see table **SI** B.1). The electrolyte solutions we use in our studies are relatively dilute, which guarantees Newtonian behavior during the filling process. In figure 5.3, we plot the temporal evolution of meniscus of 1 molar solutions of all the electrolytes under study. We observe that the initial velocities of the ionic solutions at the channel entrance during the early stages of filling where fluid inertia is dominant over the viscous forces (inertial regime) is approximately constant for a specific electrolyte solution and is independent of the electrolyte concentration, however, it differs among the species of ions within the range of concentrations under study. We also observe that the filling rate of solutions containing structure breaker[201] cation *viz.* K^+ is higher in all the cases, as expected. For very dilute solutions, we observe that the filling rate is concentration independent, however, at higher concentrations, the filling kinetics seems to be divided depending upon the type of cations (see figures **SI** B.2 and B.4). For a specific ionic species, the filling rate during the viscous regime, where the viscous force is dominant and determines the filling kinetics, seems to be concentration dependent. However, the initial filling

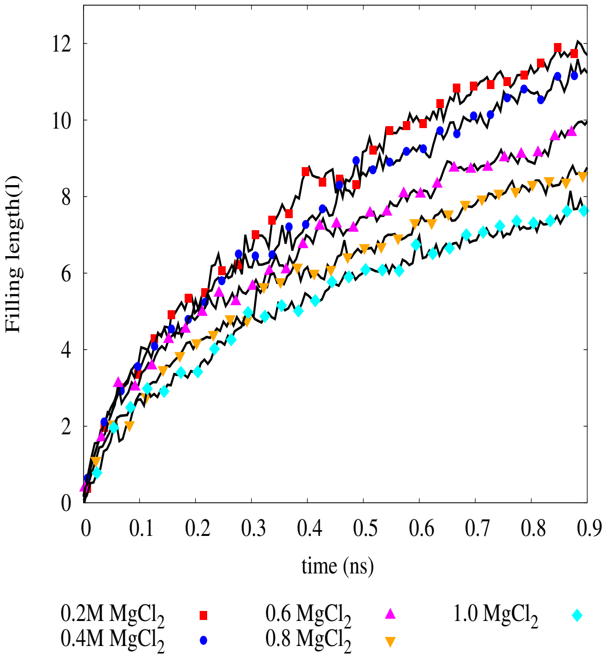

FIGURE 5.4: Capillary filling of different concentrations of $MgCl_2$ in a 6nm wide hydrophilic silica channel. Source: Own elaboration.

rates even for the different concentrations of the same cation remain appoximately constant (see figures **SI** B.5,B.6,B.7,B.8).

In nanochannels with net charge on the walls, the filling kinetics is determined by the complex interactions of charged walls with the ionic solutions and the decrease in filling rate can be attributed to the interplay of electrical and hydrodynamic forces over interfacial scales.[16] However, the slowing down of filling kinetics in absence of net surface charge seems interesting and merits further investigations.

To investigate further into the apparent cause of the slower filling rate with increasing concentration of the electrolytes en the aqueous solutions, we compute additional properties that influence the filling kinetics at nanoscale, *viz*. surface tension, viscosity and equilibrium Young's WCA .

Radial Distribution Function

Radial distribution function (RDF) is used to study the structure of liquids and distribution of solvent molecules around a solute molecule. We calculate the radial distribution functions of the ions used in this study, plots of which are shown in figures 5.5-5.8. To calculate the RDF of the ions used in this study, we equilibrated an anion-cation pair in a cubic slab of water containing 4000 molecules of water in NVT ensemble at 300 K for 10 ns. Subsequently, the slab containing particular pair of anion-cation pair was subjected to equilibrium in NVE ensemble for next 15 ns after which, the production simulations to calculate the RDF were conducted in NVE ensemble for 2 ns.

The comparison of characteristic values of the peaks and positions of all the ions at 300 K to the values reported in the literature and experimental works are tabulated in table 5.3. We observe that the height of the peak along the groups of

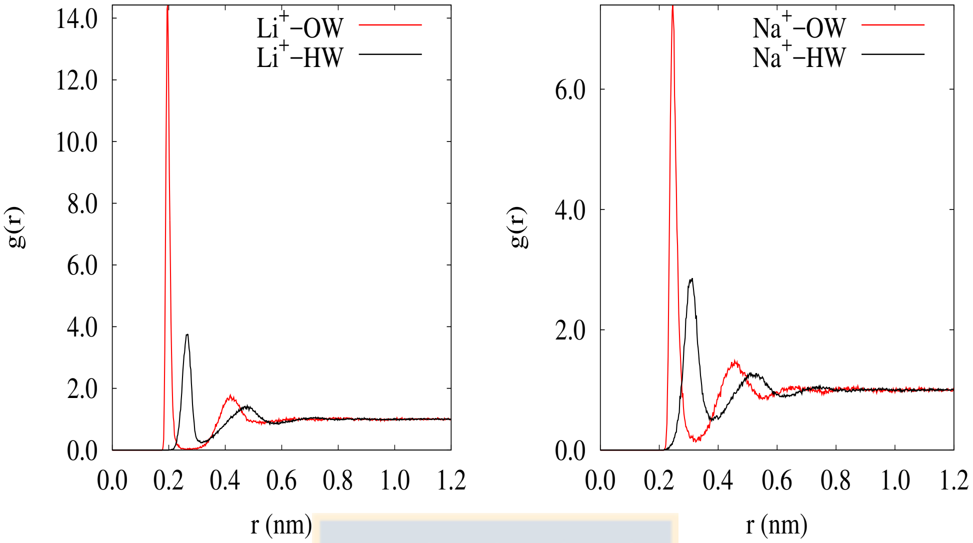

FIGURE 5.5: Radial distribution functions of Li^+-OW (left) and Na^+-OW (right). Source: Own elaboration.

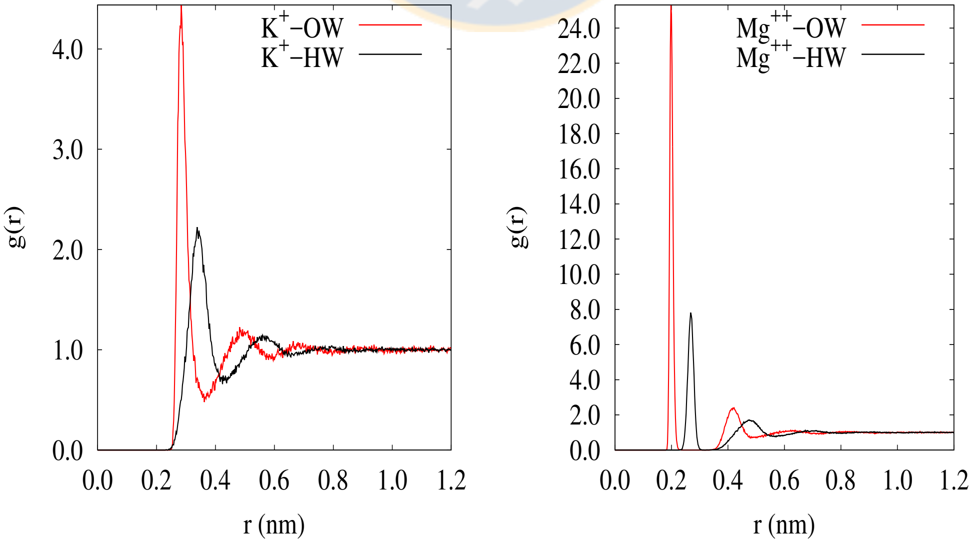

FIGURE 5.6: Radial distribution functions of K^+-OW (left) and Mg^{2+}-OW (right). Source: Own elaboration.

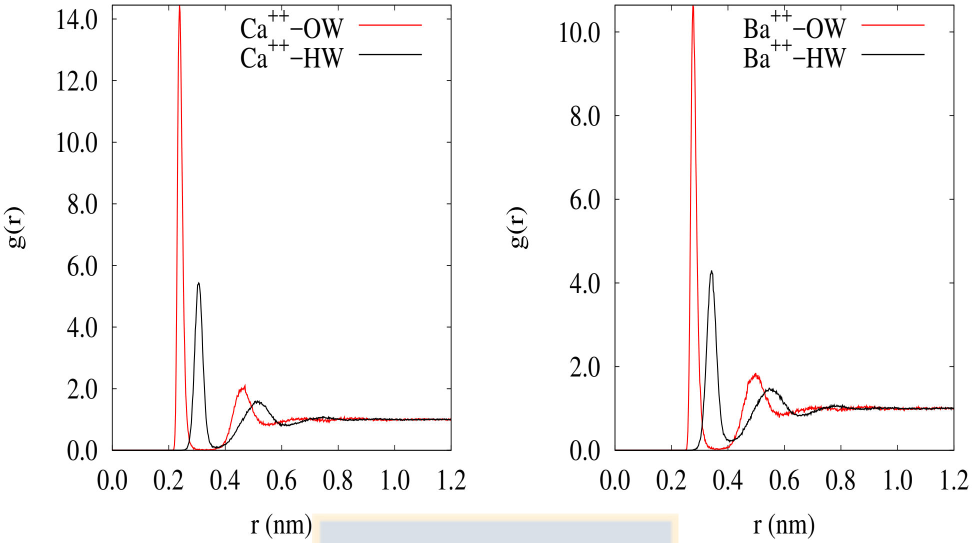

FIGURE 5.7: Radial distribution functions of Ca^{2+}-OW (left) and Ba^{2+}-OW (right). Source: Own elaboration.

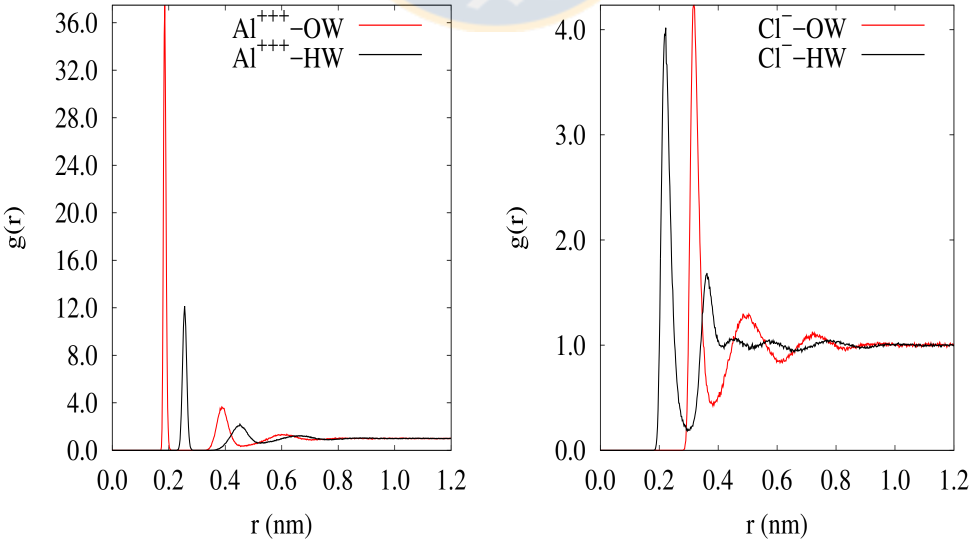

FIGURE 5.8: Radial distribution functions of Al^{3+}-OW (left) and Cl^{-}-OW (right). Source: Own elaboration.

periodic table decreases which indicates that the hydration effects are more pronounced in the ions with higher charge density among the same group.[144,167] For cations, the position of the peaks of RDFs of ions with respect to oxygen ($g(r)_{OW}$) is nearer than those compared to hydrogen ($g(r)_{HW}$) that suggests the presence of oxygen atoms nearer to the cations and hydrogen away from them and is a strong indication of hydration effect for positively charged ions.

TABLE 5.3: Comparison of characteristic peak values and positions of the ions in water at 300 K.

		$g_{OW}(rmax)$	r_{max}(nm)	$g_{OW}(rmin)$	r_{min}(nm)	N_c
Li^+	MD (present work)	14.4	0.196	0.0	0.26	4.32
	MD[178]	9.56	0.22	0.03	0.31	6.00
	MD[350]	13.76	0.197	0.00	0.256	4.40
	Experimental[201]	-	0.194	-		4.10
Na^+	MD (present work)	7.39	0.245	0.14	0.32	5.33
	MD[178]	7.00	0.245	0.22	0.350	6.60
	MD[350]	8.11	0.237	0.08	0.306	5.20
	Experimental[201]	-	0.234	-	-	5.30
K^+	MD (present work)	4.43	0.2827	0.50	0.36	6.42
	MD[178]	5.64	0.270	0.35	0.365	8.00
	MD[350]	4.02	0.286	0.45	0.369	6.10
	Experimental[201]	-	0.265	-	-	6.00
Mg^+	MD (present work)	25.32	0.2	0.0	0.3	6.03
	MD[219]	17.2	0.22	0.0	0.31	6.2
	MD[42]	0.4	0.21	-	-	6.0
	Experimental[201]	-	0.209	-	-	6.0
Ca^+	MD (present work)	14.43	0.24	0.0	0.3	7.47
	MD[143]	-	0.25	-	-	7.6
	MD[74]	-	0.237	-	-	7.1
	Experimental[201]	-	0.240	-	-	7.0
Ba^+	MD (present work)	10.62	0.28	0.0	0.35	8.3
	MD[275]	-	0.28	-	-	8.3
	Experimental[201]	-	0.281	-	-	8.1
Al^+	MD (present work)	37.14	0.19	0.0	0.2	5.88
	MD[207]	40.99	0.18	0.0	0.20	6.0
	Experimental[201]	-	0.191	-	-	6.0
Cl^-	MD (present work)	4.23	0.32	0.43	0.38	6.81
	MD[350]	3.96	0.33	0.55	0.375	6.40
	MD[117]	3.9	0.3275	-	-	8.4
	Experimental[201]	-	0.316	-	-	7.0

Source: Own elaboration

The simulation results of RDFs presented in this study agree well with the experimental results and other simulation studies.[85,147,201,204,345] Small differences in the peak position is be due to the difference in potential models used in this and other studies.[57,117,207,219,275]

Coordination number is another characteristic variable to represent the structure of liquids. It is defined as

$$N_c = 4\pi\rho_g \int_0^{r'} g(r) r^2 dr \tag{5.1}$$

TABLE 5.4: Total interaction energy (kJ/mol) between ion- water pair in the first solvation shell at 300 K.

Li^+	Na^+	K^+	Mg^{++}	Ca^{++}	Ba^{++}	Al^{+++}	Cl^-
274.8	167.933	110.88	519.23	327.885	214.25	849.62	298.31

Source: Own elaboration

where, N_c is the coordination number, ρ_g the number density, $g(r)$ the radius distribution function, r is the interparticle distance and r' is the distance to the first minimum. The results presented in table 5.3 suggest that the coordination number increases with the ionic size and decreases with ionic charge density. For the ions of the same group in the periodic table, we observe that coordination number increases with ionic radius since more water enters the first coordination shell.

The angular distribution function (PDF) of the water molecules in the first shell of all the ions included in the present study is shown in 5.10. For cations used in this work, the orientation of water molecules around the aluminium ion is strongest whereas the weakest orientation occurs around potassium ion. The values of cosine of the orientation angle present a maximum at 1, which indicates the water molecules approaching the cation with the oxygen atom towards the ion.

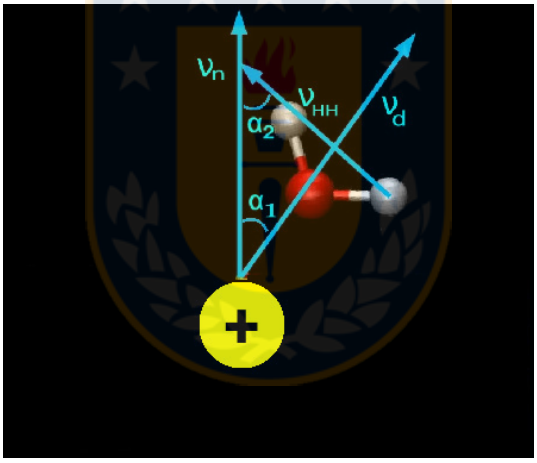

FIGURE 5.9: The angles considered to determine the orientation of the water molecules around specific ions. Source: Own elaboration.

We also calculate the average interaction energy of the ion-water pair per mole (cf. figure 5.11).

The higher ion-water interaction energy indicates higher stability of the solvation shells and hence the reduced movement of water molecules around the ions (see table 5.4). The interaction of the solvation shell with the bulk water determines the dynamic properties of the solution. This interaction may be determined by the water dipole orientation around the ions and the average distance (d) between the hydrogen atoms of the first shell and the adjacent oxygen atoms of the bulk (see table 5.5). We observe that d is smallest for Al^{3+} ion which suggests that viscosity and surface tension of solutions containing AlCl_3 to be the highest among those studied in this work.

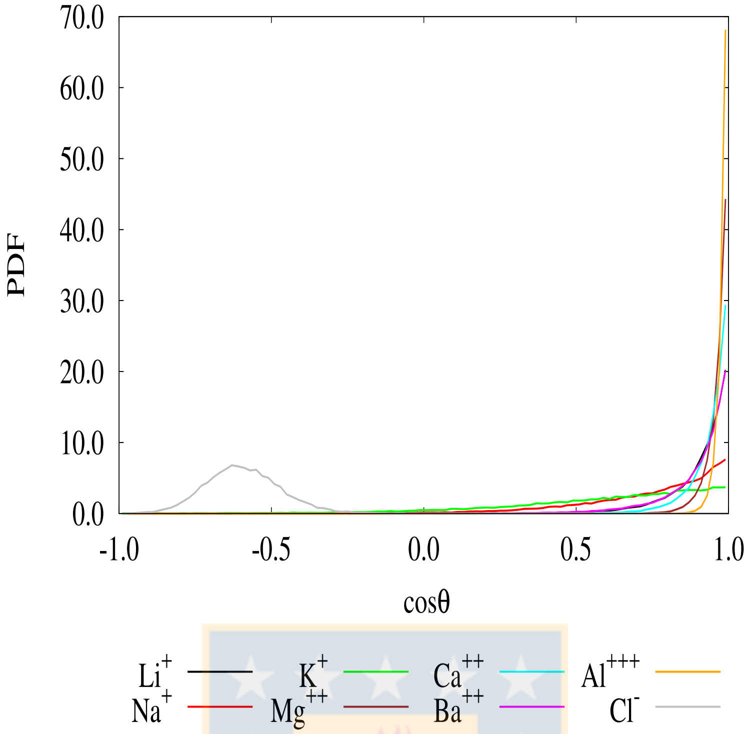

FIGURE 5.10: Normalized angular distribution function of water dipoles around the ions used in this study. Source: Own elaboration.

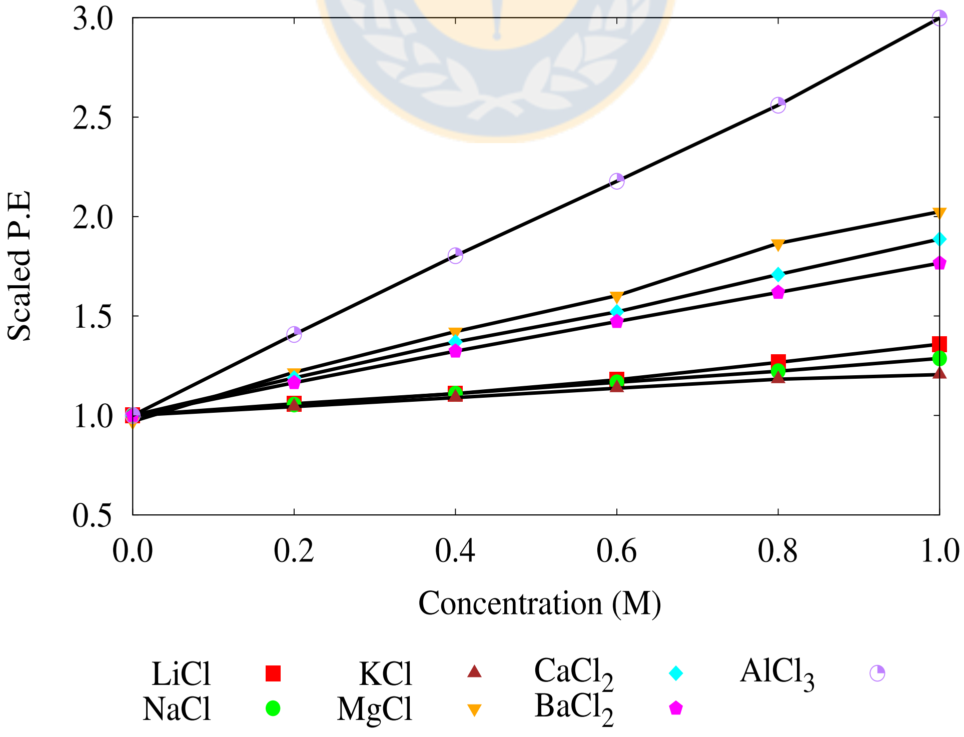

FIGURE 5.11: Potential energy between ion-water for different concentrations for the electrolyte solutions under study. Source: Own elaboration.

TABLE 5.5: Distance (nm) between the hydrogen atoms of the first shell and the adjacent oxygen molecules in the bulk at 300 K.

Li^+	Na^+	K^+	Mg^{++}	Ca^{++}	Ba^{++}	Al^{+++}
0.152	0.146	0.144	0.147	0.1666	0.1525	0.131

Source: Own elaboration

5.4.2 Effects of ions on viscosity of electrolyte solution

The effect of ions on the electrolyte solution can be qualitatively predicted using Hofmeister series and the concepts like kosmotropes (structure making ions) and chaotropes (structure-breaking ions).[201,334] The viscosity is determined mainly by two types of quantities:[135] the increase or decrease in ordering of water molecules due to added electrolyte, and entropies of ion solvation. The viscosity (μ) of an aqueous electrolyte solution typically has the following dependence on ion concentration (c):[152]

$$\frac{\mu}{\mu_0} = 1 + Ac^{1/2} + Bc.. \tag{5.2}$$

where μ_0 is the viscosity of pure water at the same temperature. A is a constant independent of c; its corresponding term can be explained by Debye−Huckel theory.[138,208] The constant B, the Jones−Dole coefficient[152] is the quantity that defines the degree of water structuring around the ions. B is positive for kosmotropic ions and negative for chaotropic ions.

It has been proposed that dynamic properties like viscosity can be understood in terms of activation energy required to strip a water away from the first solvation shell of an ion compared to that of another water molecule and is well described by:[134]

$$\Delta E_i = E_i - E_0 \tag{5.3}$$

where, E_0 is the energy required to separate two water molecules in the bulk and E_i is the energy required to pull a water molecule from the first shell in an ion coordination shell. A water molecule "binds" to a small ion more tightly than it binds to a neighboring water molecule, resulting in a positive activation energy. The effects of ions on water could be explained by a competition between ion-water interactions that are dominated by charge density effects, and water-water interactions, which are dominated by hydrogen bonding.[60] In this part of the study, we focus on the effect of ion types on the viscosity of the electrolyte solutions at different concentration levels. The viscosity of an aqueous solution of a structure-making ion, such as Na^+, increases with increasing ionic concentration. However, we observe two different tendencies for structure-breaking ion like K^+. At a particular electrolyte concentration, the vicosity of the solution containing K^+ ions is lower than that compared to the solutions with structure-making ions. At qualitative level, this can be explained on the basis that structure-breaking ion should disrupt hydrogen bonding and thus increase the mobility of water molecules, with the opposite being true for the structure-making ions. However, we observe that the viscosity of the solutions containing K^+ ions increase with an increased concentration.

The presence of ions can have two compensatory effects on the dynamics of water molecules. The ions can disrupt the hydrogen-bonding network but also interact strongly with the water molecules.[58] The balance between these two effects can cause either an increase or a decrease in the water self-diffusion and viscosity. If

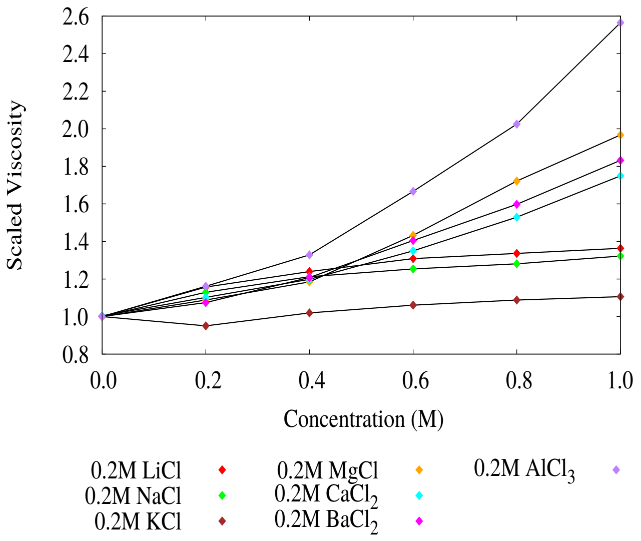

FIGURE 5.12: Viscosity of the electrolyte solutions at different concentrations. The viscosity values are scaled with respect to the viscosity of pure water at 298 K.
Source: Own elaboration.

the balance is subtle, the net effect can be temperature-dependent.[163]

The results presented in this study are inline with experimental results.[46,112,147,152] The values of viscosity calculated using MD simulations are shown in table **SI** B.7. We plot the scaled viscosity for the cases in this study in the figure 5.12. For the plots of energy and number of hydrogen bonds, the readers are referred to the figures **SI** B.15 and **SI** B.16 respectively. The values of the measured properties are scaled with respect to the properties of pure water *viz.* viscosity, number of hydrogen bonds and the potential energy at 298 K, as follows:

$$\mu_s = \frac{\mu}{\mu_0}; \qquad hb_s = \frac{hb}{hb_0}; \qquad PE_s = \frac{PE}{PE_0} \tag{5.4}$$

where, μ represents viscosity, hb represents the number of hydrogen bonds and PE represents the interaction energy. The subscritps s and 0 represents the scaled and pure water properties, respectively. Figure 5.12 indicates that the viscosity effect correlates with the charge density, that is, the viscosity of the electrolyte solution increases with an increasing charge and decreasing size of the cation.[60]For a given concentration of electrolyte, the viscosity of the solution containing chaotropic cation, K^+ in this case, is lower than that containing kosmotropic cation. As described above, chaotropic cations disrupt hydrogen bonding and hence reduces the bulk vicosity of the solution. We find that the number of hydrogen bonds does not differ significantly in the electrolytic solutions containing the cations of the same group in the periodic table at a given concentration[43] (cf. figure **SI** B.16) and there is an overall reduction of hydrogen bonds with increase in concentration of electrolytes. We, however, observe notable differences in the values of viscosity among the solutions containing cations of the same group at a specific concentration. This suggests that the dimension of the water clusters around the cations cannot be correlated with the behavior of the viscosity. This finding is inline with that reported by Corridoni et al.[61] When an ion substitutes a water molecule in the solution, it may push in or draw out its first neighboring water molecules, relative to their original position, depending on its size i.e. a steric effect. This local change of the microscopic structure affects both the energy landscape experienced by neighboring water molecules and their local density. Hence, we focus on the energy content of each system. We find that the total kinetic energy of all the systems in equilibrium at 300 K is approximately constant, while there are significant differences in the potential energies between the systems in this study. Hence, the change in viscosity induced by steric effects may be correlated to the change in overall interaction energy of the system (cf. figure **SI** B.15).

5.4.3 Effect of ion on the surface tension of electrolyte solution

The calculated values of surface tensions of pure water and all the electrolyte solutions in this study are shown in figure 5.13. We find that the surface tension of pure water is 62.86 mN/m which is inline with other theoretical studies using SPC/E water model.[217,306]

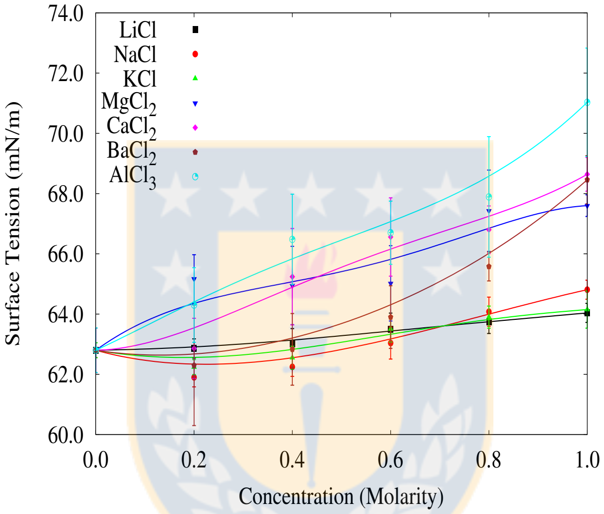

FIGURE 5.13: Surface tensions of different electrolyte solutions at varied concentration under study at 300 K. Source: Own elaboration.

Figures in **SI** B.17 show the water and ionic-number-density profiles for all the ions used in this work at the concentration of 1 molL^{-1}. All the ionic density profiles reach a plateau at the center of the film. We observed that the ions are preferentially excluded from the vicinity of the water/vapor interface.[157] We observe that the cationic and anionic densities are different implying that there is an exclusion related to the particular ion polarity at the vicinity of interface, with chloride ions residing nearer to the interface (see **SI** B.17).[156,229] We observe that the ion exclusion at the interface depends upon the charge density of the cations with higher exclusion observed in the case of system with aluminium ions. In a different study, Jung-Wirth and Tobias[156] used a polarizable-potential model for a series of sodium halide salts and water and observed that the cationic and anionic density profiles for NaCl at 1.2 M show some charge separation with the Cl^- ion residing closer to the interface. We do not observe a precise ion exclusion for the cases with Li^+, Na^+ and K^+ ions, while it can be observed for other cases, indicating that it depends on the polarizing power of the cations. We are not able to capture the ion exclusion effect at the interface in the cases with Li^+, Na^+ and K^+ ions due to the lack of polarizing potentials. We avoid using polarizable force fields due to its high computational cost which would restrict the use of large system size and long simulation time required for the present study. Nevertheless, results obtained in this study are inline with those obtained for monovalent ions by Bhatt et al.[27]

We compute the total number of interfacial hydrogen bonds in the electroyte solutions (see figure **SI** B.18) and observe that the total number decreases for higher concentration and is inline with our previous finding (see figure **SI** B.16). The missing interfacial hydrogen bonds give rise to a large positive enthalpy of hydration and hence to a free energy change.
However, we do not observe a significant difference between the surface tensions among the electrolyte systems which indicates that the surface tension is only slightly effected by the type of cations.[229]

5.4.4 Effect of ion on equilibrium contact angles made by electrolyte solutions on an amorphous hydrophilic silica slab

For a flat, rigid and chemically homogeneous surface, the contact angle can be predicted by Young-Laplace equation 5.5 and is related to surface tension (γ).

$$cos\theta = \frac{\gamma_{sv} - \gamma_{sl}}{\gamma_{lv}} \tag{5.5}$$

where γ_{sv}, γ_{sl}, γ_{lv} is the surface tension between the solid and gas (vapor), solid and liquid, and liquid and gas, respectively. In general, θ increases when γ_{lv} decreases; in other words, fluids with lower γ_{lv} easily wet the solid surface. In the previous section, we calculated the surface tension of the electrolyte systems used in this work and observed that the γ_{lv} of the systems do not change significantly among the cations of the same group while, slight increase can be observed between those of different groups along the periodic table. This implies that, the contact angles of the electrolyte solution on a hydrophilic silica slab should follow the same trend as the change in liquid-vapor interfacial tensions. However, other factors that determine the equilibrium water contact angle are the interaction energy of the solid-liquid interface, which can be translated into the Gibbs free energy of adhesion, and the intermolecular cohesive energy of the solution.

To this end, we calculated the water contact angles of all the electrolyte solutions used in this study on a hydrophilic silica slab at PZC as shown in figure **SI** 5.14. The contact angle of pure water on the silica slab has been reproduced in our previous study[343] and found to be 19.6^o. We observe a non-linear dependence of equilibrium contact angles in relation to the concentration. The contact angles increase with the concentration of the electrolyte solutions. In the previous section, we have observed that the number of interfacial hydrogen bonds decreases with the increase in electrolyte concentration of a solution (see figure **SI** B.18), however, the total intermolecular potential energy of the system increases (see figure **SI** B.15). In this regard, we calculate the interaction energies of the solution (water-water, water-ion) and slab-solution to estimate the tendency of adhesive and cohesive forces in the system (cf. figures 5.15 and 5.16).

We observe that both the solution-solution and solution-slab interaction energies increase with concentration, however, the increase in solution-solution interaction energy (cohesive energy) is higher than the increase in slab-solution adhesion energy. Hence, it can be inferred that at PZC of the hydrophilic silica slab, the increase in contact angle with increasing concentration of electrolyte solution is dominated by the increase in cohesive energy of the system.

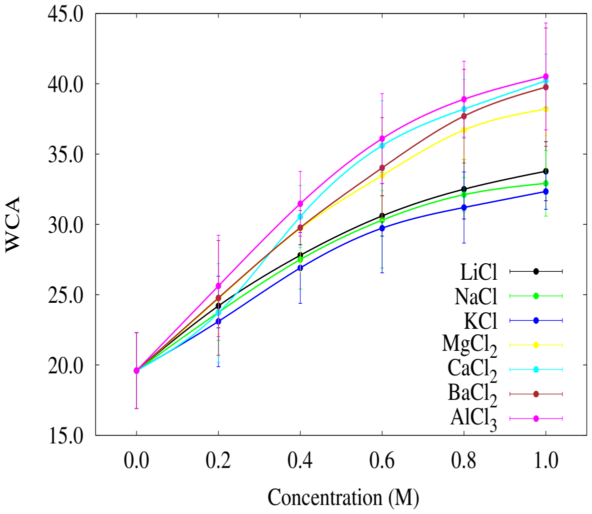

FIGURE 5.14: Contact angles of electrolyte solutions in relation to the concentration on a hydrophilic silica slab.Source: Own elaboration.

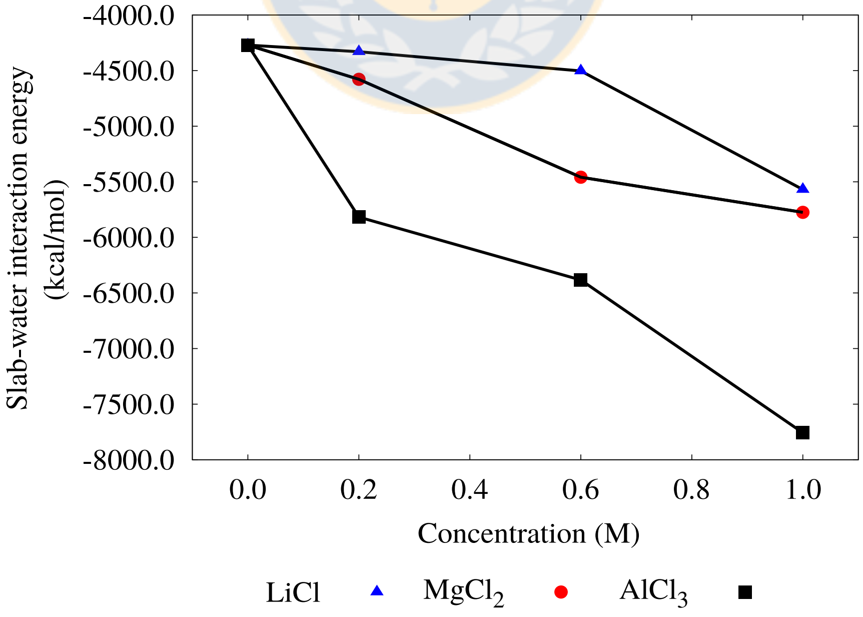

FIGURE 5.15: Interaction energy of the electrolyte solutions with the hydrophilic silica slab in relation to the concentration on a hydrophilic silica slab. Source: Own elaboration.

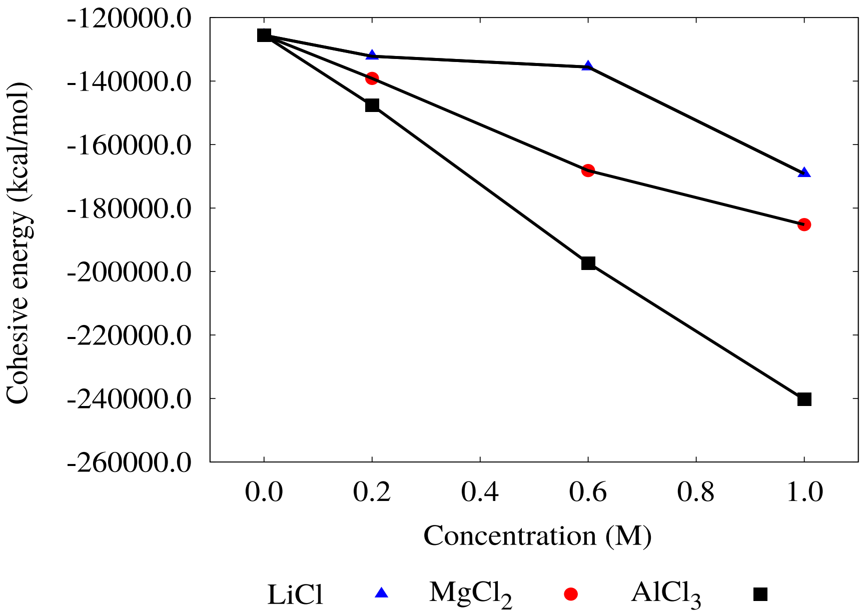

FIGURE 5.16: Cohesive potential energy of the electrolyte solutions in relation to the concentration on a hydrophilic silica slab. Source: Own elaboration.

5.4.5 Effect of ions on the nanocapillary imbibition of electrolyte solutions into a hydrophilic silica channel

Having discussed the effect of electrolyte in the most relevant properties that determine the capillary filling, we now analyze the nanocapillary imbibition of the electrolyte solutions in a 6 nm wide hydrophilic silica channel. We observe that filling rates are determined by the complex interplay between the wettability of the solution, electro-viscosity and the surface tension effects, that in turn are affected by the type of ions present in the solution and their particular concentration. The observed filling rates of different electrolyte solutions suggest that those containing structure breaking cations like K^+ have higher filling rates as compared to structure making cations, as the former tend to have lower viscosity owing to the reduced ion-water interaction energy and higher disruption of hydrogen bonds (cf. figure 5.12). We also observe that the filling kinetics can be described by the modified form of Bosanquet's equation[159], which is a force balance equation where inertial and viscous forces acting on the fluid during the imbibition process are balanced by capillary force created due to Laplace's pressure of the curved meniscus. The fit of the modified Bosanquet's equation to the capillary filling of the electrolyte solutions indicates that the momentum and viscous effects are predominant during the filling process.

The dashed lines in figure 5.17 compares the prediction of Bosanquet's equation with those in simulation data and depict an initial constant velocity regime. This regime, also termed as inertial regime, is characterised by constant filling velocity during which viscous effects are negligible.[159,223]

In our previous study of nanocapillary filling of pure water ,[159] we have showed that the velocity of the fluid during inertial regime depends on the initial contact angle made by the fluid with the channel entrance. In this study, we observe that, for dilute solutions, the initial filling rates depends on the type of cation (valency and size) and not on the particular concentration of the ions in the solution. However, the duration of the inertial regime i.e. inertial time depends both on the

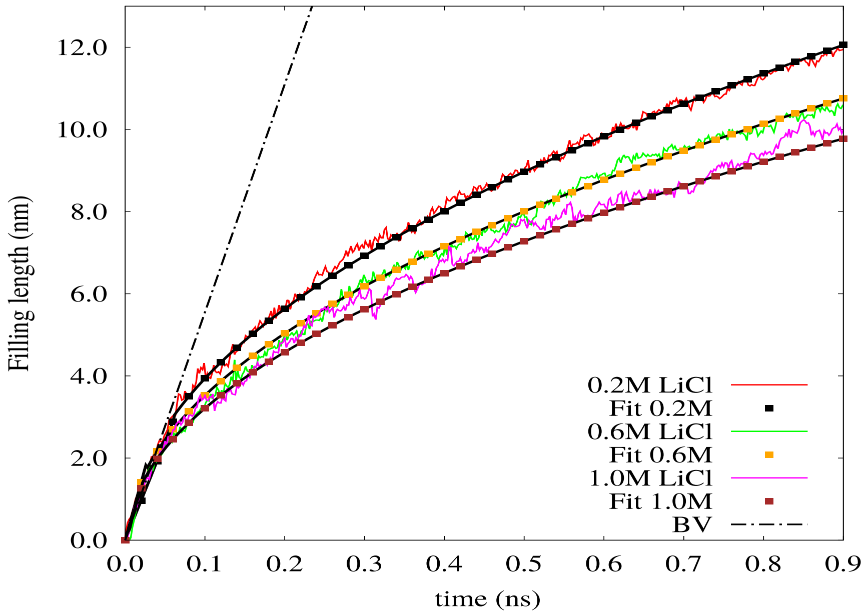

FIGURE 5.17: Comparison of simulation data of capillary filling in a 6 nm wide hydrophilic silica nanochannel with that predicted by Bosanquet's model for LiCl solutions. BV refers to the Bosanquet's initial velocity at the channel entrance. The solid filled dotted lines are those predicted by the modified[159] Bosanquet's model[35], while the solid colored lines are simulation data. The dashed lines correspond to a linear regression in the constant velocity regime. Source: Own elaboration.

type and concentration of the cations. The simulation data are fitted to the modified[159] Bosanquet's equation where the original model developed by Bosanquet (cf. equation 5.6)[35] is modified to include the dynamic contact angle made by the fluid meniscus with the channel walls (ca. equation 5.9).

$$l(t)^2 = \frac{2A_I^2}{B}[t - \frac{1}{B}(1 - exp(-Bt))] \tag{5.6}$$

A and B in the above equation are given by

$$A = \sqrt{\left(\frac{2\gamma cos\theta}{\rho H}\right)} \tag{5.7}$$

$$B = \frac{12\mu}{\rho H^2} \tag{5.8}$$

where, A corresponds to the initial velocity at the entrance.
The equilibrium contact angle in equation 5.6 is assumed to be attained instantaneously which is contrary to more recent studies.[36,63,81,82,149,265,267] Hence, it is important to account for dynamic contact angle (DCA) in Bosanquet's equation to adequately explain the capillary rise. In our previous study, we proposed that the DCA, which can only be seen when the viscous force starts predominating the inertial effects of the fluid during the imbibition, can be modeled by equation (5.9).

$$cos\theta_d = \begin{cases} cos\theta_i & \text{for t} \leq t_i \\ cos\theta_e\left(1 - exp\left(-\frac{t}{\tau}\right)\right) & \text{for t} > t_i \end{cases} \tag{5.9}$$

In the above equation, τ is proportional to characteristic time for fully developed flow and is given by equation 5.10,[20] t_i refers to the time during which the inertial regime persists and θ_i is the initial contact angle made by the liquid with the nanochannel walls while θ_e is the final equilibrium contact angle made by a drop of solution on a solid surface.

$$\tau = 2.132\left(\frac{H^2\rho}{\mu}\right) \tag{5.10}$$

From the MD trajectories, we computed the filling velocity (calculated velocity in table 5.6) and calculated the effective angle at the channel entrance as an average of the angles made by electrolyte solutions with the upper and lower slab respectively during the inertial regime. Theoretically, we estimated the fluid velocity at the channel entrance using equation 5.11.

$$\nu_0 = \sqrt{\left(\frac{2\gamma cos\theta_0}{\rho H}\right)} \tag{5.11}$$

where, ν_0 is the initial velocity of the fluid at the channel entrance and θ_0, the initial angle made by the fluid with the channel walls at the entrance.

The similarity between the calculated values of initial velocities using equation 5.11 and those estimated from the atomic trajectories obtained from MD simulations (see table 5.6) suggest that the overestimation of initial velocity in the original Bosanquet's equation during the inertial regime is due to the assumption that the equilibrium contact angle is attained right at the channel entrance.[223] The influence of ions in electrolyte solutions and their effect in the imbibition process merits an explanation. We have showed that the viscosity and the surface tension of the imbibing electrolyte solutions are affected both by the cation types and their concentration. Nevertheless, surface tension is only slightly affected by cations. The excellent fit of the modified Bosanquet's equation with the filling rates of the electrolyte solutions extracted from the simulation data indicates that the interaction of these solutions with the nanochannel wall at PZC does not significantly modify the interfacial fluid-wall behavior within the range of concentrations under study. This can be explained on the basis that the small number of ions and the short time scale of nanocapillary imbibition in the present work makes the process of wall-ion interaction stochastic and uncorrelated with the concentrations[15] and hence, makes the filling kinetics independent to the ion-wall interactions. However, the fit of Bosanquet's equation to the simulation data indicates that the filling kinetics is governed by the enhanced viscosity due to the presence of ions in water.

5.5 Conclusions

In summary, we have presented a study on the effect of ions in the nanocapillary imbibition in a hydrophilic silica nanochannel at PZC. The results suggest that the filling kinetics in all the cases is altered by hydrodynamic forces enhanced by the viscoelectric effects due to the presence of ions in the electrolyte solution. We find that the presence of cations does not significantly affect the surface tension while the viscosity depends both on the type and concentration of the cations in the electrolyte solution. For a particular concentration, viscosity of the electrolyte solution depends upon the type (structure maker or breaker) and charge density of the cations present in the electrolyte solution. We also observe that the filling

TABLE 5.6: Values of the important parameters during initial rise

Salt type	Conc.	E. vel(nm/ns)	C. vel(nm/ns)
LiCl	0.2	57.5	53.3
	0.4	57.5	49.9
	0.6	62.5	63.9
	0.8	62.5	58.4
	1.0	62.5	65.1
NaCl	0.2	65.2	64.1
	0.4	63.6	60.9
	0.6	63.8	61.2
	0.8	62.5	63.9
	1.0	64.3	67.2
KCl	0.2	71.5	68.8
	0.4	71.5	72.1
	0.6	71.5	73.5
	0.8	71.5	70.1
	1.0	71.5	67.3
$MgCl_2$	0.2	57.5	53.1
	0.4	57.5	55.2
	0.6	60.5	63.8
	0.8	60.5	64.1
	1.0	60.5	68.1
$CaCl_2$	0.2	65	68.9
	0.4	66	65.2
	0.6	66.5	67.1
	0.8	62.5	65.3
	1.0	62.5	59.1
$BaCl_2$	0.2	52.5	46.1
	0.4	52.5	48.8
	0.6	40.5	38.5
	0.8	40.5	43.9
	1.0	40.5	34.2
$AlCl_3$	0.2	68.2	73.1
	0.4	70	72.7
	0.6	70.1	68.1
	0.8	70.3	65.9
	1.0	70.7	76.3

Conc.=electrolyte concentration,E.vel=estimated velocity using equation 5.11, C.vel= velocity calculated from the atomic trajectories. Source: Own elaboration.

flow rate of the imbibing solution in the hydrophilic silica nanochannel at PZC depends both on the type and concentration of ionic species present in the electrolyte solution. Our results indicate that the filling rate decreases with increase in concentration of cations for all the cases, while for a particular concentration, the filling rate increases or decreases depending upon the type of cation. For instance, solution containing structure breaker ions like K^+ has higher filling rate than those containing structure maker ions like Li^+ and Na^+, at a given concentration. Our study provides a new insight into the physics of the effect of hydration of ions and concentration in the capillary imbibition of electrolyte solutions at PZC in hydrophilic silica nanochannels.

Chapter 6

Effect of external electric fields on capillary imbibition of water in silica nanochannels

Parts of this chapter has been published in: Effect of an external electric field on capillary filling of water in hydrophilic silica nanochannels.(N. Kumar Karna, A. R. Crisson, E. Wagemann, J. H. Walther and H. A. Zambrano, Physical Chemistry Chemical Physics, 2018, 20, 18262–18270)

6.1 Outlines

Development of functional nanofluidic devices requires understanding the fundamentals of capillary driven flow in nanochannels. In this context, we conduct molecular dynamics simulations of water capillary imbibition in silica nanoslits under externally applied electric (E) fields with strengths between 0 to 1 V/nm. For increasing E-fields, we observe a systematic lowering in the meniscus contact angle and a decrease in the corresponding water filling rates. These results contrast markedly the classical Washburn-Bosanquet's equation which predicts an increase in filling rates for lower water contact angles. Our study provides evidence that the observed decrease in water filling rates can be attributed to the interplay between two underlying mechanisms, a reduced fluidity of interfacial water and a systematic alignment of the water molecules in the bulk as a response to the particular strength of the applied E-field. Therefore, during water capillary filling a constant E-field applied in the direction parallel to the water imbibition leads to a lower than expected filling rate caused by a viscosity increase in the bulk and an altered solid-liquid friction on the channel walls. These coupled mechanisms governing capillarity under the action of applied E-fields could be manipulated for controlling imbibition of polar liquid solutions in nanofluidic devices.

6.2 Introduction

Fabrication techniques have evolved dramatically over the last decade[41,121,185] making possible to build artificial liquid conduits on length scales comparable to the size of ultra-efficient biological channels.[111] This realization offers new opportunities in the development of functional multistage microdevices integrated by nanoscale pores and channels[329] which may have tremendous implications in a number of foreseeable biological,[94] chemical[220] and technological applications.[289] In fact, recent advances in nanofluidics have triggered a number of new

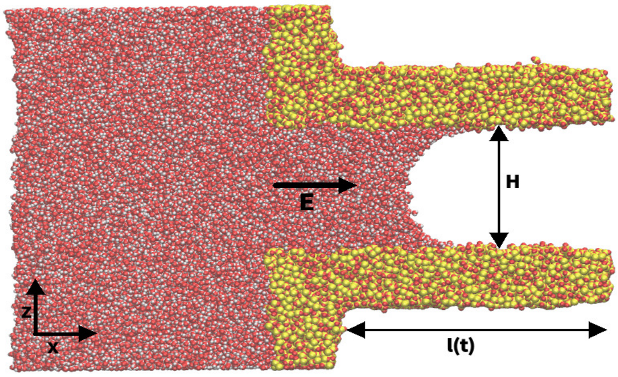

FIGURE 6.1: A snapshot of capillary filling for 7-nm silica nanochannel. The electric field (E) is applied in the direction of nanocapillary imbibition. Source: Own elaboration.

high impact technologies such as high throughput techniques,[49] drug delivery[268] and biomolecular analysis.[225]

Water is an essential material in our everyday life and is the most used solvent in technological applications.[126] Moreover, water in nanoconfinement plays a key role in the controlled transport of species through biological cellular membranes,[111] in water desalination systems[172] and in novel sensor technologies.[328] Therefore, achieving precise control of water imbibition and transport in nanoscale structures is crucial to enable the design of more efficient processes and to develop a new generation of promising microdevices. Nevertheless, there are a number of challenges and opportunities associated with controlling water flow in nanochannels. Several studies have shown that water in nanoconfined geometries exhibits unexpected behaviors as compared to those observed in macroscale systems.[47,166,177,183,333] For instance, the presence of interfaces distorts the near H-bond network of water and as a result of the ultra high surface to volume ratio inherent to nanoconfinement, altered interfacial properties greatly influence the static and dynamic behavior of water in nanochannels.[176,185,221,330,331] In addition, water molecules are highly polar and hence, molecular ordering of water within ultraconfined structures can be altered by exposure to electromagnetic fields.[241,307,331] In this context, a variety of techniques like direct modification of the surface charge density,[237,252] surface embedded electrodes[99,342] and electric,[241,264,332] and magnetic far field effects[258] have been used for manipulation of aqueous solutions in nanoconfinement. Furthermore, recent studies have revealed the significant effect of varying external applied electric fields on flow control by tuning the electrical double layer thickness,[16,342] the electro-osmotic flow velocity[50,70,206] and the pressurized water flow rates.[253].
In an interesting experimental study by Xue et al[335], the authors report increase in imbibition rate of KOH solutions inside nonoporous gold under the influence of externally applied potential.

In the present study, we analyze the effect of an externally applied electric field on capillary flow of water in hydrophilic silica nanochannels (cf. figure 6.1). It is well established that the driving force in capillary flow is determined by a balance between the Laplace pressure[75,173] and a drag with variable contributions from inertia and viscous friction.[35,223] Indeed, the Laplace pressure is directly related to the surface tension acting on the curved interface at the advancing capillary front whose curvature in turn is dependent on the surface wettability of the channel walls. Furthermore, wettability is quantified by measuring the water contact angle which is mainly determined by the particular strength of the solid-liquid interactions.[64,108,332] In previous studies, we reported the relation between dynamic contact angle, height of nanochannels and capillary filling flow rates.[159,223] Specifically, we found that the initial filling rate depends upon the particular value of the contact angle made by the fluid at the entrance of the nanochannel, and is given by:

$$U_i = \sqrt{\left(\frac{2\gamma \cos\theta_i}{\rho H}\right)} \tag{6.1}$$

where, U_i corresponds to the initial flow velocity and θ_i is the initial value of the contact angle made by fluid at the channel entrance.

In capillary filling under the influence of an externally applied electric field, the meniscus contact angle of the imbibing fluid can be predicted by the Young-Lippmann (Y-L) equation[67,170]

$$\cos\theta = \frac{\gamma_{sg} - \gamma_{sl}}{\gamma_{lg}} + \frac{\langle \epsilon_0 \epsilon \mid E \mid^2 D \rangle}{2\gamma_{lg}} \tag{6.2}$$

where θ is the equilibrium contact angle, D, the thickness of the solid-liquid interfacial layers, γ, the surface tension of the liquid, E, the applied electric field, ϵ, the dielectric constant of the liquid and ϵ_0, the permittivity of free space. The subscripts l, g and s refer to the liquid, gas and solid, respectively, and the angular bracket stands for the average over D. The average interaction between a free dipole (μ) and electric field (E) at temperature T is $\sim\mid \mu \mid^2\mid E \mid^2 /(3k_B T)$[67], where k_B represents the Boltzmann's constant. The Y-L equation indicates that contact angle depends only on the absolute strength of the field regardless of its direction. However, deviations from these predictions have been reported in studies of water contact angles at hydrophobic surfaces under different electric field strengths at the nanoscale.[67,270,271,325] Qualitatively, the Y-L equation indicates lowering of contact angle for increasing applied electric field and hence predicts, at first glance, higher capillary pressure with increase in electric field strength during imbibition in hydrophilic nanochannels. Nevertheless, the application of an electric field during the capillary filling of water in nanochannels could affect not only the meniscus contact angle[270] but also other properties such as viscosity,[352] dielectric constant,[339] temperature and surface tension[318] among others[253,352] and therefore, it might be challenging to predict the effect of an electric field applied during the water imbibition process at nanoscale.

In this work, from large scale molecular dynamics simulations of water imbibition in the presence of an electric field applied in the direction parallel to the flow, we report the time evolution of the capillary front position and the instantaneous meniscus contact angle during the capillary filling of a 7 nm high nanoslit. The strengths of the electric fields applied to the system range from 0 to 1 V/nm. These field strengths are in the range of those produced by charged electrodes,[317] biological ion channels,[337] electric-field-directed assembly of biomolecules[348] and electroporation processes.[341] It should be noted that in experiments the effective electric field differs significantly from the applied field because the actual field is lowered by the orientational polarization of water.[87,270] Therefore, in the bulk phase, the exact relation (for the absolute values of the field) is given by[98]

$$E = \frac{3E_0}{\epsilon_r + 2} \tag{6.3}$$

where E_0 is the applied electric field, and ϵ_r is the relative permittivity, defined as the ratio of effective permittivity of the medium (ϵ) to the absolute permittivity of free space (ϵ_0). Moreover, the strength of the electric field used in the present study are weak enough to avoid decomposition of water molecules.[260] In our simulations, the application of an electric field exerts a force $F = q_i E$ at the center of mass of each atom according to the partial charge q_i on each corresponding atom which is discussed in detail elsewhere.[87,270,342] As water molecules are electrically neutral but highly polarized, the effect of an external electric field on water is a torque which reorients each molecule in the direction of the applied field altering the overall hydrogen bonding network.[45,253] Furthermore, under the influence of an increasing external electric field, water molecules may experience progressive reduction in the degrees of freedom.[108,285,331]

6.3 Computational method

To elucidate the effect of externally applied electric fields in capillary filling of water in hydrophilic silica nanopores, we conduct a series of all-atom MD simulations using FASTTUBE, a molecular dynamics simulation package which has widely been used to investigate fundamental fluid dynamics under nanoconfinement.[159,222,223,314,315,342] Water molecules are described using the simple point charge SPC/E model[24] and the silica atoms by the TTAMm model developed by Guissani and Guillot[114] which is a modification of the original TTAM model.[297] Water-silica interactions are described using Coulomb and Buckingham potentials calibrated in our previous study[343] wherein the experimental value of the water contact angle reported by Thamdrup et al.[290] in studies of capillary filling is used as criterion to calibrate the potential parameters. For further details of the potentials used here, we refer readers to Zambrano et al.[343] We have chosen the SPC/E water model not only to be consistent with our previous works,[159,223,314,343] but also due to its simplicity and quantitative agreement with experiments to yield water reorientation and hydrogen bond dynamics.[108,254,255,263,352] Moreover, studies have found that the value of the surface tension for the SPC/E model is in good agreement with experimental results.[306]

6.4 Results and discussion

Influence of electric field in wettability

We first study the effect of electric field strength on water wettability of a silica slab by evaluating the water contact angle (WCA) on a hydrophilic amorphous silica surface. For this purpose, we perform simulations of a cylindrical nanodroplet,[322] consisting of 3000 water molecules mounted on a silica slab of 37.92 nm × 2.584 nm × 3.5 nm in vacuum using a time step of 2 fs. To equilibrate the water droplet-silica system, we follow the methodology described by Zambrano et al.[343] and references therein. Further, we allow a cylindrical water droplet to spread on a frozen silica slab under different electric field strengths with the field applied parallel to the solid surface. A Berendsen thermostat[25] is

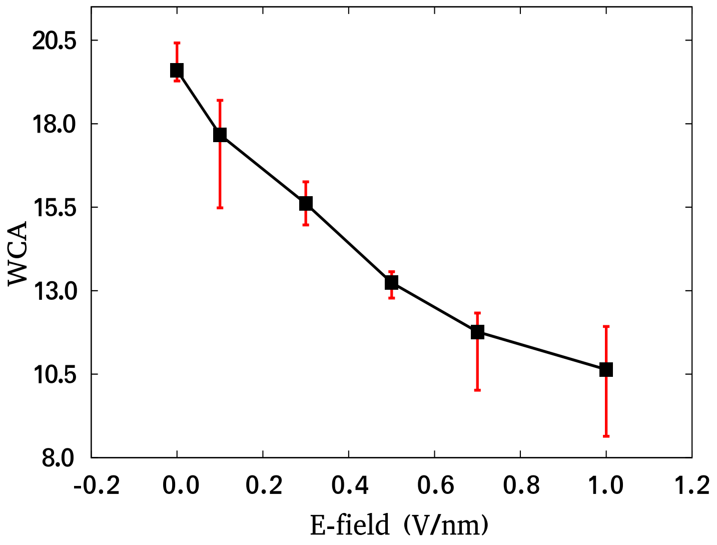

FIGURE 6.2: Water contact angle (WCA) on a hydrophilic silica slab at different electric field strength. The electric field is applied parallel to the surface.
Source: Own elaboration.

connected to the water molecules with a weak coupling constant of 0.1 ps to maintain a constant temperature of 300 K. We use the Berendsen heat bath to control the system temperature as this thermostat may have advantages over other methods used in nonequilibrium simulations of viscous flow.[52,253] The equilibrium value of water contact angles are obtained as the average value for snapshots extracted every 50 time steps from trajectories computed after 5 ns of equilibration.[270,271] The values of the water contact angles on the silica surface in either the absence or presence of externally applied fields are plotted in figure 6.2. The equilibrium WCA in absence of electric field is measured to be ca. 20° which is in accordance with the value previously reported.[343] Meanwhile, a significant decrease in WCA can be observed with increasing electric field strength, which indicates that the magnitude of the applied electric field has a strong effect in the final equilibrium state of the droplet.[255,270,270]

Influence of electric field in the bulk viscosity of water

In the present study, we calculate the viscosity of bulk water using the periodic-perturbation method developed by Hess,[127] where the viscosity of liquid water is calculated by applying an external force on each water molecule. The applied force is a function of height (z) of the simulation box. For details of the viscosity calculation using this method, readers are referred to the studies by Hess[127] and Sunda et al.[283] We plot the scaled viscosity (μ_s) of bulk water at different field strengths as shown in figure 6.3, where,

$$\mu_s = \frac{\mu_f}{\mu_0} \tag{6.4}$$

μ_f and μ_0 represent the bulk viscosities of water, with and without imposed electric field respectively. Within the range of electric field considered in this study, the viscosity increases linearly with increasing field strength. The maximum change in viscosity between the cases with the maximum applied field and without electric field respectively is found to be ca. 20 %. These results are in line with those

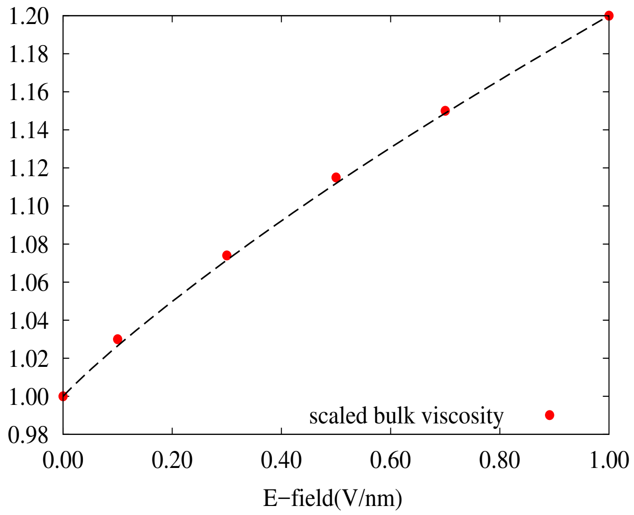

FIGURE 6.3: Scaled viscosity calculated from the Periodic perturbation method at different electric fields. The dotted lines represent the linear tendency of the change in viscosity while the points are the measured values. Source: Own elaboration.

reported by Zong et al.[352] using non-equilibrium molecular dynamics, who observed that the dipole moment of the water molecules in bulk align along the direction of the applied electric field resulting in a monotonic increase of the bulk viscosity of water with electric field strength.

Effect of electric field on capillary imbibition in silica nanochannels

To study the capillary imbibition of water in silica nanochannels in the presence of an external electric field we build a channel with height of 7 nm using parallel walls consisting of amorphous silica slabs as shown in figure 6.1. For the details of the slab construction and amorphization, readers are referred to our previous studies.[159,343] Simulations are conducted in a periodic orthorhombic cell with size of 2.52 nm × 43.0 nm × 20.88 along the x, y and z axis. Part of the simulation box is filled with 23,600 water molecules to reproduce the density of water in bulk. In all the simulations of imbibition, the water molecules are coupled to a Berendsen[25] heat bath with a coupling constant of 0.1 ps at 300 K during 1 ns; then, the thermostat is disconnected and the simulations are conducted in the microcanonical ensemble (NVE) for 3 ns until the system is equilibrated. Next, the electric field is applied and the system is further allowed to relax for 1 ns after which the water slab is released from rest to move spontaneously towards the silica channels. We notice that the electric fields are imposed, for all the cases, in the direction parallel to the water capillary imbibition.

The viscous Joule heat is extracted during the filling connecting a Berendsen thermostat to the water molecules with a weak coupling constant of 0.1 ps while atoms of the channel walls are fixed to their equilibrium positions.[87] In particular, the use of a Berendsen heat bath to control temperature could not be ideal[87] however previous studies have reported, for water under electric fields, satisfactory results using a Berendsen thermostat with proper values of the coupling constant which ensures maintaining the target temperature without large oscillations.[86,87,249]

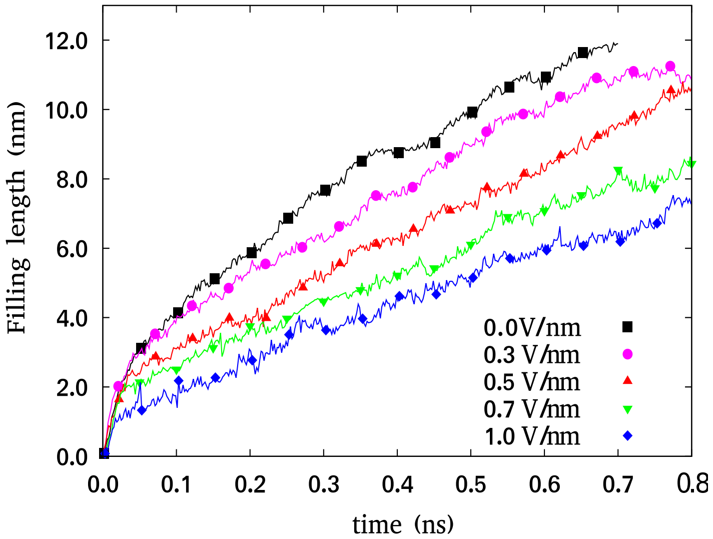

FIGURE 6.4: Nanocapillary imbibition length as a function of time in a 7 nm-high channel for different strength of electric field. The constant filling rates for all the cases of electric field indicates an inertial regime independent of initial conditions. Source: Own elaboration.

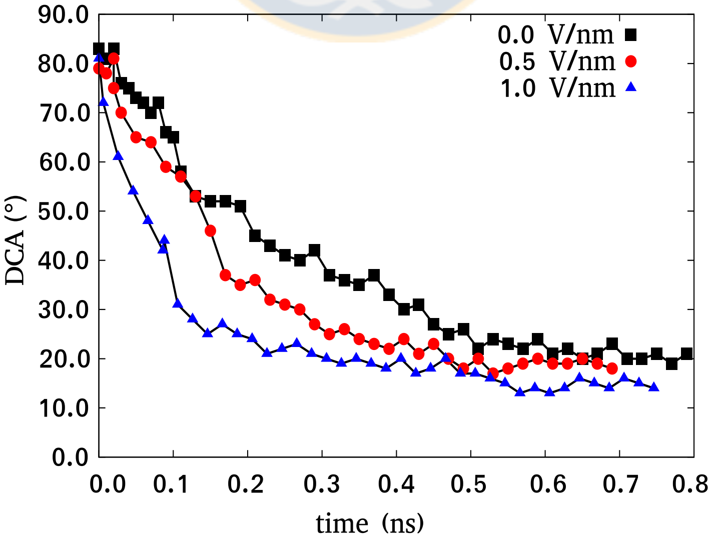

FIGURE 6.5: Measured dynamic contact angle (DCA) in a 7 nm-high channel at various electric field strengths. Source: Own elaboration.

During water spontaneously filling the channels, the instantaneous positions of the advancing capillary front along the direction of the water flow are tracked to estimate the penetration length of the liquid as a function of time (cf. figure 6.4). The initial capillary front velocity (u_i), the duration of the inertial time (t_i) and the dynamic contact angles for each simulation during nanocapillary imbibition are computed from the atomic trajectories. The physical mechanisms behind the dynamics of water filling a nanochannel with an applied electric field can be rather complex owing to coupled factors such as the water molecules-electric field interactions, the intermolecular forces between species in the system and the variable population of hydrogen bonds in water.[67,212] Therefore, to evaluate the effect of an applied electric field on the contact angle of the advancing capillary front, we compute the dynamic contact angle (DCA) during water imbition in the silica nanochannel (cf. figure 6.5). For details about extracting DCA values during the water imbibition, the readers are referred to our previous study.[159]

We observe that the dynamic contact angles measured during the capillary imbibition in either the absence or presence of externally applied fields (cf. figure 6.5) are consistent with the values computed of equilibrium WCA of nanodroplets as shown in figure 6.2. For instance, figure 6.5 shows that the DCA value for the case without applied field (black squares) evolves from an initial value of ca. 84° until attaining a constant value of ca. 21° while for the case with the highest applied field (blue triangles), the DCA evolves from the same initial value until attaining a constant value of ca. 13°, similar to the corresponding equilibrium WCA values shown in figure 6.2. Therefore, our results reveal a substantial decrease in both the dynamic and static contact angles as higher electric field are applied suggesting a significant field-dependent increase in the Laplace pressure at the capillary meniscus.

In figure 6.4, we plot temporal evolution of the imbibition length for different electric field strengths. The time evolution of the imbibition lengths during the initial stage of the filling is linear irrespective of the strength of the imposed electric field which indicates a capillary flow with constant velocity at the channel entrance confirming, for all the cases, the existence of an inertial regime as predicted by Bosanquet.[35,66,159,168,223] This insensitivity of the meniscus speed to the particular strength of the imposed electric field implies that the initial contact angle (ca. 80°) at the channel entrance does not depend upon the strength of the applied field and should remain constant during the inertial regime, in line with the results in our previous study[159]. Nevertheless, figure 6.4 also indicate that the inertial time[223], during which retarding inertial forces dominate capillary filling, decreases with increasing strength of the applied field. These shorter transition times suggest that properties in the imbibed water vary systematically with the strength of the applied electric field.

Once the flow transitions from the inertial to the viscous regime, the results clearly reveal that water filling rates decrease for higher magnitudes of the applied field in channels with the same height. We observe a difference of 40 % in the maximum imbibition velocity, measured at the center of the channel, during the viscous regime for the two extreme cases i.e. the case without applied electric field and the one with the maximum applied field of 1.0 V/nm (See Supplementary information). It should be noticed that a capillary meniscus with lower contact angle would imply a higher Laplace pressure[168,336] and thus, a higher filling speed. Therefore, a decrease in filling rates (figure 6.4) is in contradiction with the observed lowering of contact angle under increasing electric fields as shown in figures 6.2 and 6.5.

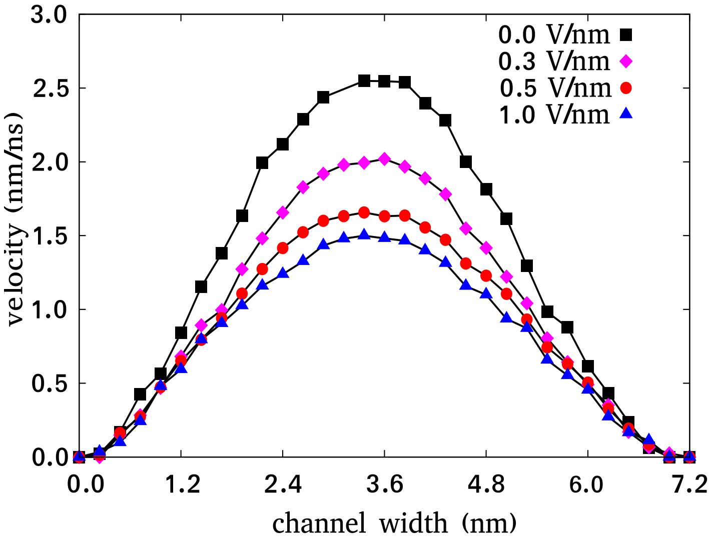

FIGURE 6.6: Velocity profile of Poiseuille flow for a slit silica channel with height of 7 nm at different applied field strengths. The maximum velocity computed at the center of the channel decreases with increasing applied field strength. Source: Own elaboration.

Another important aspect related to capillary imbibition is the surface tension of the imbibing liquid which for water, is closely related to the number of interfacial hydrogen bonds and has been reported in detail elsewhere.[217,270,277] Indeed, in presence of external electric fields, changes in the meniscus surface tension could potentially alter the Laplace pressure during capillary filling[19] and consequently modify the flow rates in the channel. Recently, the surface tension of water has been reported to increase within the range of electric field strengths under study here.[217] Therefore, indicating that the effect of the applied electric field on water surface tension is not an explanation of the decrease in filling rates observed in the present study.

Simulations of Poiseuille like flow in silica nanochannels

To understand the causes of this apparent contradiction, we performed further MD simulations of Poiseuille like flow in silica nanochannels with height of 7 nm. Considering water flow sufficiently far from the channel entrance and also far behind of the capillary front position is a scenario wherein it is acceptable to assume Poiseuille flow to study the influence of an electric field on viscosity during capillary filling. All the conditions during the study of Poiseuille like flow are maintained constant except for the strength of the axial electric field in the flow direction. We perform simulations at various field strengths viz. 0.0, 0.3, 0.5, 0.7 and 1.0 V/nm. We equilibrate the water for 3 ns in NVT and 3 ns in NVE ensembles, respectively. After water is equilibrated, a constant acceleration (gravity field) is imposed to each water molecule to reproduce a Poiseuille like flow through the silica channel. In order to extract the viscous heat, a Berendsen thermostat[25] with a coupling time constant of 0.1 ps at 300 K is connected to the water molecules. For additional details about the setup of the Poiseuille flow simulations, the readers are referred to Wagemann et al.[314] The production simulations are performed for 20 ns with an electric field applied in the flow direction. In all the simulations with Poiseuille like flow, a gravity field is applied to impose an acceleration of

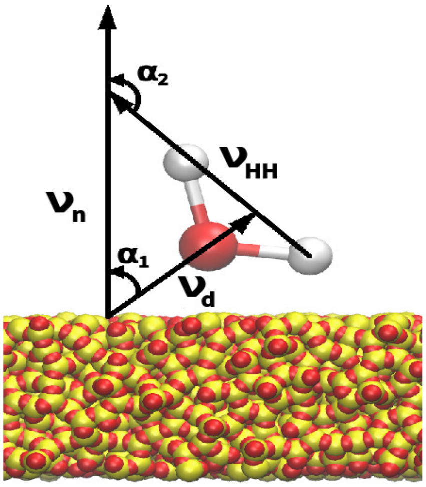

FIGURE 6.7: The angles considered to determine the orientation of the water molecules are given in terms of the angles α_1 and α_2. ν_d,ν_n and ν_{HH} are the vectors corresponding to the dipole moment, normal to the surface and that connecting the two hydrogen atoms, respectively. Source: Own elaboration.

$9.83 \cdot 10^{11}\ \mathrm{m/s^2}$, equivalent to a pressure gradient 10 bar/nm. Velocities are computed by averaging over the axial length after steady state velocity profiles have been reached, more details regarded the methodology can be found in our previous studies.[314]

The velocity profiles across the channel at various field strengths shown in figure 6.6 indicate that the maximum velocity decreases with increase in the strength of the imposed electric field. These results confirm our previous observations of reduced capillary filling rates with higher applied electric fields. We note that the $\sim$ 20 % increase in bulk viscosity at 1 V/nm reported in the previous section cannot account for the ca. 40 % decrease in maximum velocity observed for the cases with Poiseuille flow (See SI. C.1 for the plot of maximum velocity observed during visco-inertial regimes at different electric fields).

Orientation of water molecules under the influence of an external electric field

Now that we have discussed the effect on imbition of viscosity and surface tension under an externally applied electric field, we turn to the effect of electric field inducing water orientation and its influence on the observed lower than expected nanocapillary imbibition. To shed light into the problem, we measure the orientation of water molecules under nanoconfinement. The orientation profiles, describing water angle distribution, are defined by two specific angles: α_1 and α_2 as illustrated in figure 6.7, α_1 is the angle between the dipole vector ($\overrightarrow{\nu_d}$) of a single water molecule and the normal vector ($\overrightarrow{\nu_n}$) for the surface, while α_2 is the angle between ($\overrightarrow{\nu_{HH}}$), the vector from one H atom to the other in the same water molecule, and ($\overrightarrow{\nu_n}$). The preferred orientation of water molecules under external electric fields has been studied extensively in different systems.[67,253,352,353] Specifically, the response of nanoconfined water molecules to an externally applied electric field can be inferred from the orientation of the water dipole moment (cf. figure 6.8). In this figure, the probability distribution function (PDF) of the angle between the vector normal to the silica surface and the water dipole has been calculated at the

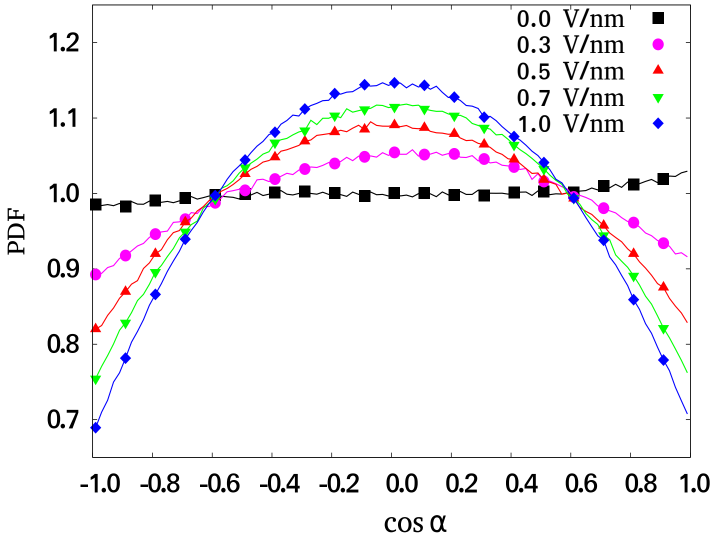

FIGURE 6.8: Probability distribution function of water dipole moment at a distance between 1.5–2.0 nm from the lower wall surface. Source: Own elaboration.

distance between 1.5 and 2.0 nm from the silica surface. We choose this distance as, for pure water, the effect of a solid surface does not significantly affect the water density beyond 1.5 nm (cf. figure 6.9) and hence, is considered to have bulk properties beyond this distance.[30,199] In fact, as shown in Supporting information (Figures SI. C.2 and SI. C.4), we observed a high preferential orientation of water molecules near the channel walls for all the cases with and without applied electric fields, in line with previous experimental studies.[199] However, the molecular orientation quickly vanishes in the bulk in absence of an external electric field (see figure SI. C.2). Conversely, in the presence of electric fields (see figure 6.8 and figure SI. C.3), we observe that the water molecules in the bulk orient themselves along the field with the oxygen atoms against, and the hydrogen, along the field direction.[253,270,352] Moreover, in the bulk, the water molecules for the highest strength of applied field display a preferential orientation of 80°–110° indicating that the dipole moment is nearly tangential to the channel wall surface.

To further study the structure of the water molecules in the channel, we consider the orientation of the vector that connects the two hydrogen atoms ($\overrightarrow{v_{HH}}$ in figure 6.7) which in other words indicates the particular plane wherein water molecules are localized. Our results show that the plane of water molecules tends to be oriented perpendicular to the wall surface with increase in the applied electric field strength (see SI. C.3). The position of the plane is indicated by the increased probability of orientation of the vector $\overrightarrow{v_{HH}}$ which points perpendicular to the surface wall. This preferential orientation suggests that the water molecules are highly structured with oxygen atoms oriented against the applied field with one OH bond pointing towards the surface and other towards the bulk. Nevertheless, we infer that the interaction with the partial charges of surface silicon and oxygen atoms leads to water molecules with suppressed translational and rotational freedom near channel walls which results in a slowdown of the interfacial water dynamics.[123] In accordance with this, the distribution function of water dipole angle with the normal to the wall surface reveals that the water molecules in the bulk are more prone to respond to the particular strength of the applied field[352] (cf. figure 6.8) compared to water molecules near the wall surface (See SI.

TABLE 6.1: Parameters of equation 6.6 under different magnitudes of electric field at 300 K

E-field (V/nm)	$\frac{D_{bulk}}{D_{app}}$	$\frac{\mu_{eff}}{\mu_{bulk}}$	Contribution (%) to the effective viscosity
0.0	1.66	1.10	10%
0.5	1.41	1.06	6%
1.0	1.30	1.05	5%

Source: Own elaboration

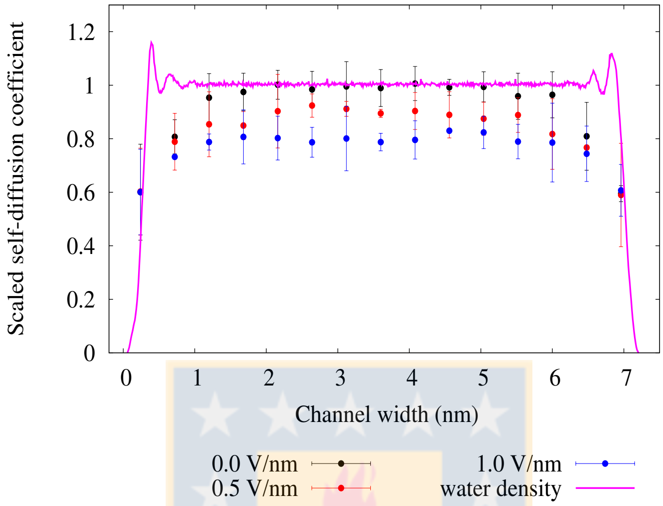

FIGURE 6.9: Coefficient of self-diffusion of water along channel width. The solid line represents the density of water and the dots with error bars represent the scaled self-diffusion coefficient of water calculated using the Stokes-Einstein relation.
Source: Own elaboration.

C.4). This differential response of water molecules across the channel to externally applied electric fields can affect the overall hydrogen bond distribution in the system and thus resulting in interfacial water with a fluidity intrinsically distinct than that in bulk water.[30,241,255,278,307] Furthermore, highly structured water at the solid-liquid interface[199] might result in an increased friction coefficient.[293,331] Therefore, an altered fluidity of the interfacial[113,113] combined with an increase in the viscosity in bulk may govern hydrodynamics during water capillary filling of nanochannels under external electric fields.

To estimate the mobility of water under these conditions, we measure the self-diffusion coefficient of water along the channel cross section at different electric field strengths (cf. figure 6.9). We calculate the three components of the self-diffusion coefficient in the box *viz.* D_x, D_y and D_z representing x, y, and z components respectively, which are calculated from the asymptotic slope of the time-dependent mean-square displacement (MSD). We consider only the x-component of the self-diffusion coefficient taking into account the direction of the capillary flow. We find that the self-diffusion coefficient of water is affected by the presence of walls and decreases at the wall-fluid interface (cf. figure 6.9). The self-diffusion coefficient of water can be related to the viscosity using Stokes-Einstein relation[340,352] as shown in equation 6.5.

$$\mu_{eff} = \frac{k_B T}{3\pi r_w} \frac{1}{D_{eff}} \tag{6.5}$$

μ_{eff} is the effective viscosity of water, where r_w is the effective molecular diameter which is a function of the size and shape of the molecule (for water molecules, r_w= 0.17 nm[187,215]), and D_{eff} is the self-diffusion coefficient. Moreover, using equation 6.5 and figure 6.9, we infer that the viscosity of water is higher at the wall-water interface compared to the viscosity in the bulk. We observe that the change in interfacial viscosity is less than changes reported in other studies[310] and that the contribution of the interfacial viscosity to the effective viscosity is relatively low and decreases with an increase in electric field strength. Indeed, we calculate the contribution of interfacial viscosity to the total effective viscosity using height dependent viscosity of water in nano-conduits[310] as shown in equation 6.6

$$\frac{\mu_{eff}}{\mu_{bulk}} = 1 + \frac{2L_i}{H}\left(\frac{\mu_{app}}{\mu_{bulk}} - 1\right) \tag{6.6}$$

where μ_{bulk} is the viscosity of the bulk, and μ_{app} is the interfacial viscosity. L_i represents the width of the interface while H is the height of the channel. In this study, we consider interface to be located within 0.6 nm from the channel walls, where maximum water density is found. For the magnitudes of electric field under study, the values of the parameters in equation 6.6 are listed in table 6.1. We noticed that this increase in total effective viscosity due to contribution of the higher interfacial viscosity still cannot explain the lowering of maximum velocity observed during the capillary imbibition under the influence of electric field. All the above results suggest the contribution of an additional interfacial phenomenon that slows down the filling rate of water in the hydrophilic nanochannels.

Influence of electric field on solid-liquid interfacial friction

The increased ordering and lower mobility of water at the interface suggests a higher friction at the walls as compared to systems without external electric fields. To further shed light into this, we calculated the interfacial friction coefficient (λ) near the silica walls in a parallel silica channel with water confined at 300 K. According to linear response theory, λ can be obtained from the equilibrium fluctuations of the friction force, using a Green-Kubo (GK) relation[91,293]

$$\lambda = \lim_{t\to\infty} \lambda_{GK}(t) \tag{6.7}$$

with

$$\lambda_{GK}(t) = \frac{1}{2Ak_BT}\int_0^t \langle F(t')\cdot F(0)\rangle dt' \tag{6.8}$$

where A is the surface area of the wall, T is the temperature, and $F(t)$ is the total tangential force acting along the x-axis at the liquid/solid interface and the factor of 1/2 comes from the averaging over the two spatial dimensions parallel to the sheets. The friction coefficients calculated using GK relation for sufficiently long time plateaus to a constant value of λ_{GK}. We obtain the value of λ_{GK} from the plateau of the integrated force autocorrelation function in the range of 0–0.15 ps. We take this plateau value as the equilibrium value for the friction coefficient following the methodology presented by Falk et al.[90]. We plot these calculated values of the friction coefficients for three different cases in figure 6.10. We observe a significant increase in the calculated values of friction coefficients with increase

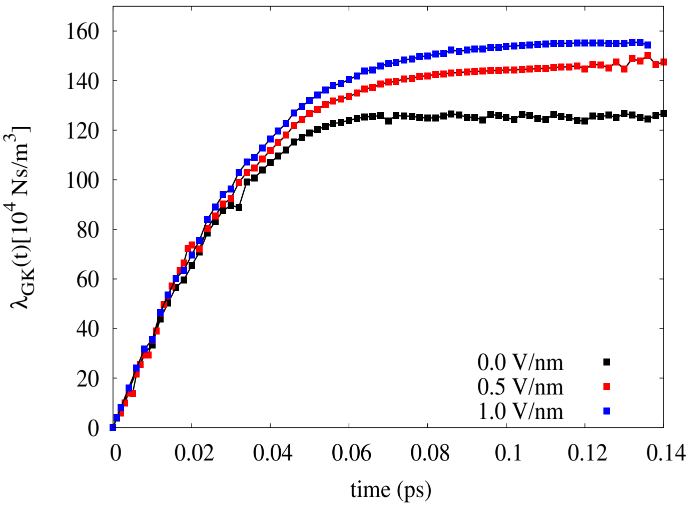

FIGURE 6.10: Interfacial friction coefficient in water-silica interface under different external electric fields. Source: Own elaboration

in electric field in the direction parallel to the silica surface. For the case with applied electric field of 1.0 V/nm, we find approximately ca. 33 % increase in λ_{GK}, compared to the case with no applied field.

6.5 Conclusions

In summary, we have presented a study on the effect of externally applied electric fields on capillary flow of water in amorphous silica nanochannels. We compute lower equilibrium DCAs of the capillary meniscus as electric fields with increasing strengths are applied. Furthermore, we find that the overall filling rates decrease with increasing electric field strengths. We attribute this to an increase in effective viscosity due to the alignment of water molecules in the bulk and also to the particular structure of the interfacial water molecules under combined effect of the silica wall surface and the presence of the external electric field. Our results indicate that the ordering induced by the electric field results in an increased solid-liquid friction which combined to a substantial increase in bulk viscosity dominate the capillary force balance during water imbibition. In particular, our study suggests that the ordering of water molecules affects the "propagation" of momentum dissipation between the solid surface and liquid water such that the friction is readily transferred to the bulk in highly oriented water molecules. This finding from our atomistic simulations enriches the general discussions of the solid-liquid interface related phenomena and its critical effect in transport of fluid in hydrophilic nanochannels. Moreover, our results are helpful for a comprehensive understanding of the complex phenomenon of water capillary filling of nanopores under the effect of externally applied electric fields.

Chapter 7

Concluding remarks and scope of future work

7.1 Summary of the major findings

In this study, through an atomistic description of matter, we attempt to provide a better understanding of the flow during nanocapillary imbibition using MD simulations. The outcomes of the present dissertation can be classified into three broad categories:

1) In chapter 4, we demonstrate the height dependence of the filling velocity in the amorphous silica nanoslit channels. The observed lower than theoretically predicted velocity can be amended by the inclusion of two element in Bosanquet's equation of capillarity: i) The initial contact angle at the channel entrance that depends on the height and material of the channel. ii) Dynamic contact angle remains constant during the inertial regime and converges to an equilibrium value during viscous regime. Moreover we find that the initial contact angle is different than the intuitive result of 90°. We also demonstrate that the inertial time regime is more significant for channels with greater height within the channel heights studied here.

2) In chapter 5, we study the effect of hydration of ions in capillary imbibition inside silica nanoslit channels at point of zero charge (PZC), where the net surface charge on the channel walls is zero. We find that the observed filling rate follows the modified version of Bosanquet's equation of capillarity. This indicates that the filling kinetics in all the cases are altered by hydrodynamic forces enhanced by viscoelectric effect due to the presence of ions in the electrolyte solution. We observe that the presence of cations do not significantly affect the surface tension while the viscosity depends both, on the type (structure maker or breaker) and concentration of the cations in the electrolyte solution.

3) In chapter 6, we provide evidence that nanocapillary imbibition control is feasible by an adequate application of electric field across the channel. The application of an external electric field increases the viscosity of water and also decreases the equilibrium contact angle with the silica surface. Nevertheless, it lowers the filling rate of water inside the nanochannels which can be attributed to the reduced fluidity owing to complex interplay of enhanced viscosity, due to higher orientation of water molecules under the influence of the electric field and increase in solid-liquid friction at the interface.

7.2 Hypothesis validation

Taking into account the results obtained through our study on the nanocapillary imbibition of water and aqueous electrolyte solutions in hydrophilic silica nanochannels, we validate the proposed hypotheses.

1) The higher velocity predicted by Bosanquet's equation of capillarity is due to the assumption that the equilibrium contact angle is established right at the channel entrance, which is in contrast with our study of nanocapillary imbibition of water inside hydrophilic silica nanochannel. We showed that the initial Bosanquet's velocity depends upon the contact angle made by the water miniscus at the channel entrance and hence, the modification of of Bosanquet's force balance equation by the inclusion of dynamic contact angle explains the lower than expected velocity at the channel entrance.

2) The hydration of ions in water increases the viscosity due to electroviscous effects while other properties like surface tension is only slightly affected. We show that filling velocity is decreased due to the increase in viscous forces. Hence, the hydration related to the presence of ions in water affects the filling kinetics in hydrophilic nanochannels.

3) Our results indicate that the application of external electric field modifies the dynamic properties like viscosity and self diffusion which can be attributed to the reorientation of water molecules under the influence of external field. We show that the filling kinetics depends upon the increased solid-liquid friction along with enhanced dynamic properties of water which validates that an external electric field affects the filling kinetics of water in hydrophilic nanochannels.

7.3 Scope of future work

The results obtained in this thesis leads to interesting theoretical bases upon the application of nanocapillary imbibition in real life nanodevices. Hence, to continue with our investigation, we look forward to incorporate polarizable force fields and more detailed dipole models to reproduce more realistic results using different class of ions. Furthermore, we shall attempt to set theoretical background to include the transport and separation of biomolecules like DNA and RNA in ionic environment using nanocapillary imbibition.

Appendix A

Supporting Information for Chapter 4.

A.1 Interaction potentials used in the study

Silica-Silica interaction Potential

The silica-silica interaction potential is approximated by TTAMm model[114] which is a modification of classical two-body potential (TTAM),[297] that describe silica-silica, silica-oxygen and oxygen-oxygen interaction through Coulombic potential for electrostatic interactions, Buckingham and a Lennard-Jones 18-6 potential, which avoids the blowing up of atoms in the silica slab at high temperatures, for short range interactions (ca. A.1). This model has been successfully used to describe amorphized hydrophilic silica in recent studies.[64,159,223,343] The parameters of the potential for all the interactions are presented in table B.2. The partial charge of silica and water are 2.4e and -1.2e respectively.

$$U_{ij} = \frac{q_a q_b}{4\pi\epsilon_0 r_{ij}} + 4\epsilon_{ab}\left[\left(\frac{\sigma_{ab}}{r_{ij}}\right)^{18} - \left(\frac{\sigma_{ab}}{r_{ij}}\right)^{6}\right] - \alpha_{ab}\exp(-\rho_{ab} r_{ij}) - \frac{C_{ab}}{r_{ij}} \tag{A.1}$$

where ϵ is the depth of the potential well, σ is the finite distance at which the inter-particle potential is zero and r is the distance between the particles.

Silica-Water interaction parameters

Water-Silica interaction potential (ca. equation A.2) parametrized by Zambrano el al.[343] that adequately models water-silica interaction will be used for this study. The authors parametrized Buckingham type potential to reproduce the macroscopic water contact angle (WCA) of 19.9 folowing the methodology proposed by Werder et al.[324]. The electrostatic calculations are calculated by a Coulomb potential and the partial charges considered are 1.3e and 0.65e for silica and oxygen atoms respectivley. The interaction potential are presented in table A.2.

$$U_r = \alpha_{ab}\exp(\rho_{ab} r_{ij}) - \frac{C_{ab}}{r_{ij}} \tag{A.2}$$

TABLE A.1: Silica-silica interaction parameters.

$a-b$	$\epsilon_{ab}(kJ/mol)$	$\sigma_{ab}(nm)$	$\alpha_{ab}(kJ/mol)$	$\rho_{ab} nm^{-1}$	$C_{ab}(kJnm^6$ /mol)
Si-Si	1276.8	0.04	8.312865 x 10^{10}	152.207	0.0022841
O-O	0.04613	0.22	169551.09	28.2641	0.020719
Si-O	1.0834	0.13	1034699.4	47.959593	0.0068258

Source: Own elaboration.

TABLE A.2: Silica-water interaction parameters.

$a - b$	$\alpha_{ab}(kJ/mol)$	$\rho_{ab} nm^{-1}$	$C_{ab}(kJnm^6$ /mol)
Ow-Ow	1.013 x 10^5	25.00	2.360 x 10^2
Hw-Hw	6.83 x 10^3	32.66	0.0

Own elaboration.

A.2 Measurement of surface tension of fluids

One of the most important properties of a fluid and the cause of capillary force that drives the fluid into the capillary channels is surface tension. Hence, it becomes relevant to study the effect of electrolyte solutions on surface tension of water to predict its role in nanocapillary imbibition of these solutions. Surface tension of pure water has been studied in various previous studies and authors have sucessfully predicted surface tensions for different models of water molecules[4,7,203,306]. In our simulations, we consider a system containing 3000 water molecules enclosed in a cubic box of size 4 nm x 4 nm x 4 nm. First of all the water molecules are equilibrated in NPT ensemble for 2 ns and the output is further subjeted to NVT ensemble for 2 ns. Subsequently, we increase the size of box in z-direction to three times its initial value i.e. 12 nm, center the water molecules in the box and perform production simulations under NVT ensemble for 3 ns in the orthorombic simulation box of 4 nm x 4 nm x 12 nm (cf. figure A.1). This configuration allows to create two independent surfaces on the two ends of z-axis. We use simulation package GROMACS 5.2[128] to perform molecular dynamics studies and generate the molecular trajectories using time step of 1 fs. During the equilibration phase the temperature is kept constant by Berendsen thermostat[25] and during the production stage, it is controlled by Nose-Hoover thermostat.[133,218] To give consistency to our study, we use SPC/E[24] water molecules and the intramolecular bonds and angles are kept rigid using constraints.[10,257] The Lennard-Jones potential was truncated at 1.3 nm and electrostatic interactions are dealt with Ewald sums. The Fourier part of Ewald sum are evaluated using Smooth-Particle-Mesh-Ewald (SPME)[88] method and width of the mesh is set to 1Å and a fourth order interpolation is used. The pressure tensor is readily calculated in the version of simulation software used for this study, and hence allows us to calculate the surface tension (γ). In case of systems with planar interface perpendicular to the z-axis, γ is given by the following relation[256]:

$$\gamma = \int_{-\infty}^{\infty} dz[P_N(z) - P_T(z)] \tag{A.3}$$

where $P_N(z)$ and $P_T(z)$ are the (local) normal and tangential components of the pressure tensor at position z, respectively. For a planar interface, p_N does not depend on z and is equal to the vapor pressure, p. In the present study, we use the following expression to calculate the surface tension, following the methodology proposed by Spoel et al.[302]

$$\gamma = \frac{1}{n}\int_0^{L_z}\left[P_{zz}(z,t) - \frac{P_{xx}(z,t) + P_{yy}(z,t)}{2}dz\right] \tag{A.4}$$

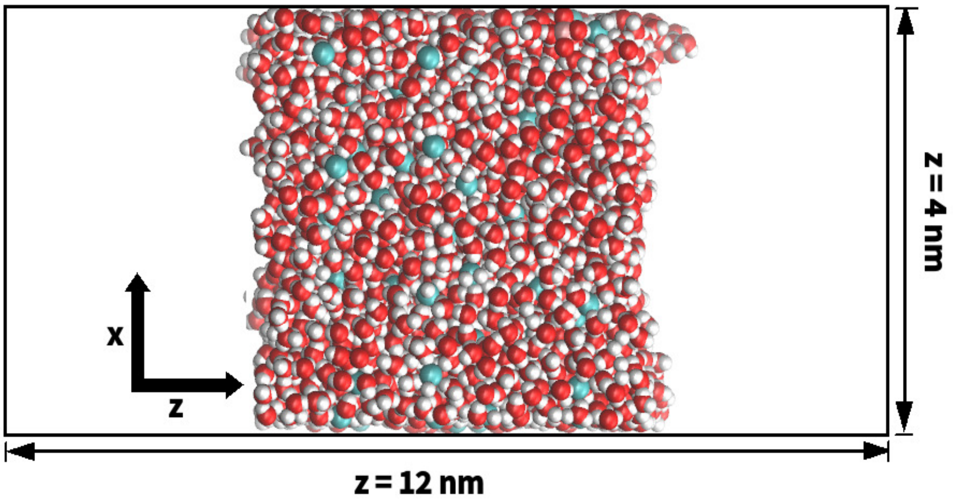

FIGURE A.1: A snapshot of the slab of the system used to calculate the surface tension of the electrolyte solutions. Source: Own elaboration.

which leads to,

$$\gamma = \frac{L_z}{n}\left[P_{zz}(t) - \frac{P_{xx}(t) + P_{yy}(t)}{2}\right] \tag{A.5}$$

where, L_z is the height of the box and n is the number of surfaces.

Energy analysis of surface tension

The creation of a surface generates additional enthalpy in the system. We measure this additional enthalpy, denoted by excessive surface enthalpy, as the difference of enthalpies between solutions with and without surfaces

$$H = H_s - H_0 \tag{A.6}$$

where, ΔH_s and ΔH_0 are the total enthalpy of simulated systems with surfaces and without surfaces respectively. There is no variation of volume at equilibrium, hence the difference $p\Delta V$ can be ignored and H can be presented as:

$$H = E_s - E_0 \tag{A.7}$$

where, E_s and ΔE_0 are the total potential energy of simulated systems with surfaces and without surfaces respectively. The surface tension can be related to the excessive surface energy per unit area using equation A.8

$$\sigma = \frac{\Delta G}{A} = \frac{\Delta H - T\Delta S}{A_t} \tag{A.8}$$

where, ΔG is the increased part of free energy due to the creation of surfaces, ΔS is the excessive surface entropy. Hence, the change in entropy of the system, which is due to the change in surface entropy can be calculated with equation A.8. We can calculate the contribution of the total entropic and enthalpic part to the surface tension making a comparison of the factors $\Delta H/A$ and $T\Delta S/A$.

Appendix B

Supporting Information for Chapter 5.

B.1 S1. Types and concentration of ions used to study the nanocapillary imbibition in hydrophilic silica nanochannel

TABLE B.1: Salts and their concentrations used to study the nanocapillary imbibition in hydrophilic silica nanochannel.

Salts		Concentration			
LiCl	0.2	0.4	0.6	0.8	1.0
NaCl	0.2	0.4	0.6	0.8	1.0
KCl	0.2	0.4	0.6	0.8	1.0
$MgCl_2$	0.2	0.4	0.6	0.8	1.0
$CaCl_2$	0.2	0.4	0.6	0.8	1.0
$BaCl_2$	0.2	0.4	0.6	0.8	1.0
$AlCl_3$	0.2	0.4	0.6	0.8	1.0

Source: Own elaboration

B.2 S2. Silica interaction parameters used for the amorphization of silica slabs

TABLE B.2: Silica-silica interaction parameters.

$a-b$	ϵ_{ab}(kJ/mol)	σ_{ab} (nm)	α_{ab} (kJ/mol)	ρ_{ab} nm^{-1}	C_{ab}(kJnm^6 /mol)
Si-Si	1276.8	0.04	8.312865 x 10^{10}	152.207	0.0022841
O-O	0.04613	0.22	169551.09	28.2641	0.020719
Si-O	1.0834	0.13	1034699.4	47.959593	0.0068258

Source: Own elaboration

B.3 Lorentz-Berthelot mixing rule

For a simple pair potential such as Lennard-Jones (LJ) interaction,

$$U_{ij}(r) = 4\epsilon_{ij}\left[\left(\frac{\sigma_{ij}}{r}\right)^{12} - \left(\frac{\sigma_{ij}}{r}\right)^{6}\right] \tag{B.1}$$

TABLE B.3: Interaction parameters for the electrolytes used in the study.

$a - b$	σ_{ab} (nm)	ϵ_{ab}(kJ/mol)	Reference
Li-Li	0.2343	0.0249	Pethes[230]
Li-Cl	0.3097	0.2353	Pethes[230]
Li-O	0.23300	0.6694	Pethes[230]
Li-Si	0.26505	0.60710	Pethes[230]
Na-Na	0.258	0.0617	Bonthius[34]
Cl-Cl	0.4401	0.4184	Aluru et al.[154]
Cl-O	0.3785	0.5216	Aluru et al.[154]
Cl-Si	0.3895	1.0118	Aluru et al.[154]
Na-O	0.2875	0.2003	Aluru et al.[154]
Na-Si	0.38861	0.2983	Zambrano et al.[342]
K-K	0.3334	0.4184	Aluru et al.[154]
K-Cl	0.3866	0.4184	Aluru et al.[154]
K-O	0.325	0.5216	Koheshan et al.[167]
K-Si	0.3359	1.0118	Aluru et al.[154]
Mg-Mg	0.1398	3.6610	Gavryushov[106]
Mg-Cl	0.2900	1.2376	Prakash et al.[239]
Mg-O	0.2282	1.5428	Prakash et al.[239]
Ca-Ca	0.2361	1.8810	Gavryushov[106]
Ca-Cl	0.3381	0.8871	Prakash et al.[239]
Ca-O	0.2764	1.1059	Prakash et al.[239]
Ba-Ba	0.3790	0.1970	Zhu et al.[351]
Ba-Cl	0.4096	0.2871	Zhu et al.[351]
Al-Al	0.14472	0.9054	Faro et al.[92]
Cl_{Li}-Cl_{Li}	0.3852	2.2240	Pethes[230]

Source: Own elaboration

between molecules of species i and j, the interaction is specified by two parameters, an energy and the molecular size parameter, ϵ_{ij} and σ_{ij}, respectively. For two particles $i = j$, these parameters may be determined from properties such as critical temperature and volume. However, the cross or unlike interactions, $i \neq j$, between unlike pairs of molecules are not so easily obtained. For this reason, mixing rules are convenient. The most well-known mixing rules are Lorentz-Berthelot(LB) mixing rules, where the cross terms are given by,

$$\epsilon_{ij} = \sqrt{\epsilon_{ii}\epsilon_{jj}} \tag{B.2}$$

and

$$\sigma_{ij} = \frac{\sigma_{ii} + \sigma_{jj}}{2} \tag{B.3}$$

That is ϵ_{ij} and σ_{ij} are given by geometric and arithmetic averages.

B.4 Filling kinetics of water-electrolyte systems in hydrophilic silica nanochannel

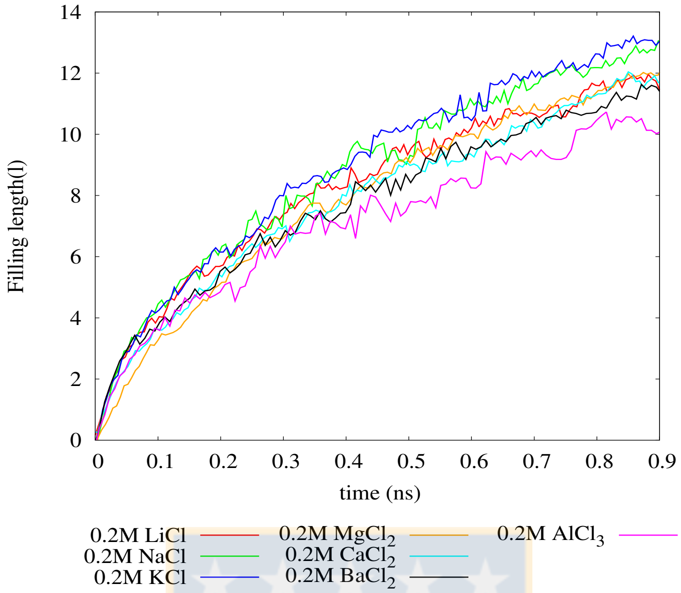

FIGURE B.1: Filling kinetics of 0.2M electrolyte system in silica-nanochannel. Source: Own elaboration.

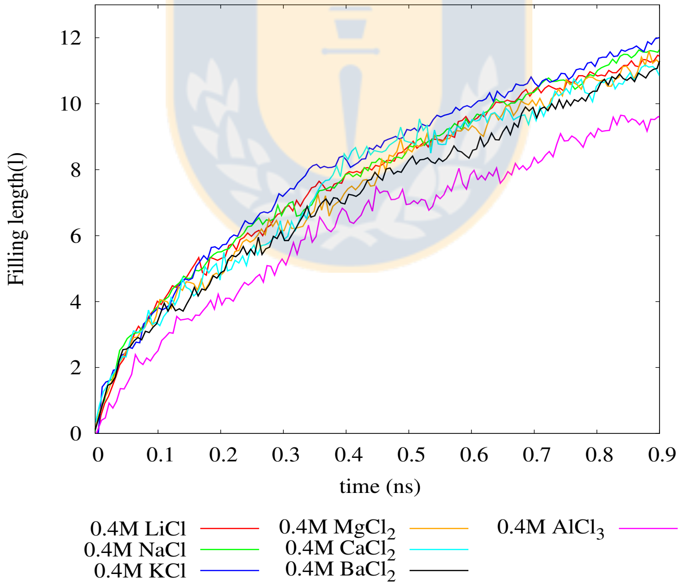

FIGURE B.2: Filling kinetics of 0.4M electrolyte system in silica-nanochannel. Source: Own elaboration.

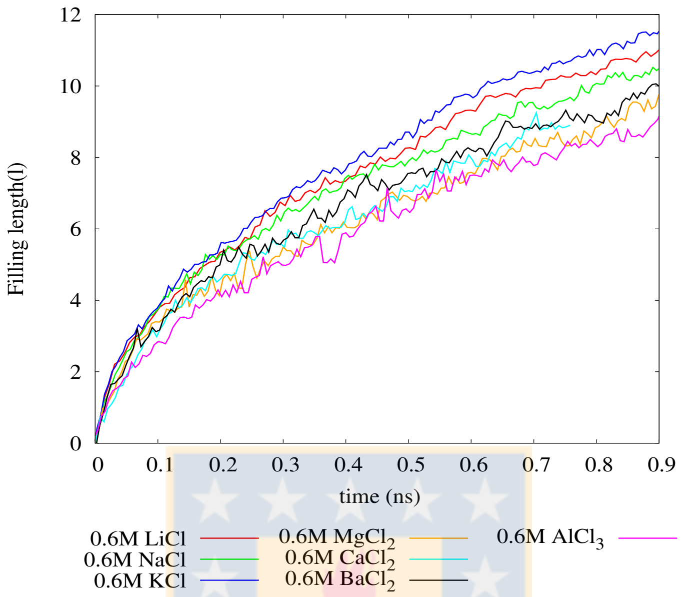

FIGURE B.3: Filling kinetics of 0.6M electrolyte system in silica-nanochannel. Source: Own elaboration.

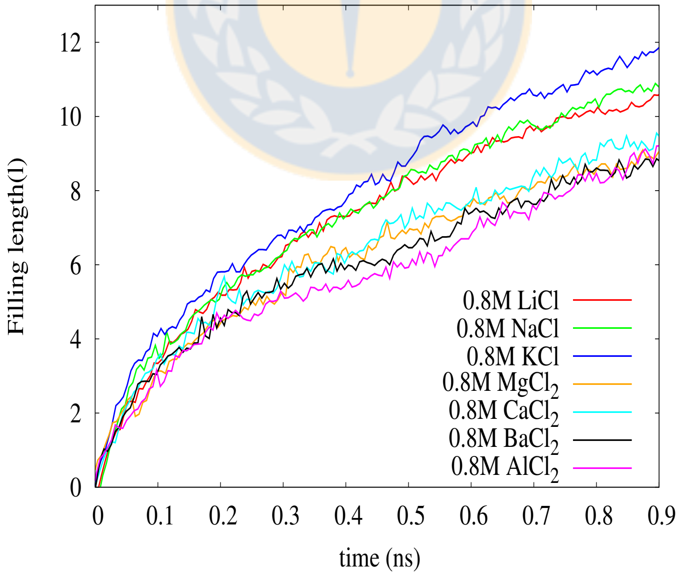

FIGURE B.4: Filling kinetics of 0.8M electrolyte system in silica-nanochannel. Source: Own elaboration.

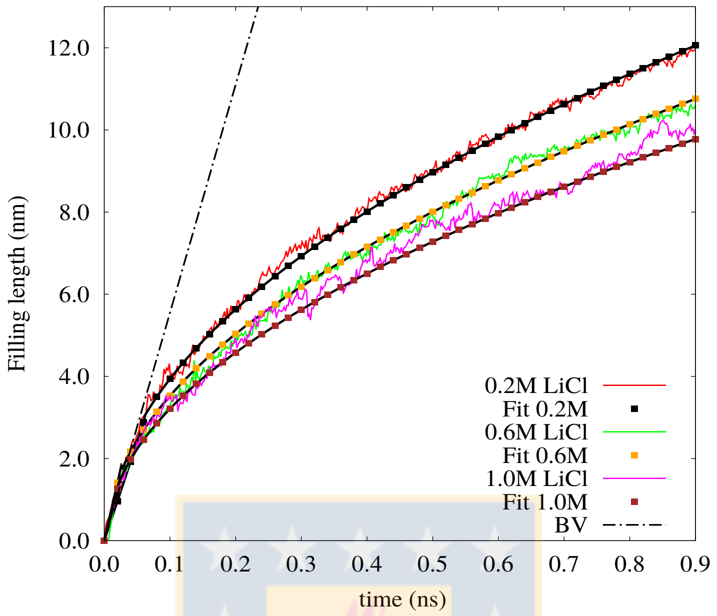

FIGURE B.5: Filling kinetics of LiCl solution in silica-nanochannel. The solid lines are fit of Bosanquet's equation, while the straight dotted line is the fit of initial velocity. Source: Own elaboration.

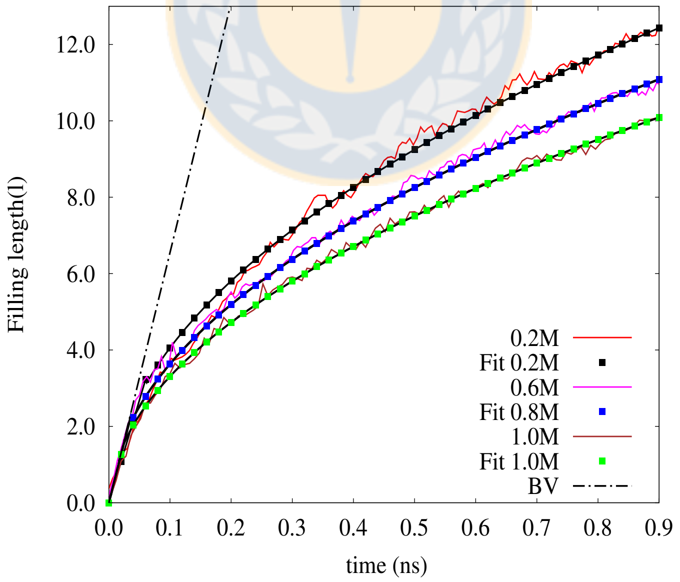

FIGURE B.6: Filling kinetics of NaCl solution in silica-nanochannel. The solid lines are fit of Bosanquet's equation, while the straight dotted line is the fit of initial velocity. Source: Own elaboration.

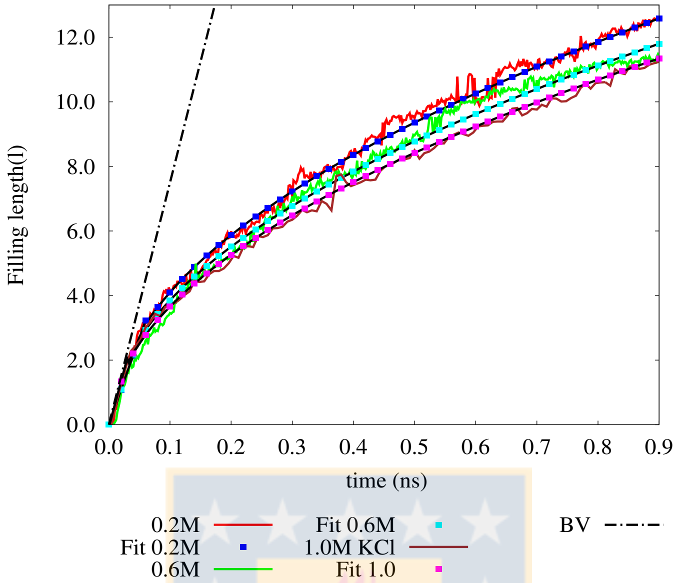

FIGURE B.7: Filling kinetics of KCl solution in silica-nanochannel. The solid lines are fit of Bosanquet's equation, while the straight dotted line is the fit of initial velocity. Source: Own elaboration.

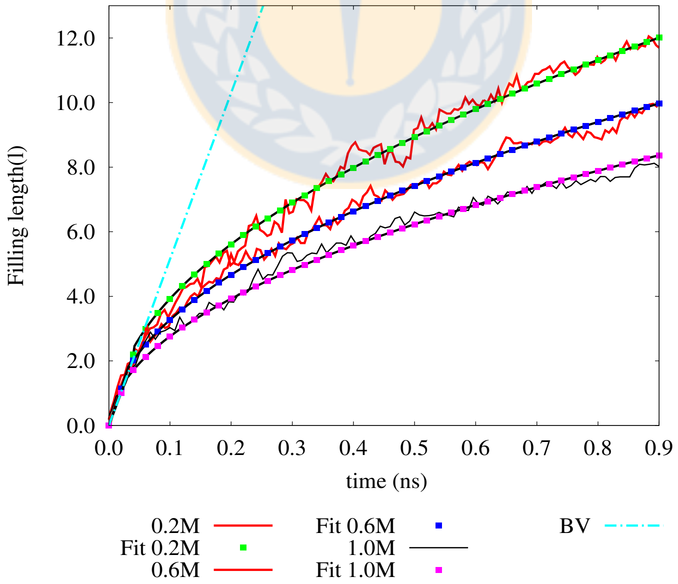

FIGURE B.8: Filling kinetics of $MgCl_2$ solution in silica-nanochannel. The solid lines are fit of Bosanquet's equation, while the straight dotted line is the fit of initial velocity. Source: Own elaboration.

B.5 Radial distribution functions of water-electrolyte systems

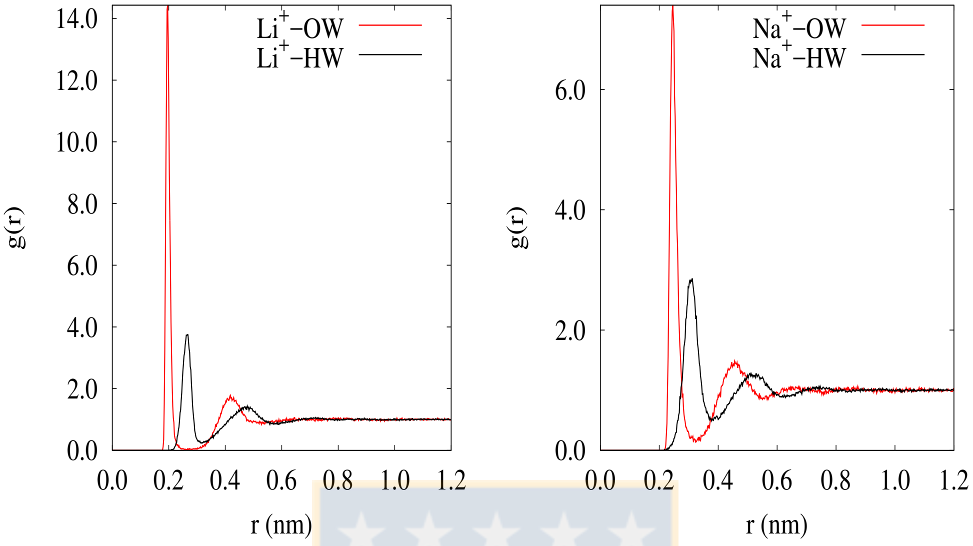

FIGURE B.9: Radial distribution functions of Li$^+$-OW (left) and Na$^+$-OW (right). Source: Own elaboration.

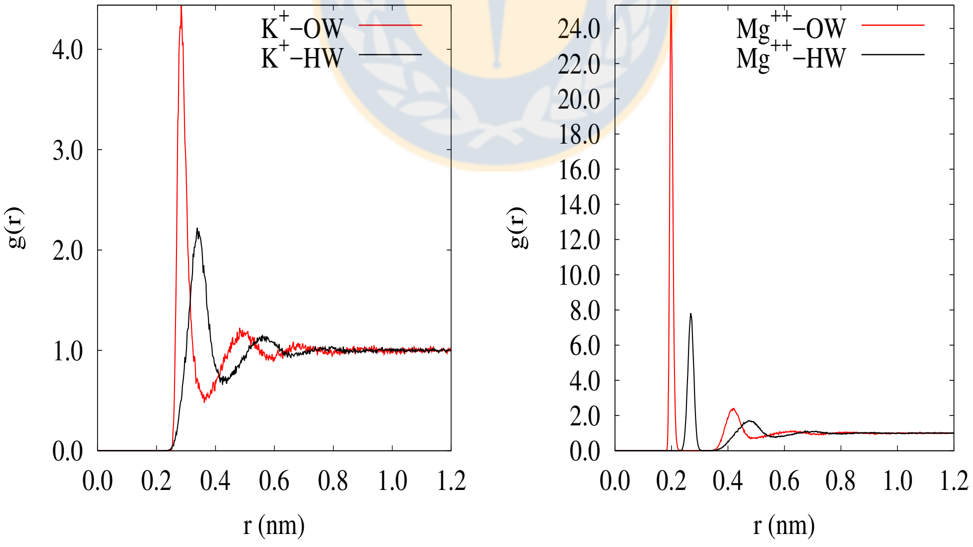

FIGURE B.10: Radial distribution functions of K$^+$-OW (left) and Mg^{2+}-OW (right). Source: Own elaboration.

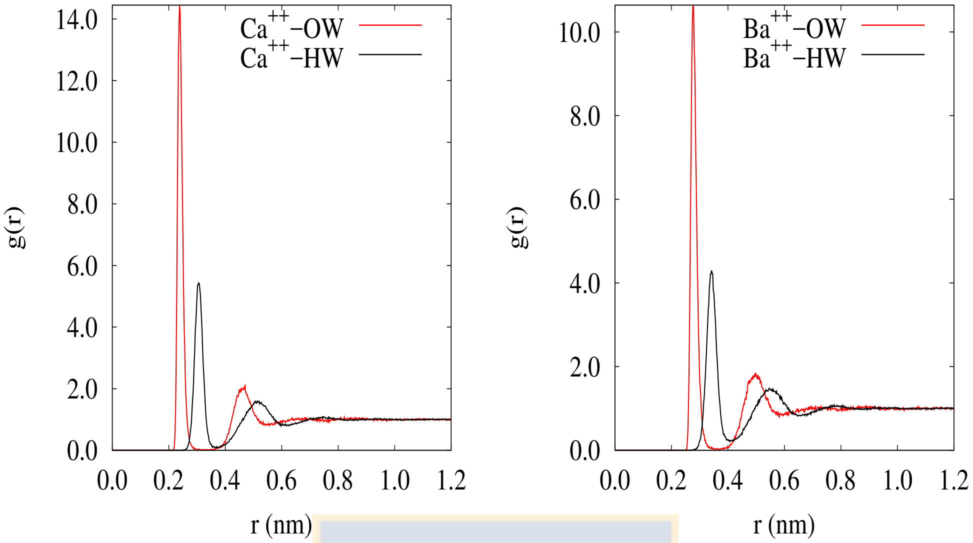

FIGURE B.11: Radial distribution functions of Ca^{2+}-OW (left) and Ba^{2+}-OW (right). Source: Own elaboration.

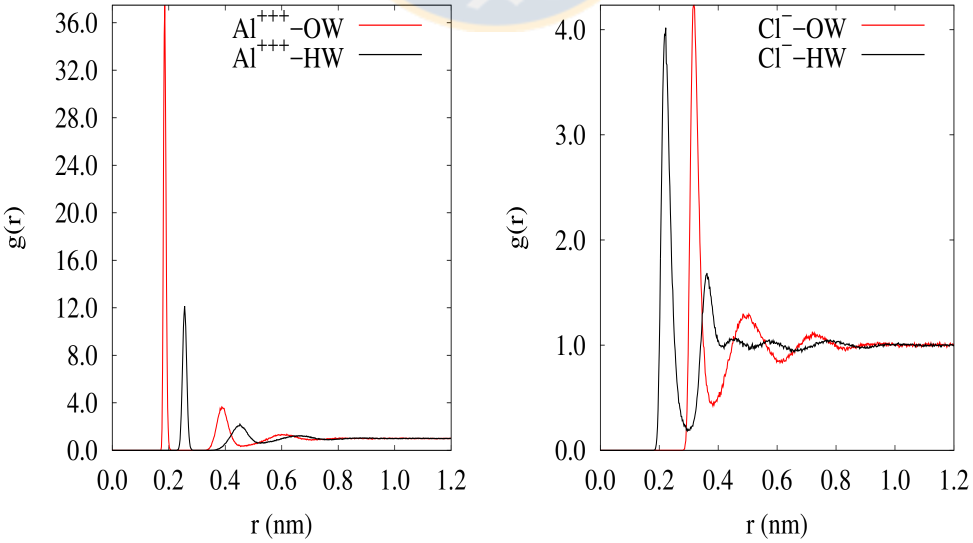

FIGURE B.12: Radial distribution functions of Al^{3+}-OW (left) and Cl^{-}-OW (right). Source: Own elaboration.

TABLE B.4: Comparison of characteristic peak values and positions of the ions in water at 300 K. Source: Own elaboration.

		$g_{OW}(rmax)$	r_{max}(nm)	$g_{OW}(rmin)$	r_{min}(nm)	N_c
Li^+	MD (present work)	14.4	0.196	0.0	0.26	4.32
	MD[178]	9.56	0.22	0.03	0.31	6.00
	MD[350]	13.76	0.197	0.00	0.256	4.40
	Experimental[201]	-	0.194	-		4.10
Na^+	MD (present work)	7.39	0.245	0.14	0.32	5.33
	MD[178]	7.00	0.245	0.22	0.350	6.60
	MD[350]	8.11	0.237	0.08	0.306	5.20
	Experimental[201]	-	0.234	-	-	5.30
K^+	MD (present work)	4.43	0.2827	0.50	0.36	6.42
	MD[178]	5.64	0.270	0.35	0.365	8.00
	MD[350]	4.02	0.286	0.45	0.369	6.10
	Experimental[201]	-	0.265	-	-	6.00
Mg^+	MD (present work)	25.32	0.2	0.0	0.3	6.03
	MD[219]	17.2	0.22	0.0	0.31	6.2
	MD[42]	0.4	0.21	-	-	6.0
	Experimental[201]	-	0.209	-	-	6.0
Ca^+	MD (present work)	14.43	0.24	0.0	0.3	7.47
	MD[143]	-	0.25	-	-	7.6
	MD[74]	-	0.237	-	-	7.1
	Experimental[201]	-	0.240	-	-	7.0
Ba^+	MD (present work)	10.62	0.28	0.0	0.35	8.3
	MD[275]	-	0.28	-	-	8.3
	Experimental[201]	-	0.281	-	-	8.1
Al^+	MD (present work)	37.14	0.19	0.0	0.2	5.88
	MD[207]	40.99	0.18	0.0	0.20	6.0
	Experimental[201]	-	0.191	-	-	6.0
Cl^-	MD (present work)	4.23	0.32	0.43	0.38	6.81
	MD[350]	3.96	0.33	0.55	0.375	6.40
	MD[117]	3.9	0.3275	-	-	8.4
	Experimental[201]	-	0.316	-	-	7.0

Source: Own elaboration

B.6 Orientation distribution functions of water around ions in their respective solutions

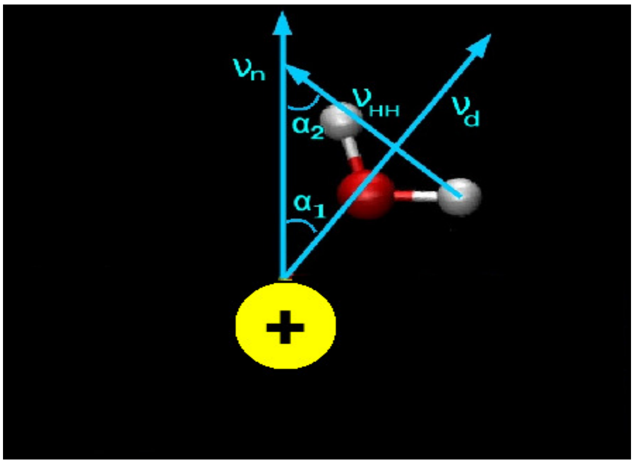

FIGURE B.13: The angles considered to determine the orientation of the water molecules around specific ions.
Source: Own elaboration.

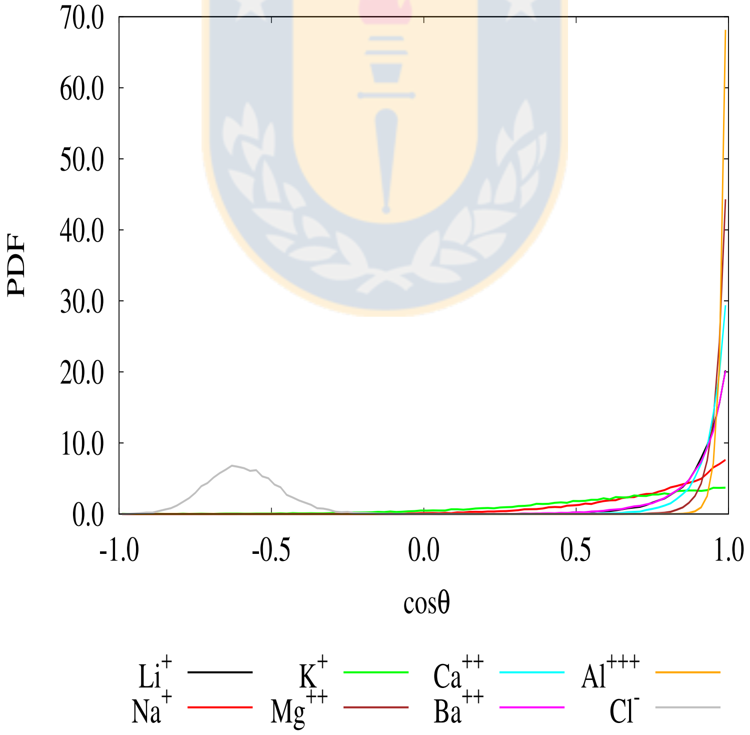

FIGURE B.14: Probability distribution function of water dipoles around the ions used in this study. Source: Own elaboration.

TABLE B.5: Total interaction energy (kJ/mol) between ion- water pair in the first solvation shell at 300 K. Source: Own elaboration.

Li^+	Na^+	K^+	Mg^{++}	Ca^{++}	Ba^{++}	Al^{+++}	Cl^-
274.8	167.933	110.88	519.23	327.885	214.25	849.62	298.31

Source: Own elaboration

TABLE B.6: Distance (nm) between the hydrogen atoms of the first shell and the adjacent oxygen molecules in the bulk at 300 K. Source: Own elaboration.

Li^+	Na^+	K^+	Mg^{++}	Ca^{++}	Ba^{++}	Al^{+++}
0.152	0.146	0.144	0.147	0.1666	0.1525	0.131

Source: Own elaboration

B.7 Viscosity of electrolyte solutions at different concentrations

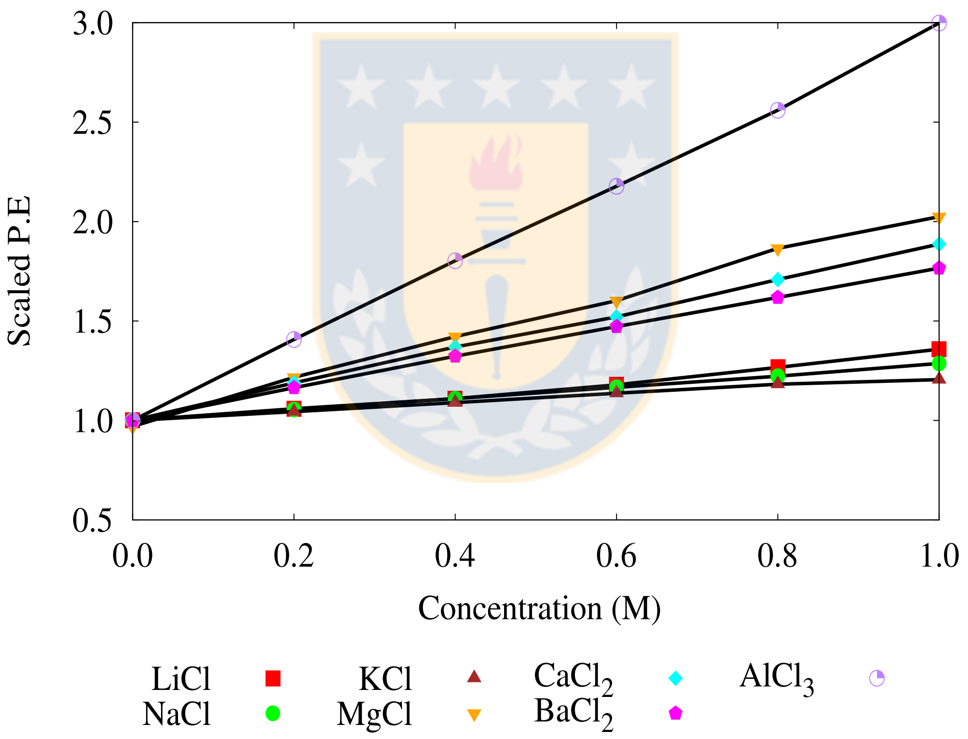

FIGURE B.15: Potential energy between ion-water for different concentrations for the electrolyte solutions under study. Source: Own elaboration.

TABLE B.7: Viscosity of various electrolyte solutions at different concentrations at 300K

Salt	Concentration (M)	Viscosity (mPa.s)[This study]	viscosity experimental
H_2O	pure	0.726	0.729
$LiCl$	0.2	0.84	0.91
$LiCl$	0.4	0.88	-
$LiCl$	0.6	0.95	0.96
$LiCl$	0.8	0.966	–
$LiCl$	1.0	0.99	1.05
$NaCl$	0.2	0.73	–
$NaCl$	0.4	0.78	–
$NaCl$	0.6	0.91	0.928 (conc=0.5)
$NaCl$	0.8	0.93	-
$NaCl$	1.0	0.96	0.972 (conc=1.0)
KCl	0.2	0.69	–
KCl	0.4	0.74	–
KCl	0.6	0.77	0.806 (conc=0.5)
KCl	0.8	0.79	–
KCl	1.0	0.803	0.972 0.813 (c0nc=1.0)
$MgCl_2$	0.2	0.79	1.12 (conc=0.28)
$MgCl_2$	0.4	0.86	–
$MgCl_2$	0.6	1.20	1.285(conc=0.65)
$MgCl$	0.8	1.29	–
$MgCl_2$	1.0	1.408	1.4180(conc=0.90)
$CaCl_2$	0.2	0.80	0.92 (conc = 0.2)
$CaCl_2$	0.4	0.87	–
$CaCl_2$	0.6	1.09	1.07 (conc = 0.65)
$CaCl_2$	0.8	1.14	1.07 (conc = 0.65)
$CaCl_2$	1.0	1.21	1.17 (conc = 0.97)
$BaCl_2$	0.2	0.78	1.06 (conc=0.25)
$BaCl_2$	0.4	0.877	–
$BaCl_2$	0.6	1.09	1.12 (conc=0.499)
$BaCl_2$	0.8	1.16	–
$BaCl_2$	1.0	1.25	1.27 (conc=0.999)
$AlCl_3$	0.2	0.843	–
$AlCl_3$	0.4	0.9644	–
$AlCl_3$	0.6	1.210	1.27
$AlCl_3$	0.8	1.35	–
$AlCl_3$	1.0	1.862	1.83

Source: Own elaboration

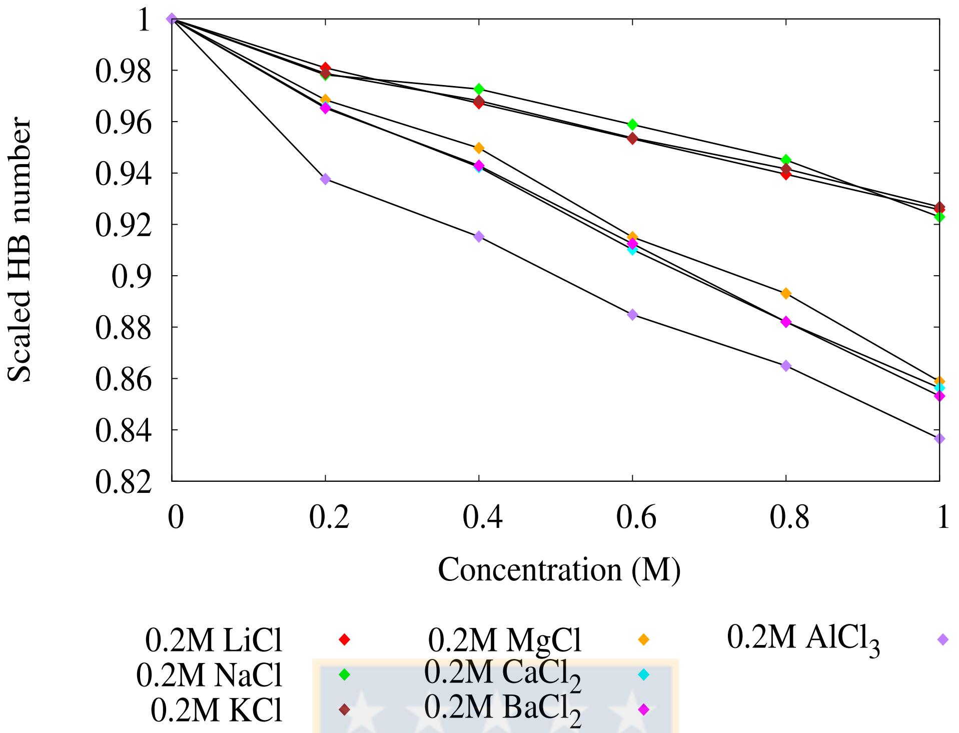

FIGURE B.16: Number of hydrogen bonds in electrolytic solutions in relation to the concentration. Source: Own elaboration.

B.8 Surface tension of electrolyte-ion systems at different concentrations

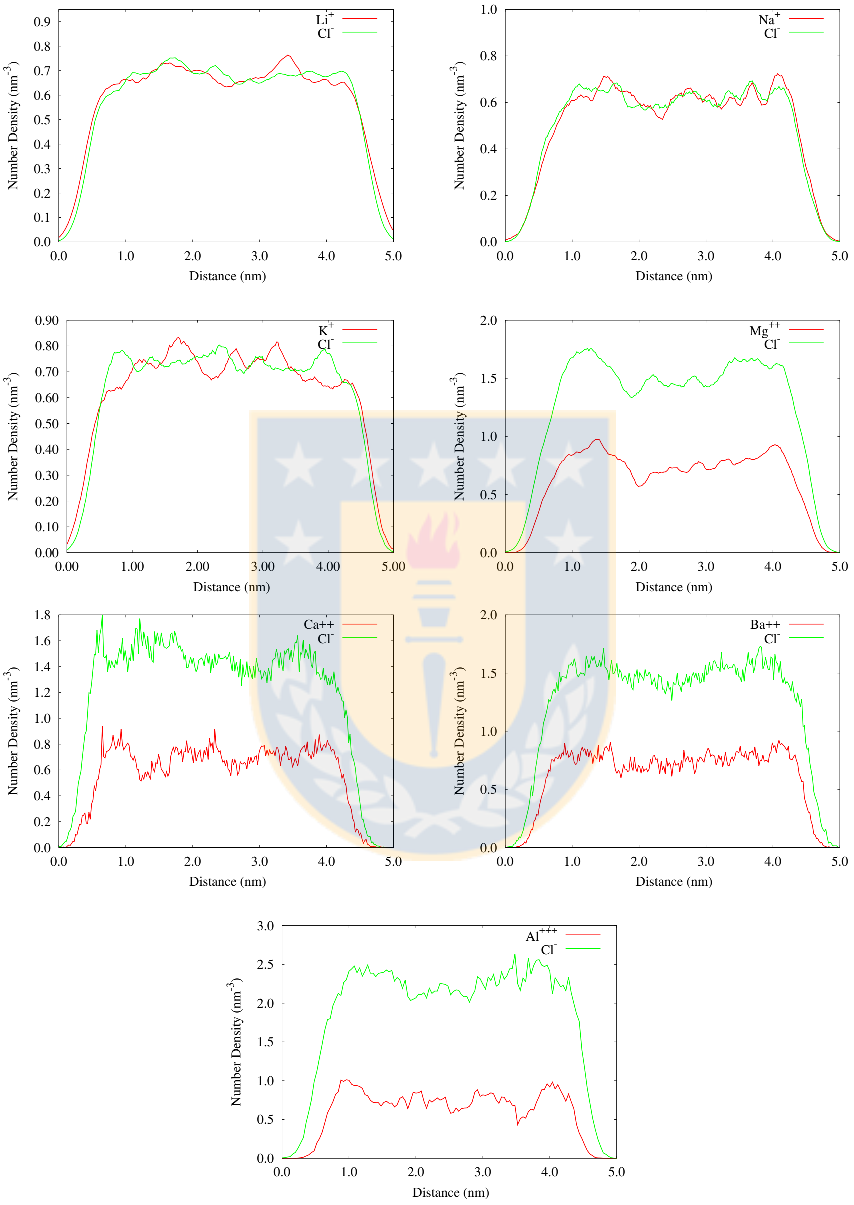

FIGURE B.17: Densities of the anions and cations of the systems under study along the direction perpendicular to film. Source: Own elaboration.

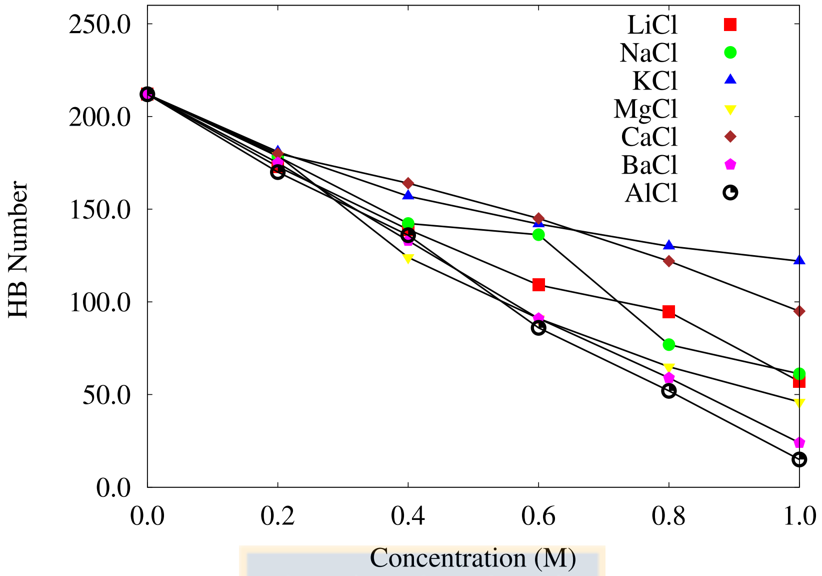

FIGURE B.18: Number of interfacial hydrogen bonds in electrolytic solutions in relation to the concentration. Source: Own elaboration.

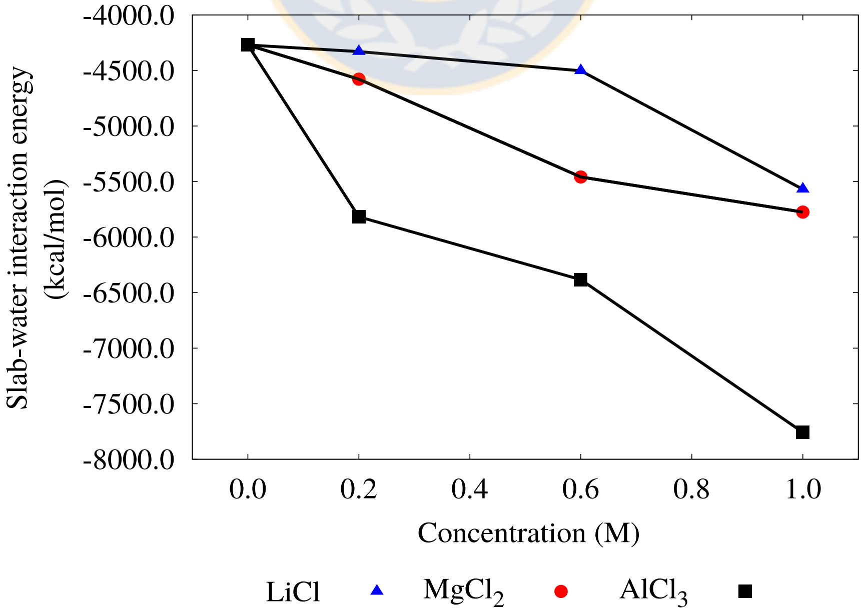

FIGURE B.19: Interaction energy of the electrolyte solutions with the hydrophilic silica slab in relation to the concentration on a hydrophilic silica slab. Source: Own elaboration.

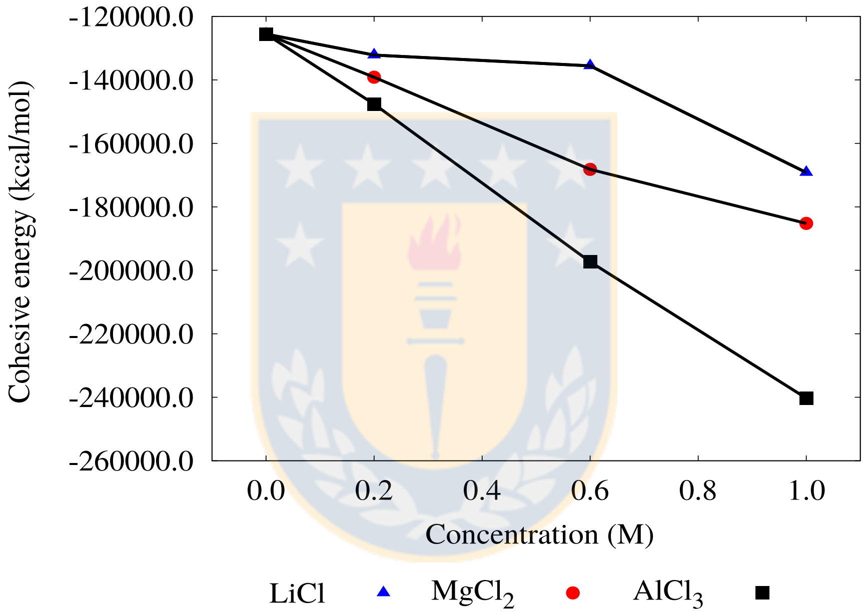

FIGURE B.20: Cohesive potential energy of the electrolyte solutions in relation to the concentration on a hydrophilic silica slab. Source: Own elaboration.

Appendix C

Supporting Information for Chapter 6.

C.1 S1. Average velocity during the viscous regime during nanocapillary imbibition in amorphous silica channels

The maximum velocity during the viscous regime of the nanocapillary imbibition is calculated from the slope of the length vs time plot, and is shown in fig B.2. The maximum velocities are calculated as an average velocites observed between 4-8 nm from the channel distance, which guarantees that the inertial effects are negligible. We observe a monotonic decrease in the maximum velocity of the meniscus with increase in the field strength of the applied electric field.

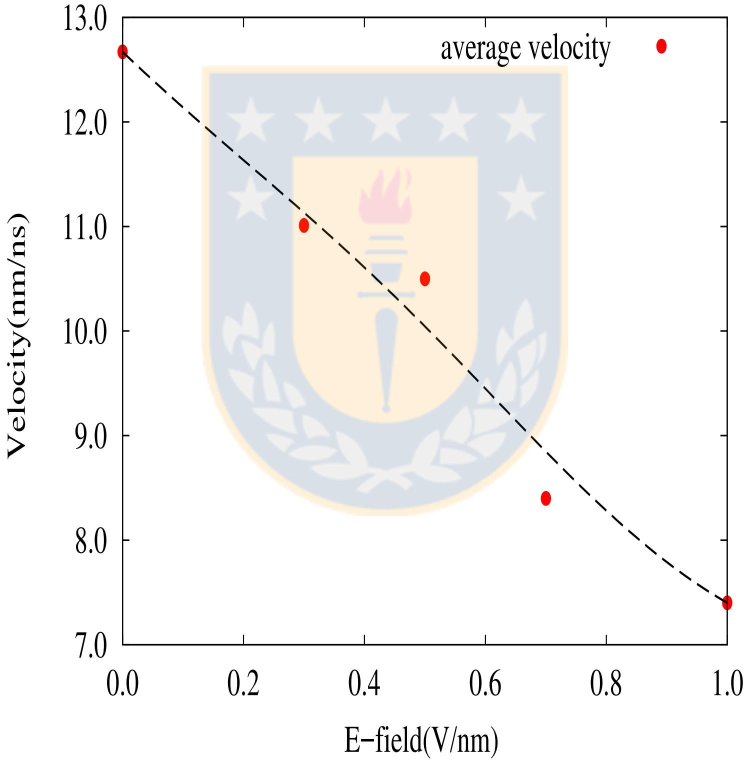

FIGURE C.1: Average velocity during the viscous regime during the nanocapillary imbibition at different electric field strength applied parallel to the flow direction.The dotted lines represents the tendency of monotonic decrease of the maximum velocity observed during the process. Source: Own elaboration.

C.2 S2. Orientation distribution of angle between the water dipole vector and the vector normal to the silica surface at different distance from the silica-wall for case without applied electric field

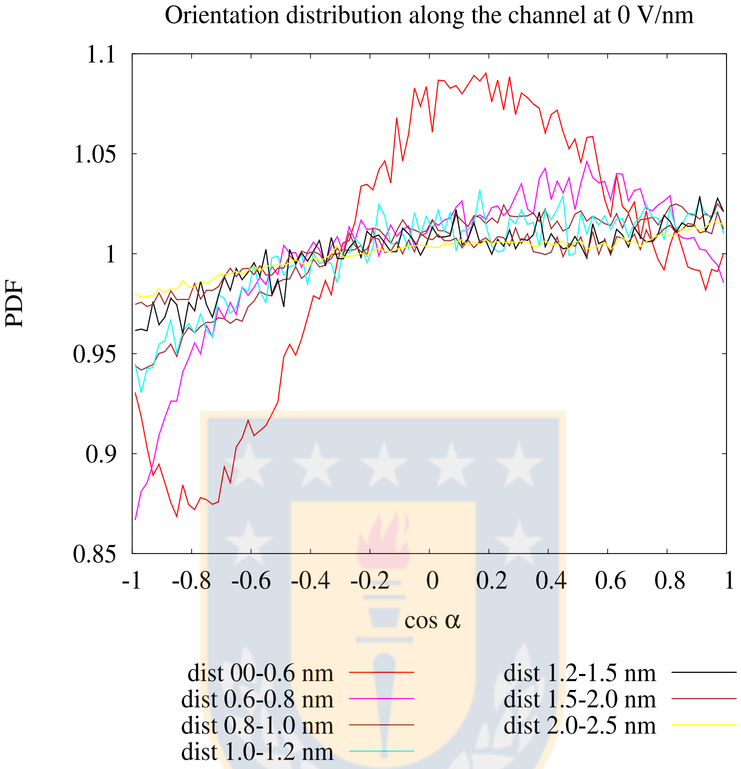

FIGURE C.2: Distribution function of angle between the water dipole and the normal to the silica wall for case without applied electric field. Source: Own elaboration.

It can be observed figure B.4 that the dipole orientation quickly converge to the bulk value at the distance away from 0.6 nm. This indicates that the surface walls of the capillary nanochannel significantly alter the water dipole orientation at the wall-water interface even in the absence of external electric field. This could probably be caused by the interaction of water molecules with the local electric field produced by the atoms of the wall.

C.3 S3.Orientation distribution of the angle between the vector normal to the silica wall and the vector joining the two hydrogen bonds for different applied field strength.

A complete picture of orientation of water molecules near a surface requieres the distribution function of two important angles made by the atoms of water molecules: 1) The angle between the water dipole and the vector normal to the silica walls. 2) The angle made by the vector connecting two hydrogen atoms with the vector normal to the silica walls. We plot the latter in figure B.5.

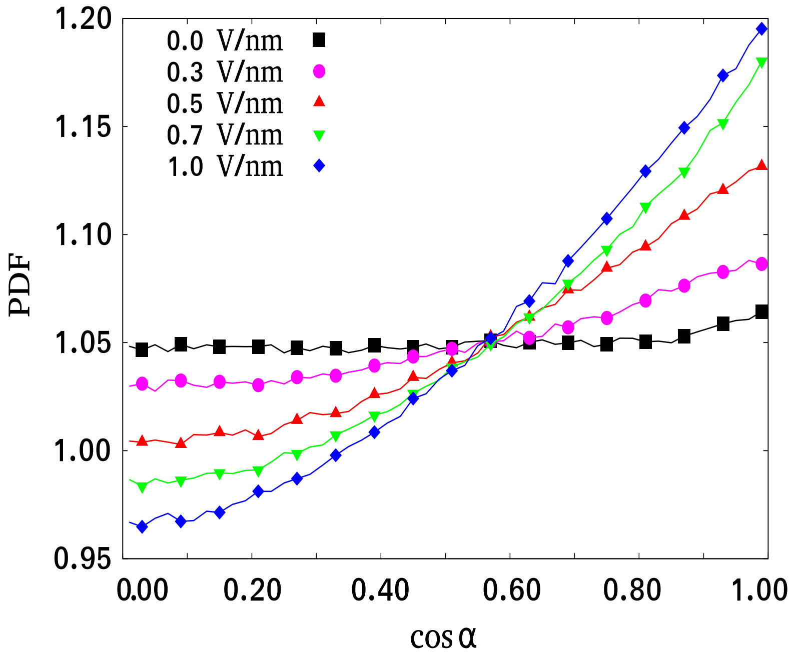

FIGURE C.3: Orientation distribution function of the angle between the vector normal to the silica wall and the vector joining the two hydrogen bonds for different applied field strength. This function is calculated at a distance between 1.5–2.0 nm from the lower wall surface. Source: Own elaboration.

C.4 S4. Orientation distribution of angle between the water dipole vector and the vector normal to the silica surface distance between 0-0.5 nm from the silica-wall for different applied electric field

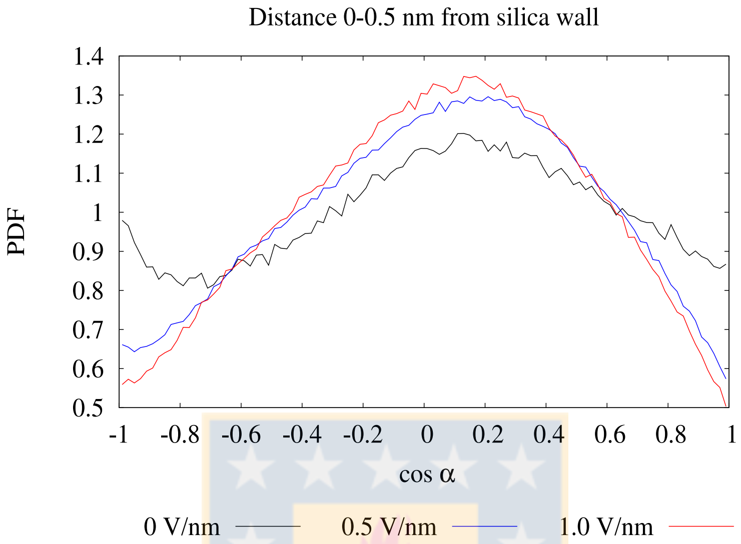

FIGURE C.4: Distribution function of angle between the water dipole and the normal to the silica wall for different applied electric field at a distance between 0-0.5 nm from the silica surface. Source: Own elaboration.

Bibliography

[1] P. Abgrall and N. T. Nguyen. Nanofluidic devices and their applications. *Analytical Chemistry*, 80(7):2326–2341, 2008.

[2] C. H. Ahn, J.-W. Choi, G. Beaucage, J. H. Nevin, J.-B. Lee, A. Puntambekar, and J. Y. Lee. Disposable smart lab on a chip for point-of-care clinical diagnostics. *Proceedings of the IEEE*, 92(1):154–173, 2004.

[3] B. J. Alder and T. E. Wainwright. Studies in molecular dynamics. i. general method. *The Journal of Chemical Physics*, 31(2):459–466, 1959.

[4] J. Alejandre, D. J. Tildesley, and G. A. Chapela. Molecular dynamics simulation of the orthobaric densities and surface tension of water. *The Journal of Chemical Physics*, 102(11):4574–4583, 1995.

[5] M. A. Alibakhshi, Y. Li, and C. Duan. Accurate measurement of liquid transport through nanoscale conduits. *Scientific Reports*, 6(14):24936, 2016. PMID: 27336652.

[6] M. P. Allen. Introduction to molecular dynamics simulation. *Computational Soft Matter: From Synthetic Polymers to Proteins*, 23:1–28, 2004.

[7] M. P. Allen and D. J. Tildesley. *Computer Simulation of Liquids*. Oxford University Press, Oxford, UK, 2nd edition, 2017.

[8] A. Ambrosetti, N. Ferri, R. A. DiStasio, and A. Tkatchenko. Wavelike charge density fluctuations and van der waals interactions at the nanoscale. *Science*, 351(6278):1171–1176, 2016.

[9] H. C. Andersen. Molecular dynamics simulations at constant pressure and/or temperature. *The Journal of Chemical Physics*, 72(4):2384–2393, 1980.

[10] H. C. Andersen. Rattle: A "velocity" version of the shake algorithm for molecular dynamics calculations. *Journal of Computational Physics*, 52(1):24 – 34, 1983.

[11] T. Andrukh, D. Monaenkova, B. Rubin, W.-K. Lee, and K. G. Kornev. Meniscus formation in a capillary and the role of contact line friction. *Soft Matter*, 10:609–615, 2014.

[12] D. Argyris, D. R. Cole, and A. Striolo. Ion-specific effects under confinement: The role of interfacial water. *ACS Nano.*, 4(4):2035–2042, 2010.

[13] A. Arnold and C. Holm. *Efficient Methods to Compute Long-Range Interactions for Soft Matter Systems*, pages 59–109. Springer Berlin Heidelberg, Berlin, Heidelberg, 2005.

[14] J. B. Asbury, T. Steinel, C. Stromberg, S. A. Corcelli, C. P. Lawrence, J. L. Skinner, and M. D. Fayer. Water dynamics: vibrational echo correlation spectroscopy and comparison to molecular dynamics simulations. *The Journal of Physical Chemistry A*, 108(7):1107–1119, 2004.

[15] C. Bakli and S. Chakraborty. Effect of presence of salt on the dynamics of water in uncharged nanochannels. *The Journal of Chemical Physics*, 138(5):054504, 2013.

[16] C. Bakli and S. Chakraborty. Rapid capillary filling via ion-water interactions over the nanoscale. *Nanoscale*, 8:6535–6541, 2016.

[17] M. Barletta and A. Gisario. Electrostatic spray painting of carbon fibre-reinforced epoxy composites. *Progress in Organic Coatings*, 64(4):339 – 349, 2009.

[18] J. E. Basconi and M. R. Shirts. Effects of temperature control algorithms on transport properties and kinetics in molecular dynamics simulations. *Journal of Chemical Theory and Computation*, 9(7):2887–2899, 2013.

[19] A. Bateni, S. Laughton, H. Tavana, S. Susnar, A. Amirfazli, and A. Neumann. Effect of electric fields on contact angle and surface tension of drops. *Journal of Colloid and Interface Science*, 283(1):215 – 222, 2005.

[20] G. L. Batten. Liquid imbibition in capillaries and packed beds. *J. Coll. Interface Sci.*, 102(2):513 – 518, 1984.

[21] O. Becker, A. Mackerell Jr, B. Roux, and M. Watanable. *Computational Biochemistry and Biophysics*. Marcel and Dekker,Inc., 1 edition, 2001.

[22] J. M. Bell and F. K. Cameron. The flow of liquids through capillary spaces. *J. Phys. Chem.*, 10(8):658–674, 1906.

[23] H. J. C. Berendsen. *Simulating the Physical World: Hierarchical Modeling from Quantum Mechanics to Fluid Dynamics*. Cambridge University Press, New York, NY, USA, 2007.

[24] H. J. C. Berendsen, J. R. Grigera, and T. P. Straatsma. The missing term in effective pair potentials. *J. Phys. Chem.*, 91:6269–6271, 1987.

[25] H. J. C. Berendsen, J. P. M. Postma, W. F. van Gunsteren, A. DiNola, and J. R. Haak. Molecular dynamics with coupling to an external bath. *J. Chem. Phys.*, 81(8):3684–3684, 1984.

[26] M. I. BernalUruchurtu and I. OrtegaBlake. A refined monte carlo study of mg2+ and ca2+ hydration. *The Journal of Chemical Physics*, 103(4):1588–1598, 1995.

[27] D. Bhatt, J. Newman, and C. J. Radke. Molecular dynamics simulations of surface tensions of aqueous electrolytic solutions. *The Journal of Physical Chemistry B*, 108(26):9077–9084, 2004.

[28] B. Bhushan, Y. Pan, and S. Daniels. Afm characterization of nanobubble formation and slip condition in oxygenated and electrokinetically altered fluids. *Journal of Colloid and Interface Science*, 392:105 – 116, 2013.

[29] A. Biswas, I. S. Bayer, A. S. Biris, T. Wang, E. Dervishi, and F. Faupel. Advances in top–down and bottom–up surface nanofabrication: Techniques, applications future prospects. *Adv. Coll. Interf. Sci.*, 170(1-2):2–27, 2012.

[30] O. Bjorneholm, M. H. Hansen, A. Hodgson, L.-M. Liu, D. T. Limmer, A. Michaelides, P. Pedevilla, J. Rossmeisl, H. Shen, G. Tocci, E. Tyrode, M.-M. Walz, J. Werner, and H. Bluhm. Water at interfaces. *Chemical Reviews.*, 116(13):7698–7726, 2016.

[31] T. Blake and J. D. Coninck. The influence of solid–liquid interactions on dynamic wetting. *Advances in Colloid and Interface Science*, 96(1):21 – 36, 2002. A Collection of Papers in Honour of Nikolay Churaev on the Occasion of his 80th Birthday.

[32] T. D. Blake. The physics of moving wetting lines. *Journal of Colloid and Interface Science*, 299(1):1 – 13, 2006.

[33] D. Boda and D. Henderson. The effects of deviations from lorentz-berthelot rules on the properties of a simple mixture. *Mol. Phys.*, 106(20):2367–2370, 2008.

[34] D. J. Bonthuis, D. Horinek, L. Bocquet, and R. R. Netz. Electrokinetics at aqueous interfaces without mobile charges. *Langmuir*, 26(15):12614–12625, 2010.

[35] C. H. Bosanquet. On the flow of liquids into capillary tubes. *Phil. Mag. Ser. 6*, 45(267):525–531, 1923.

[36] F. J. P. Bracke, M.and De Voeght. *Trends in Colloid and Interface Science III*, volume 136, chapter The kinetics of wetting: the dynamic contact angle, pages 142–149. Steinkopff, 1989.

[37] D. Bratko, C. D. Daub, and A. Luzar. Field-exposed water in a nanopore: liquid or vapour? *Phys. Chem. Chem. Phys.*, 10:6807–6813, 2008.

[38] E. Braun, S. Mohamad Moosavi, and B. Smit. Anomalous effects of velocity rescaling algorithms: the flying ice cube effect revisited. *ArXiv e-prints*, May 2018.

[39] F. Brochard-Wyart and P. de Gennes. Dynamics of partial wetting. *Advances in Colloid and Interface Science*, 39:1 – 11, 1992.

[40] M. A. Brown, Z. Abbas, A. Kleibert, R. G. Green, A. Goel, S. May, and T. M. Squires. Determination of surface potential and electrical double-layer structure at the aqueous electrolyte-nanoparticle interface. *Phys. Rev. X*, 6:011007, Jan 2016.

[41] H. Cabral, N. Nishiyama, and K. Kataoka. Supramolecular nanodevices: From design validation to theranostic nanomedicine. *Accounts of Chemical Research*, 44(10):999–1008, 2011. PMID: 21755933.

[42] K. M. Callahan, N. N. Casillas-Ituarte, M. Roeselová, H. C. Allen, and D. J. Tobias. Solvation of magnesium dication: Molecular dynamics simulation and vibrational spectroscopic study of magnesium chloride in aqueous solutions. *The Journal of Physical Chemistry A*, 114(15):5141–5148, 2010.

[43] C. D. Cappa, J. D. Smith, B. M. Messer, R. C. Cohen, and R. J. Saykally. Effects of cations on the hydrogen bond network of liquid water: new results from x-ray absorption spectroscopy of liquid microjets. *The Journal of Physical Chemistry B*, 110(11):5301–5309, 2006.

[44] A. Carlson, G. Bellani, and G. Amberg. Universality in dynamic wetting dominated by contact-line friction. *Phys. Rev. E*, 85:045302, Apr 2012.

[45] A. T. Celebi, M. Barisik, and A. Beskok. Electric field controlled transport of water in graphene nanochannels. *J. Comput. Phys.*, 147(16):1–10, 2017.

[46] A. S. Chacravarti and B. Prasad. Viscosity and density of aqueous solutions of barium chloride, magnesium chloride, cobalt chloride and nickel chloride at 35[degree] c. *Trans. Faraday Soc.*, 35:1466–1471, 1939.

[47] S. Chakraborty, H. Kumar, C. Dasgupta, and P. K. Maiti. Confined water: Structure, dynamics, and thermodynamics. *Acc. Chem. Res.*, 50(9):2139–2146, 2017.

[48] F. Chauvet, S. Geoffroy, A. Hamoumi, M. Prat, and P. Joseph. Roles of gas in capillary filling of nanoslits. *Soft Matter*, 8(41):10738, 2012.

[49] J. Chen, C. Xue, Y. Zhao, D. Chen, M.-H. Wu, and J. Wang. Microfluidic impedance flow cytometry enabling high-throughput single-cell electrical property characterization. *International Journal of Molecular Sciences*, 16(5):9804–9830, 2015.

[50] L. Chen and A. T. Conlisk. Electroosmotic flow and particle transport in micro/nano nozzles and diffusers. *Biom. Microdevices*, 10:289–298, 2008.

[51] X. Chen, G. Cao, A. Han, V. K. Punyamurtula, L. Liu, P. J. Culligan, T. Kim, and Y. Qiao. Nanoscale fluid transport: Size and rate effects. *Nano Letters*, 8(9):2988–2992, 2008. PMID: 18720972.

[52] X. Chen, P. Carbone, W. L. Cavalcanti, G. Milano, and F. Müller-Plathe. Viscosity and structural alteration of a coarse-grained model of polystyrene under steady shear flow studied by reverse nonequilibrium molecular dynamics. *Macromolecules*, 40(22):8087–8095, 2007.

[53] S. Chibbaro, L. Biferale, F. Diotallevi, S. Succi, K. Binder, D. Dimitrov, A. Milchev, S. Girardo, and D. Pisignano. Evidence of thin-film precursors formation in hydrokinetic and atomistic simulations of nanochannel capillary filling. *Europhys. Lett.*, 84(4):44003, 2008.

[54] M. Chiu and M. C. Herdbort. Molecular dynamics simulations on high-performance reconfigurable computing systems. *ACM transactions on reconfigurable technology and systems*, 3(24).

[55] K. Cho and J. D. Joannopoulos. Ergodicity and dynamical properties of constant-temperature molecular dynamics. *Phys. Rev. A*, 45:7089–7097, May 1992.

[56] C.-H. Choi, J. A. Westin, and K. S. Breuer. Apparent slip flows in hydrophilic and hydrophobic microchannels. 15(10):2897–2902, 2003.

[57] S. Chowdhuri and A. Chandra. Molecular dynamics simulations of aqueous nacl and kcl solutions: Effects of ion concentration on the single-particle, pair, and collective dynamical properties of ions and water molecules. *The Journal of Chemical Physics*, 115(8):3732–3741, 2001.

[58] S. Chowdhuri and A. Chandra. Hydrogen bonds in aqueous electrolyte solutions: Statistics and dynamics based on both geometric and energetic criteria. *Phys. Rev. E*, 66:041203, Oct 2002.

[59] G. Ciccotti, M. Ferrario, and J.-P. Ryckaert. Molecular dynamics of rigid systems in cartesian coordinates. a general formulation. *Mol. Phys.*, 47(6):1253–1264, 1982.

[60] K. Collins. Charge density-dependent strength of hydration and biological structure. *Biophysical Journal*, 72(1):65 – 76, 1997.

[61] T. Corridoni, R. Mancinelli, M. A. Ricci, and F. Bruni. Viscosity of aqueous solutions and local microscopic structure. *The Journal of Physical Chemistry B*, 115(48):14008–14013, 2011. PMID: 21859162.

[62] R. G. Cox. The dynamics of the spreading of liquids on a solid surface. *J. Fluid Mech.*, 168:169–194, 1986.

[63] R. G. Cox. Inertial and viscous effects on dynamic contact angles. *J. Fluid Mech.*, 357:249–278, 1998.

[64] E. R. Cruz-Chu, A. Aksimentiev, and K. Schulten. Water-silica force field for simulating nanodevices. *J. Phys. Chem. B*, 110:21497–21508, 2006.

[65] T. Darden, D. York, and L. Pedersen. Particle mesh Ewald: An $N \cdot \log N$ method for Ewald sums in large systems. *J. Chem. Phys.*, 98(12):10089–10092, 1993.

[66] S. Das, P. R. Waghmare, and S. K. Mitra. Early regimes of capillary filling. *Phys. Rev. E*, 86:067301, 2012.

[67] C. D. Daub, D. Bratko, K. Leung, and A. Luzar. Electrowetting at the nanoscale. *The Journal of Physical Chemistry C*, 111(2):505–509, 2007.

[68] C. D. Daub, D. Bratko, and A. Luzar. *Nanoscale Wetting Under Electric Field from Molecular Simulations*, pages 155–179. Springer Berlin Heidelberg, Berlin, Heidelberg, 2012.

[69] R. L. Davidchack, R. Handel, and M. V. Tretyakov. Langevin thermostat for rigid body dynamics. *The Journal of Chemical Physics*, 130(23):234101, 2009.

[70] I. S. Davis, B. Shachar-Hill, M. R. Curry, K. S. Kim, T. J. Pedley, and A. E. Hill. Osmosis in semi-permeable pores: an examination of the basic flow equations based on an experimental and molecular dynamics study. *Proc. R. Soc. A*, 463:881–896, 2007.

[71] B.-W. F. Q. D. de Gennes, Pierre-Gilles. *Surface Tension*, chapter Capillarity:Deformable interfaces, pages 3–11. Springer, 2004.

[72] B.-W. F. Q. D. de Gennes, Pierre-Gilles. *Surface Tension*, chapter Capillarity:Deformable interfaces, pages 132–133. Springer, 2004.

[73] A. V. Delgado, F. Gonzalez-Caballero, R. J. Hunter, L. K. Koopal, and J. Lyklema. Measurement and interpretation of electrokinetic phenomena. *Pure Appl. Chem.*, 77(10):1753–1805, 2005.

[74] D. Di Tommaso, E. Ruiz-Agudo, N. H. de Leeuw, A. Putnis, and C. V. Putnis. Modelling the effects of salt solutions on the hydration of calcium ions. *Phys. Chem. Chem. Phys.*, 16:7772–7785, 2014.

[75] D. I. Dimitrov, A. Milchev, and K. Binder. Forced imbibition a tool for separate determination of laplace pressure and drag force in capillary filling experiments. *Phys. Chem. Chem. Phys.*, 10:1867–1869, 2008.

[76] P. S. Dittrich and A. Manz. Lab-on-a-chip: microfluidics in drug discovery. *Nature Reviews Drug Discovery*, 5(210):154–173, 2006.

[77] M. H. Du, L. L. Wang, A. Kolchin, and H. P. Cheng. Water-silica interaction in clusters. *Eur. Phys. J. D*, 24:323–326, 2003.

[78] D. Duncan, D. Li, J. Gaydos, and A. Neumann. Correlation of line tension and solid-liquid interfacial tension from the measurement of drop size dependence of contact angles. *Journal of Colloid and Interface Science*, 169(2):256 – 261, 1995.

[79] R. Durikovic and T. Motooka. Modeling material behavior: molecular dynamics simulation and visualization. In *Proceedings Shape Modeling International '99. International Conference on Shape Modeling and Applications*, pages 186–191, March 1999.

[80] J. D. Durrant and J. A. McCammon. Molecular dynamics simulations and drug discovery. *BMC Biology*, 9(1):71, Oct 2011.

[81] E. B. Dussan. On the spreading of liquids on solid surfaces: Static and dynamic contact lines. *Annu. Rev. Fluid Mech.*, 11(1):371–400, 1979.

[82] D. Duvivier, T. D. Blake, and J. De Coninck. Toward a predictive theory of wetting dynamics. *Langmuir*, 29(32):10132, 2013.

[83] J. Dzubiella, R. J. Allen, and J.-P. Hansen. Electric field-controlled water permeation coupled to ion transport through a nanopore. *JChemP*, 120(11):5001–5004, 2004.

[84] J. C. T. Eijkel and A. van den Berg. Nanofluidics: What is it and what can we expect from it? *Microfluid. Nanofluid.*, 1:249–267, 2005.

[85] J. E. Enderby. The solvation of ions. *Journal of Physics: Condensed Matter*, 3(42):F87, 1991.

[86] N. J. English and J. M. D. MacElroy. Hydrogen bonding and molecular mobility in liquid water in external electromagnetic fields. *The Journal of Chemical Physics*, 119(22):11806–11813, 2003.

[87] N. J. English and C. J. Waldron. Perspectives on external electric fields in molecular simulation: progress, prospects and challenges. *Phys. Chem. Chem. Phys.*, 17:12407–12440, 2015.

[88] U. Essmann, L. Perera, M. L. Berkowitz, T. Darden, H. Lee, and L. G. Pedersen. A smooth particle mesh Ewald method. *J. Chem. Phys.*, 103(19):8577–8593, 1995.

[89] P. P. Ewald. Die berechnung optischer und elektrostatische gitterpotentiale. *Annalen der Physik*, 64:253–287, 1921.

[90] K. Falk, F. Sedlmeier, L. Joly, R. R. Netz, and L. Bocquet. Molecular origin of fast water transport in carbon nanotube membranes: Superlubricity versus curvature dependent friction. *Nano Letters*, 10(10):4067–4073, 2010. PMID: 20845964.

[91] K. Falk, F. Sedlmeier, L. Joly, R. R. Netz, and L. Bocquet. Ultralow liquid/solid friction in carbon nanotubes: Comprehensive theory for alcohols, alkanes, omcts, and water. *Langmuir*, 28(40):14261–14272, 2012. PMID: 22974715.

[92] T. M. C. Faro, G. P. Thim, and M. S. Skaf. A lennard-jones plus coulomb potential for al3+ ions in aqueous solutions. *The Journal of Chemical Physics*, 132(11):114509, 2010.

[93] C. J. Fecko, J. J. Loparo, S. T. Roberts, and A. Tokmakoff. Local hydrogen bonding dynamics and collective reorganization in water: Ultrafast infrared spectroscopy of hod/d2o. *The Journal of Chemical Physics*, 122(5):054506, 2005.

[94] M. Ferrari. Cancer nanotechnology: opportunities and challenges. *NRCR*, 5:161–171, 2005.

[95] L. R. Fisher and P. D. Lark. An experimental study of the washburn equation for liquid flow in very fine capillaries. *Journal of Colloid and Interface Science*, 69(3):486 – 492, 1979.

[96] D. Frenkel and B. Smit. *Understanding Molecular Simulation*. Academic Press, San Diego, 2nd edition, 2002.

[97] N. Fries and M. Dreyer. The transition from inertial to viscous flow in capillary rise. *J. Coll. Interface Sci.*, 327:125–128, 2008.

[98] H. Frolich. *Theory of dielectrics dielectric constant and dielectric loss*. Oxford University Press, 2nd edition, 1990.

[99] M. Fuest, C. Boone, K. K. Rangharajan, A. T. Conlisk, and S. Prakash. A three-state nanofluidic field effect switch. *Nano Letters*, 15(4):2365–2371, 2015. PMID: 25730552.

[100] Z. Futera and N. J. English. Communication: Influence of external static and alternating electric fields on water from long-time non-equilibrium ab initio molecular dynamics. *The Journal of Chemical Physics*, 147(3):031102, 2017.

[101] . G. Martic, T. D. Blake, and J. D. Coninck. Dynamics of imbibition into a pore with a heterogeneous surface. *Adv. Coll. Interf. Sci.*, 21(24):11201–11207, 2005.

[102] N. Gao and X. Li. *5 - Controlled drug delivery using microfluidic devices*, pages 167 – 185e. Woodhead Publishing Series in Biomaterials. Woodhead Publishing, 2013.

[103] X. Gao, J. Fang, and H. Wang. Kaiser-bessel basis for particle-mesh interpolation. *Phys. Rev. E*, 95:063303, Jun 2017.

[104] J.-A. Garate, N. J. English, and J. M. D. MacElroy. Static and alternating electric field and distance-dependent effects on carbon nanotube-assisted water self-diffusion across lipid membranes. *The Journal of Chemical Physics*, 131(11):114508, 2009.

[105] E. N. Gatimu, J. V. Sweedler, and P. W. Bohn. Nanofluidics and the role of nanocapillary array membranes in mass-limited chemical analysis. *Analyst*, 131:705–709, 2006.

[106] S. Gavryushov. Dielectric saturation of the ion hydration shell and interaction between two double helices of dna in mono- and multivalent electrolyte solutions: foundations of the -modified poissonboltzmann theory. *The Journal of Physical Chemistry B*, 111(19):5264–5276, 2007. PMID: 17439264.

[107] P. G. D. Gennes, F. Brochard-Wyart, D. Quéré, A. Reisinger, and B. Widom. Capillarity and Wetting Phenomena: Drops, Bubbles, Pearls, Waves. *Physics Today*, 57(12):120000–67, Dec. 2004.

[108] N. Giovambattista, P. G. Debenedetti, and P. Rossky. Effect of surface polarity on water contact angle and interfacial hydration structure. *J. Phys. Chem. B*, 111(32):9581–9587, 2007.

[109] M. Goel. Electret sensors, filters and mems devices: New challenges in materials research. *Curr. Sci.*, 85(4):443–453, 2003.

[110] E. M. Gosling, I. McDonald, and K. Singer. On the calculation by molecular dynamics of the shear viscosity of a simple fluid. *Molecular Physics*, 26(6):1475–1484, 1973.

[111] S. Gravelle, L. Joly, F. Detcheverry, C. Ybert, C. Cottin-Bizonne, and L. Bocquet. Optimizing water permeability through the hourglass shape of aquaporins. *Proc. Natl. Acad. Sci. USA*, 110(41):16367, 2013.

[112] C. E. Grimes, J. Kestin, and H. E. Khalifa. Viscosity of aqueous potassium chloride solutions in the temperature range 25-150 .degree.c and the pressure range 0-30 mpa. *Journal of Chemical & Engineering Data*, 24(2):121–126, 1979.

[113] S. Gruener, T. Hofmann, D. Wallacher, A. V. Kityk, and P. Huber. Capillary rise of water in hydrophilic nanopores. *Phys. Rev. E*, 79:067301, Jun 2009.

[114] Y. Guissani and B. Guillot. A numerical investigation of the liquid-vapor coexistence curve of silica. *J. Chem. Phys.*, 104(19):7633–7644, 1996.

[115] G. J. Guo, Y. G. Zhang, K. Refson, and Y. J. Zhao. Viscosity and stress autocorrelation function in supercooled water: a molecular dynamics study. *Molecular Physics*, 100(16):2617–2627, 2002.

[116] E. M. Gutman. On the thermodynamic definition of surface stress. *Journal of Physics: Condensed Matter*, 7(48):L663, 1995.

[117] E. Guàrdia, R. Rey, and J. Padró. Potential of mean force by constrained molecular dynamics: A sodium chloride ion-pair in water. *Chemical Physics*, 155(2):187 – 195, 1991.

[118] S. Haeberle and R. Zengerle. Microfluidic platforms for lab-on-a-chip applications. *Lab Chip*, 7:1094–1110, 2007.

[119] J. M. Haile. *Molecular Dynamics Simulation: Elementary Methods*. A Wiley interscience publication, 1st edition, 1993.

[120] A. Hamraoui, K. Thuresson, T. Nylander, and V. Yaminsky. Can a dynamic contact angle be understood in terms of a friction coefficient? *J. Coll. Interface Sci.*, 226(2):199 – 204, 2000.

[121] J. Haneveld, N. Tas, N. Brunets, H. Jansen, and M. Elwenspoek. Capillary filling of sub-10 nm nanochannels. *J. Appl. Phys.*, 104:014309, 2008.

[122] N. R. Haria, G. S. Grest, and C. D. Lorenz. Viscosity of nanoconfined water between hydroxyl basal surfaces of kaolinite: Classical simulation results. *The Journal of Physical Chemistry C*, 117(12):6096–6104, 2013.

[123] M. F. Harrach, F. Klameth, B. Drossel, and M. Vogel. Effect of the hydroaffinity and topology of pore walls on the structure and dynamics of confined water. *J. Chem. Phys.*, 142(3):034703, 2015.

[124] D. G. Haywood, A. Saha-Shah, L. A. Baker, and S. C. Jacobson. Fundamental studies of nanofluidics: Nanopores, nanochannels, and nanopipets. *Analytical Chemistry*, 87(1):172–187, 2015. PMID: 25405581.

[125] Y. He, D. Gillespie, D. Boda, I. Vlassiouk, R. S. Eisenberg, and Z. S. Siwy. Tuning transport properties of nanofluidic devices with local charge inversion. *Journal of the American Chemical Society*, 131(14):5194–5202, 2009. PMID: 19317490.

[126] M. Henderson. The interaction of water with solid surfaces: fundamental aspects revisited. *Surf. Sci. Rep.*, 46(1–8):1–308, 2002.

[127] B. Hess. Determining the shear viscosity of model liquids from molecular dynamics simulations. *The Journal of Chemical Physics*, 116(1):209–217, 2002.

[128] B. Hess. P-lincs: a parallel linear constraint solver for molecular simulation. *Journal of Chemical Theory and Computation*, 4(1):116–122, 2008. PMID: 26619985.

[129] P. Hiemenz and R. Rajagopalan. *Principles of Colloid and Surface Chemistry, Revised and Expanded*. CRC Press, 3rd edition, 1997.

[130] T. Hill. *An Introduction to Statistical Thermodynamics*. Addison-Wesley series in chemistry. Dover Publications, 1986.

[131] C. Ho, R. Qiao, J. B. Heng, A. Chatterjee, R. J. Timp, N. R. Aluru, and G. Timp. Electrolytic transport through a synthetic nanometer-diameter pore. *Proc. Natl. Acad. Sci. USA*, 102(30):10445–10450, 2005.

[132] R. W. Hockney and J. W. Eastwood. *Computer Simulation Using Particles*. Taylor & Francis, Inc., Bristol, PA, USA, 1988.

[133] W. G. Hoover. Canonical dynamics: Equilibrium phase-space distributions. *Phys. Rev. A*, 31:1695–1697, Mar 1985.

[134] R. HORNE. The structure of water and aqueous solutions. In A. F. SCOTT, editor, *Survey of Progress in Chemistry*, volume 4 of *Survey of Progress in Chemistry*, pages 1 – 43. Elsevier, 1968.

[135] B. Hribar, N. T. Southall, V. Vlachy, and K. A. Dill. How ions affect the structure of water. *Journal of the American Chemical Society*, 124(41):12302–12311, 2002. PMID: 12371874.

[136] C. Huang, C. Li, P. Y. Choi, K. Nandakumar, and L. W. Kostiuk. Effect of cut-off distance used in molecular dynamics simulations on fluid properties. *Molecular Simulation*, 36(11):856–864, 2010.

[137] K. D. Huang and R. J. Yang. Electrokinetic behaviour of overlapped electric double layers in nanofluidic channels. *Nanotechnol.*, 18(115701):1–6, 2007.

[138] E. Hückel. *Zur Theorie der Elektrolyte*, pages 199–276. Springer Berlin Heidelberg, Berlin, Heidelberg, 1924.

[139] N. T. Huff, E. Demiralp, T. Cagin, and W. A. Goddard. Factors affecting molecular dynamics simulated vitreous silica structures. *J. Non-Crystal. Solids*, 253:133–142, 1999.

[140] C. Huh and L. E. Scriven. Hydrodynamic model of steady movement of a solid/liquid/fluid contact line. *J. Coll. Interface Sci.*, 35:85–101, 1971.

[141] M. Hultmark, J. M. Aristoff, and H. A. Stone. The influence of the gas phase on liquid imbibition in capillary tubes. *J. Fluid Mech.*, 678(7):600–606, 2011.

[142] P. H. Hünenberger. *Thermostat Algorithms for Molecular Dynamics Simulations*, pages 105–149. Springer Berlin Heidelberg, Berlin, Heidelberg, 2005.

[143] T. Ikeda, M. Boero, and K. Terakura. Hydration properties of magnesium and calcium ions from constrained first principles molecular dynamics. *The Journal of Chemical Physics*, 127(7):074503, 2007.

[144] R. W. Impey, P. A. Madden, and I. R. McDonald. Hydration and mobility of ions in solution. *The Journal of Physical Chemistry*, 87(25):5071–5083, 1983.

[145] W. Ip, S and J. Toguri. The equivalency of surface tension, surface energy and surface free energy. *Journal of Materials Science*, 29(688), 1994.

[146] J. N. Israelachvili. *Intermolecular and surface forces: revised third edition*. Academic press, 3 edition, 2011.

[147] J. d. B. D. B. J. R. C. van der Maarel, H. R. W. M. de Boer and J. C. Leyte. On the structure and dynamics of water in$AlCl_3$ solutions from h, d, 17o, and al27 nuclear magnetic relaxation. *Journal of Chemical Physics*, 86(6):3373–3379, 1987.

[148] A. Jang, Z. Zou, K. K. Lee, C. H. Ahn, and P. L. Bishop. State-of-the-art lab chip sensors for environmental water monitoring. *Measurement Science and Technology*, 22(3):032001, 2011.

[149] T. Jiang, O. Soo-Gun, and J. C. Slattery. Correlation for dynamic contact angle. *J. Coll. Interface Sci.*, 69(1):74–77, 1979.

[150] L. Joly. Capillary filling with giant liquid/solid slip: Dynamics of water uptake by carbon nanotubes. *J. Chem. Phys.*, 135(21):–, 2011.

[151] S. Jomeh and M. Hoorfar. Study of the effect of electric field and electroneutrality on transport of biomolecules in microreactors. *Microfluid. Nanofluid.*, Published on the web:1–16, 2011.

[152] G. Jones and M. Dole. The viscosity of aqueous solutions of strong electrolytes with special reference to barium chloride. *Journal of the American Chemical Society*, 51(10):2950–2964, 1929.

[153] P. Joos, P. van Remoortere, and M. Bracke. The kinetics of wetting in a capillary. *J. Coll. Interface Sci.*, 136(1):189–197, 1990.

[154] S. Joseph and N. R. Aluru. Hierarchical multiscale simulation of electrokinetic transport in silica nanochannels a the point of zero charge. *Langmuir*, 22(21):9041–9051, 2006.

[155] D. H. Jung, J. H. Yang, and M. S. Jhon. The effect of an external electric field on the structure of liquid water using molecular dynamics simulations. *Chemical Physics*, 244(2):331 – 337, 1999.

[156] P. Jungwirth and D. J. Tobias. Specific ion effects at the air/water interface. *Chemical Reviews*, 106(4):1259–1281, 2006. PMID: 16608180.

[157] A. Kalra, N. Tugcu, S. M. Cramer, and S. Garde. Salting-in and salting-out of hydrophobic solutes in aqueous salt solutions. *The Journal of Physical Chemistry B*, 105(27):6380–6386, 2001.

[158] S. Kang and Y. K. Suh. Electroosmotic flows in an electric double layer overlapped channel with rectangle-waved surface roughness. *Microfluid. Nanofluid.*, 7:337–352, 2009.

[159] N. K. Karna, E. Oyarzua, J. H. Walther, and H. A. Zambrano. Effect of the meniscus contact angle during early regimes of spontaneous imbibition in nanochannels. *Phys. Chem. Chem. Phys.*, 18:31997–32001, 2016.

[160] S. Kawai, A. S. Foster, T. Bjorkman, J. Björk, F. F. Canova, L. H. Gade, T. A. Jung, and E. Meyer. Van der waals interactions and the limits of isolated atom models at interfaces. *Nature Communications*, 7(11559), 2016.

[161] S. Kelly, C. Torres-Verdin, and M. T. Balhoff. Anomalous liquid imbibition at the nanoscale: the critical role of interfacial deformations. *Nanoscale*, 8:2751–2767, 2016.

[162] S. Kerisit, E. S. Ilton, and S. C. Parker. Molecular dynamics simulations of electrolyte solutions at the (100) goethite surface. *The Journal of Physical Chemistry B*, 110(41):20491–20501, 2006. PMID: 17034235.

[163] J. S. Kim, Z. Wu, A. R. Morrow, A. Yethiraj, and A. Yethiraj. Self-diffusion and viscosity in electrolyte solutions. *The Journal of Physical Chemistry B*, 116(39):12007–12013, 2012. PMID: 22967241.

[164] S. A. Kislenko, R. H. Amirov, and I. S. Samoylov. Molecular dynamics simulation of the electrical double layer in ionic liquids. *Journal of Physics: Conference Series*, 418(1):012021, 2013.

[165] C. Kittel. *Introduction to Solid State Physics*. Wiley, 8th edition, 2004.

[166] J. Kofinger, G. Hummer, and C. Dellago. Macroscopically ordered water in nanopores. *Proc. Natl. Acad. Sci. USA*, 105(36):13218–13222, 2008.

[167] S. Koneshan, J. C. Rasaiah, R. M. Lynden-Bell, and S. H. Lee. Solvent structure, dynamics, and ion mobility in aqueous solutions at 25°c. *J. Phys. Chem. B*, 102:4193–4204, 1998.

[168] K. G. Kornev and A. V. Neimark. Spontaneous penetration of liquids into capillaries and porous membranes revisited. *J. Coll. Interface Sci.*, 235(1):101–113, 2001.

[169] M. L. Kovarik and S. C. Jacobson. Attoliter-scale dispensing in nanofluidic channels. *Anal. Chem.*, 79(4):1655–1660, 2007.

[170] T. Krupenkin and J. A. Taylor. Reverse electrowetting as a new approach to high-power energy harvesting. *Nature*, 2(2):448, 2011.

[171] B. K. Ku and S. S. Kim. Electrohydrodynamic spraying characteristics of glycerol solutions in vacuum. *Journal of Electrostatics*, 57(2):109 – 128, 2003.

[172] C.-C. Lai, C.-J. Chang, Y.-S. Huang, W.-C. Chang, F.-G. Tseng, and Y.-L. Chueh. Desalination of saline water by nanochannel arrays through manipulation of electrical double layer. *Nano Energy*, 12:394 – 400, 2015.

[173] P. S. Laplace. Traite de mecanique celeste. *Courcier Paris*, (Sur L'Action Capillaire):349–498, 1805.

[174] A. Leach. 4.05 - ligand-based approaches: Core molecular modeling. In J. B. Taylor and D. J. Triggle, editors, *Comprehensive Medicinal Chemistry II*, pages 87 – 118. Elsevier, Oxford, 2007.

[175] A. R. Leach. *Molecular modelling : principles and applications*. Pearson Prentice Hall, 2 edition, Apr. 2009.

[176] C. Lee, C. Cottin-Bizonne, R. Fulcrand, L. Joly, and C. Ybert. Nanoscale dynamics versus surface interactions: What dictates osmotic transport? *The Journal of Physical Chemistry Letters*, 8(2):478–483, 2017. PMID: 28067521.

[177] J. Lee, T. Laoui, and R. Karnik. Nanofluidic transport governed by the liquid/vapour interface. *Nature Nanotechnol.*, 9(4):1–7, 2014.

[178] S. H. Lee and J. C. Rasaiah. Molecular dynamics simulation of ionic mobility. i. alkali metal cations in water at 25°c. *The Journal of Chemical Physics*, 101(8):6964–6974, 1994.

[179] E. J. LeGrand and W. A. Rense. Data on rate of capillary rise. *J. Appl. Phys.*, 16(12):843–846, 1945.

[180] W. Lei and D. R. McKenzie. Nanoscale capillary flows in alumina: Testing the limits of classical theory. *The Journal of Physical Chemistry Letters*, 7(14):2647–2652, 2016. PMID: 27336652.

[181] B. J. Leimkuhler, S. Reich, and R. D. Skeel. *Integration Methods for Molecular Dynamics*, pages 161–185. Springer New York, New York, NY, 1996.

[182] A. S. Lemak and N. K. Balabaev. On the berendsen thermostat. *Molecular Simulation*, 13(3):177–187, 1994.

[183] N. E. Levinger. Water in confinement. *Science*, 298(5599):1722–1723, 2002.

[184] M. Levitt, M. Hirshberg, K. E. Laidig, and V. Daggett. Calibration and testing of a water model for simulation of the molecular dynamics of proteins and nucleic acids in solution. *J. Phys. Chem. B*, 101:5051–5061, 1997.

[185] L. Li, Y. Kazoe, K. Mawatari, Y. Sugii, and T. Kitamori. Viscosity and wetting property of water confined in extended nanospace simultaneously measured from highly-pressurized meniscus motion. *J. Phys. Chem. Lett.*, 3(17):2447–2452, 2012.

[186] P. C. H. Li and D. J. Harrison. Transport, manipulation, and reaction of biological cells on-chip using electrokinetic effects. *Analytical Chemistry*, 69(8):1564–1568, 1997. PMID: 9109354.

[187] Y. Li, F. Wang, and H. Liu, Heand Wu. Nanoparticle-tuned spreading behavior of nanofluid droplets on the solid substrate. *Microfluidics and Nanofluidics*, 18(1):111–120, Jan 2015.

[188] D. Lindbo and A.-K. Tornberg. Spectral accuracy in fast ewald-based methods for particle simulations. *Journal of Computational Physics*, 230(24):8744 – 8761, 2011.

[189] C. Liu and Z. Li. On the validity of the navier-stokes equations for nanoscale liquid flows: The role of channel size. *AIP Advances*, 1(3):032108, 2011.

[190] H. Liu and G. Cao. Effectiveness of the young-laplace equation at nanoscale. *Scientific Reports*, 6(23936), 2016.

[191] X. Liu, S. K. Schnell, J.-M. Simon, D. Bedeaux, S. Kjelstrup, A. Bardow, and T. J. H. Vlugt. Fick diffusion coefficients of liquid mixtures directly obtained from equilibrium molecular dynamics. *The Journal of Physical Chemistry B*, 115(44):12921–12929, 2011. PMID: 21954841.

[192] C. D. Lorenz, P. S. Crozier, J. A. Anderson, and A. Travesset. Molecular dynamics of ionic transport and electrokinetic effects in realistic silica channels. *J. Phys. Chem. C*, 112:10222–10232, 2008.

[193] D. Lu, A. Aksimentiev, A. Y. Shih, E. Cruz-Chu, P. L. Freddolino, A. Arkhipov, and K. Schulten. The role of molecular modeling in bionanotechnology. *Physical Biology*, 3(1):S40, 2006.

[194] A. Lukyanov and Y. Shikhmurzaev. Effect of flow field and geometry on the dynamic contact angle. *Phys. Rev.*, 75(5):1539–3755, 2007.

[195] A. V. Lukyanov and A. E. Likhtman. Dynamic contact angle at the nanoscale: A unified view. *ACS Nano*, 10(6):6045–6053, 2016. PMID: 27276341.

[196] J. B. Luo, M. W. Shen, and S. Z. Wen. Tribological properties of nanoliquid film under an external electric field. *Journal of Applied Physics*, 96(11):6733–6738, 2004.

[197] J. Lyklema, S. Rovillard, and J. De Coninck. Electrokinetics: the properties of the stagnant layer unraveled. *Langmuir*, 14(20):5659–5663, 1998.

[198] J. M. D. MacElroy and N. English. Electric-field and friction effects on carbon nanotube-assisted water self-diffusion across lipid membranes. In M. Naraghi, editor, *Carbon Nanotubes*, chapter 21. InTech, Rijeka, 2011.

[199] P. A. Mante, C. C. Chen, Y. C. Wen, H. Y. Chen, S. C. Yang, Y. R. Huang, I. Ju Chen, Y. W. Chen, V. Gusev, M. J. Chen, J. L. Kuo, J. K. Sheu, and C. K. Sun. Probing hydrophilic interface of solid/liquid-water by nanoultrasonics. 4(6249):1–6, 2014.

[200] C. Marculescu, B. Tincu, A. Avram, T. Burinaru, and M. Avram. Computational prediction of capillary number impact on droplets formation in microchannels. *Energy Procedia*, 85:339 – 349, 2016. EENVIRO-YRC 2015 - Bucharest.

[201] Y. Marcus. Effect of ions on the structure of water: Structure making and breaking. *Chemical Reviews*, 109(3):1346–1370, 2009.

[202] G. Martic, F. Gentner, D. Seveno, D. Coulon, J. De Coninck, and T. D. Blake. A molecular dynamics simulation of capillary imbibition. *Langmuir*, 18(21):7971–7976, 2002.

[203] M. Matsumoto, Y. Takaoka, and Y. Kataoka. Liquid–vapor interface of water–methanol mixture. i. computer simulation. *The Journal of Chemical Physics*, 98(2):1464–1472, 1993.

[204] J.-J. Max, V. Gessinger, C. van Driessche, P. Larouche, and C. Chapados. Infrared spectroscopy of aqueous ionic salt solutions at low concentrations. *The Journal of Chemical Physics*, 126(18):184507, 2007.

[205] G. McHale, M. I. Newton, and N. J. Shirtcliffe. Dynamic wetting and spreading and the role of topography. *Journal of Physics: Condensed Matter*, 21(46):464122, 2009.

[206] S. McLaughlin and R. T. Mathias. Electroosmosis and the reabsorption of fluid in renal proximal tubules. *J. Gen. Physiol.*, 85:699–728, 1985.

[207] T. M.Druchok, M.Holovko. A molecular dynamics study of al3+ in water: hydrolysis effects. *Condensed Matter Physics*, 4(4(40)):699–707, 2004.

[208] M. Michelsen and J. Mollerup. *Thermodynamic Modelling: Fundamentals and Computational Aspects*. Tie-Line Publications, 2004.

[209] M. I. Mohammed, S. Haswell, and I. Gibson. Lab-on-a-chip or chip-in-a-lab: Challenges of commercialization lost in translation. *Procedia Technology*, 20:54 – 59, 2015. Proceedings of The 1st International Design Technology Conference, DESTECH2015, Geelong.

[210] N. A. Mortensen and A. Kristensen. Electroviscous effects in capillary filling of nanochannels. *Applied Physics Letters*, 92(6):063110, 2008.

[211] A. Mudi and C. Chakravarty. Effect of the berendsen thermostat on the dynamical properties of water. *Molecular Physics*, 102(7):681–685, 2004.

[212] F. Mugele and J.-C. Baret. Electrowetting: from basics to applications. *Journal of Physics: Condensed Matter*, 17(28):R705, 2005.

[213] S. Mukhopadhyay, S. S. Roy, R. A. D'Sa, A. Mathur, R. J. Holmes, and J. A. McLaughlin. Nanoscale surface modifications to control capillary flow characteristics in pmma microfluidic devices. *Nanoscale Research Letters*, 6(1):411, Jun 2011.

[214] D. Myers. *Surfaces, Interfaces, and Colloids: Principles and Applications*, chapter Surfaces and Interfaces: General Concepts, pages 415–447. Wiley, 2002.

[215] T. J. Müller, M. Al-Samman, and F. Müller-Plathe. The influence of thermostats and manostats on reverse nonequilibrium molecular dynamics calculations of fluid viscosities. *The Journal of Chemical Physics*, 129(1):014102, 2008.

[216] Y. Nakamura, A. Carlson, G. Amberg, and J. Shiomi. Dynamic wetting at the nanoscale. *Phys. Rev. E*, 88:033010, Sep 2013.

[217] M. Nikzad, A. R. Azimian, M. Rezaei, and S. Nikzad. Water liquid-vapor interface subjected to various electric fields: A molecular dynamics study. *The Journal of Chemical Physics*, 147(20):204701, 2017.

[218] S. Nose. A molecular dynamics method for simulations in the canonical ensemble. *Molecular Physics*, 52(2):255–268, 1984.

[219] S. Obst and H. Bradaczek. Molecular dynamics study of the structure and dynamics of the hydration shell of alkaline and alkaline-earth metal cations. *The Journal of Physical Chemistry*, 100(39):15677–15687, 1996.

[220] V. Okhonin, X. Liu, and S. N. Krylov. Transverse diffusion of laminar flow profiles to produce capillary nanoreactors. *Anal. Chem.*, 77(18):5925–5929, 2005.

[221] D. Ortiz-Young, H.-C. Chiu, S. Kim, K. Voitchovsky, and E. Riedo. The interplay between apparent viscosity and wettability in nanoconfined water. 4(2482):1–6, 2013.

[222] E. Oyarzua, J. H. Walther, C. M. Megaridis, P. Koumoutsakos, and H. A. Zambrano. Carbon nanotubes as thermally induced water pumps. *ACS Nano.*, 11(10):9997–10002, 2017.

[223] E. Oyarzua, J. H. Walther, A. Mejia, and Z. H. A. Early regimes of water capillary flow in slit silica nanochannels. *Phys. Chem. Chem. Phys.*, 17(1):14731–14739, 2015.

[224] Y. Pan and B. Bhushan. Role of surface charge on boundary slip in fluid flow. *Journal of Colloid and Interface Science*, 392:117 – 121, 2013.

[225] S.-m. Park, Y. S. Huh, H. G. Craighead, and D. Erickson. A method for nanofluidic device prototyping using elastomeric collapse. 106(37):15549–15554, 2009.

[226] H. Peng, G. R. Birkett, and A. V. Nguyen. The impact of line tension on the contact angle of nanodroplets. *Molecular Simulation*, 40(12):934–941, 2014.

[227] F. Persson, L. H. Thamdrup, M. B. L. Mikkelsen, S. E. Jaarlgard, P. Skafte-Pedersen, H. Bruus, and A. Kristensen. Double thermal oxidation scheme for the fabrication of sio 2 nanochannels. *Nanotechnology*, 18(24):245301, 2007.

[228] A. Perwuelz, P. Mondon, and C. Caze. Experimental study of capillary flow in yarns. *Textile Research Journal*, 70(4):333–339, 2000.

[229] P. B. Petersen and R. J. Saykally. On the nature of ions at the liquid water surface. *Annual Review of Physical Chemistry*, 57(1):333–364, 2006.

[230] I. Pethes. A comparison of classical interatomic potentials applied to highly concentrated aqueous lithium chloride solutions. *Journal of Molecular Liquids*, 242:845 – 858, 2017.

[231] P. G. Petrov and J. G. Petrov. Comparison of the static and dynamic contact angle hysteresis at low velocities of the three-phase contact line. *Colloids and Surfaces*, 61(0):227 – 240, 1991.

[232] V.-N. Phan, C. Yang, and N.-T. Nguyen. Analysis of capillary filling in nanochannels with electroviscous effects. *Microfluidics and Nanofluidics*, 7(4):519, Jan 2009.

[233] F. Pirani, S. Brizi, L. F. Roncaratti, P. Casavecchia, D. Cappelletti, and F. Vecchiocattivi. Beyond the lennard-jones model: a simple and accurate potential function probed by high resolution scattering data useful for molecular dynamics simulations. *Phys. Chem. Chem. Phys.*, 10:5489–5503, 2008.

[234] M. N. Popescu, J. Ralston, and R. Sedev. Capillary rise with velocity-dependent dynamic contact angle. *Langmuir*, 24(21):12710, 2008.

[235] M. R. Powell, L. Cleary, M. Davenport, K. J. Shea, and Z. S. Siwy. Electric-field-induced wetting and dewetting in single hydrophobic nanopores. *Nature Nanotechnology*, 6:798, 2011.

[236] H. Pradeep and G. K. Rajanikant. Nanochannels: biological channel analogues. *IET Nanobiotechnology*, 6(2):63–70, 2012.

[237] S. Prakash, T. M. Long, J. C. Selby, J. S. Moore, and M. A. Shannon. 'click' modification of silica surfaces and glass microfluidic channels. *Anal. Chem.*, 79:1601–1667, 2007.

[238] S. Prakash, A. Piruska, E. N. Gatimu, P. W. Bohn, J. V. Sweedler, and M. A. Shannon. Nanofluidics: Systems and applications. *IEEE Sens. Journal*, 8(5):441–450, 2008.

[239] S. Prakash, H. A. Zambrano, K. K. Rangharajan, N. Rosenthal-Kim, Emilyand Vasquez, and A. T. Conlisk. Electrokinetic transport of monovalent and divalent cations in silica nanochannels. *Microfluidics and Nanofluidics*, 20(1):8, Jan 2016.

[240] T. Prasanna. Physical meaning of the ewald sum method. *Philosophical Magazine Letters*, 92(1):29–37, 2012.

[241] Z. Qian, Z. Fu, and G. Wei. Influence of electric fields on the structure and structure transition of water confined in a carbon nanotube. *J. Comput. Phys.*, 140(15):1–5, 2014.

[242] R. Qiao and N. R. Aluru. Charge inversion and flow reversal in a nanochannel electro-osmotic flow. *Phys. Rev. Lett.*, 92(19):1–4, 2004.

[243] R. Qiao and N. R. Aluru. Surface-charge-induced asymmetric electrokinetic transport in confined silicon nanochannels. *Appl. Phys. Lett.*, 86(14):1–3, 2005.

[244] D. Quere, , E. Raphael, and J.-Y. Ollitrault. Rebounds in a capillary tube. *Europhys. Lett.*, 15(10):3679–3682, 1999.

[245] D. Quere. Inertial capillarity. *Europhys. Lett.*, 39(5):533–538, 1997.

[246] K. Raidongia and J. Huang. Nanofluidic ion transport through reconstructed layered materials. *Journal of the American Chemical Society*, 134(40):16528–16531, 2012. PMID: 22998077.

[247] D. C. Rapaport. *The Art of Molecular Dynamics Simulation*. Cambridge University Press, New York, NY, USA, 1996.

[248] M. Rauscher and S. Dietrich. Wetting phenomena in nanofluidics. *Annu. Rev. Mater. Res.*, 38:143–172, 2008.

[249] R. Reale, N. J. English, P. Marracino, M. Liberti, and F. Apollonio. Dipolar response and hydrogen-bond kinetics in liquid water in square-wave time-varying electric fields. *Mol. Phys.*, 112(14):1870–1878, 2014.

[250] C. J. Ridgway, P. A. C. Gane, and J. Schoelkopf. Effect of capillary element aspect ratio on the dynamic imbibition within porous networks. *J. Coll. Interface Sci.*, 252(2):373–382, 2002.

[251] R. Riehn and R. H. Austin. Wetting micro- and nanofluidic devices using supercritical water. *Analytical Chemistry*, 78(16):5933–5934, 2006.

[252] W. J. Rieter, K. M. L. Taylor, and W. Lin. Surface modification and functionalization of nanoscale metal-organic frameworks for controlled release and luminescence sensing. *Journal of the American Chemical Society*, 129(32):9852–9853, 2007. PMID: 17645339.

[253] K. Ritos, M. K. Borg, N. J. Mottram, and J. M. Reese. Electric fields can control the transport of water in carbon nanotubes. 374(2060), 2015.

[254] F. Romer, A. Lervik, and F. Bresme. Nonequilibrium molecular dynamics simulations of the thermal conductivity of water: A systematic investigation of the spc/e and tip4p/2005 models. *J. Chem. Phys.*, 137:074503, 2012.

[255] S. Romero-Vargas, N. Giovambattista, I. A. Aksay, and P. G. Debenedetti. Effect of surface polarity on the structure and dynamics of water in nanoscale confinement. *J. Phys. Chem. B*, 113:1438–1446, 2009.

[256] J. S. Rowlinson and B. Widom. *Molecular theory of capillarity*. Oxford University Press, Clarendon,Oxford, 2nd edition, 1982.

[257] J. P. Ryckaert, G. Ciccotti, and H. J. C. Berendsen. Numerical integration of the cartesian equations of motion of a system with constraints: molecular dynamics of *n*-alkanes. *J. Comput. Phys.*, 23:327–341, 1977.

[258] M. Sadeghi-Goughari, S. Jeon, and H.-J. Kwon. Effects of magnetic-fluid flow on structural instability of a carbon nanotube conveying nanoflow under a longitudinal magnetic field. *Physics Letters A*, 2017.

[259] R. J. Sadus. *Molecular Simulation of Fluids: Theory, Algorithms and Object-Orientation*. Elsevier Science Inc., New York, NY, USA, 1999.

[260] A. M. Saitta, F. Saija, and P. V. Giaquinta. Ab initio molecular dynamics study of dissociation of water under an electric field. *Phys. Rev. Lett.*, 108:207801, May 2012.

[261] A. Salis and B. W. Ninham. Models and mechanisms of hofmeister effects in electrolyte solutions, and colloid and protein systems revisited. *Chem. Soc. Rev.*, 43:7358–7377, 2014.

[262] J. Schlitter, M. Engels, P. Kruger, E. Jacoby, and A. Wollmer. Targeted molecular dynamics simulation of conformational change-application to the t r transition in insulin. *Molecular Simulation*, 10(2-6):291–308, 1993.

[263] J. Schmidt, S. Roberts, J. Loparo, A. Tokmakoff, M. Fayer, and J. Skinner. Are water simulation models consistent with steady-state and ultrafast vibrational spectroscopy experiments? *Chemical Physics*, 341(1):143 – 157, 2007.

[264] A. Schultz, I. Papautsky, and J. Heikenfeld. Investigation of laplace barriers for arrayed electrowetting lab-on-a-chip. *Langmuir*, 30(18):5349–5356, 2014. PMID: 24738982.

[265] J. E. Seebergh and J. C. Berg. Dynamic wetting in the low capillary number regime. *Chem. Eng. Sci.*, 47(17):4455 – 4464, 1992.

[266] B. Shapiro, H. Moon, R. L. Garrell, and C.-J. im. Equilibrium behavior of sessile drops under surface tension, applied external fields, and material variations. *Journal of Applied Physics*, 93(9):5794–5811, 2003.

[267] A. Siebold, M. Nardin, J. Schultz, A. Walliser, and M. Oppliger. Effect of dynamic contact angle on capillary rise phenomena. *Coll. Surf. A*, 161:81–87, 2000.

[268] P. M. Sinha, G. Valco, S. Sharma, X. Liu, and M. Ferrari. Nanoengineered device for drug delivery application. *Nanotechnology*, 15(10):S585, 2004.

[269] S. W. Siu and R. A. Böckmann. Electric field effects on membranes: Gramicidin a as a test ground. *Journal of Structural Biology*, 157(3):545 – 556, 2007. Advances in Molecular Dynamics Simulations.

[270] F. H. Song, B. Q. Li, and Y. Li. Dynamic spreading of a nanosized droplet on a solid in an electric field. *Phys. Chem. Chem. Phys.*, 17:5543–5546, 2015.

[271] F. H. Song, B. Q. Li, and C. Liu. Molecular dynamics simulation of nanosized water droplet spreading in an electric field. *Langmuir*, 29(13):4266–4274, 2013. PMID: 23488748.

[272] Y. Song and L. L. Dai. The shear viscosities of common water models by non-equilibrium molecular dynamics simulations. *Molecular Simulation*, 36(7-8):560–567, 2010.

[273] W. Sparreboom, A. van den Berg, and J. C. T. Eijkel. Transport in nanofluidic systems: a review of theory and applications. *New J. Phys.*, 12:015004, 2010.

[274] R. Srivastava, J. K. Singh, and P. T. Cummings. Effect of electric field on water confined in graphite and mica pores. *The Journal of Physical Chemistry C*, 116(33):17594–17603, 2012.

[275] A. G. Stack and J. R. Rustad. Structure and dynamics of water on aqueous barium ion and the 001 barite surface. *The Journal of Physical Chemistry C*, 111(44):16387–16391, 2007.

[276] L. J. Steinbock, O. Otto, C. Chimerel, J. Gornall, and U. F. Keyser. Detecting dna folding with nanocapillaries. *Nano Letters*, 10(7):2493–2497, 2010. PMID: 20515038.

[277] I. V. Stiopkin, C. Weeraman, P. A. Pieniazek, F. Y. Shalhout, J. L. Skinner, and A. V. Benderskii. Hydrogen bonding at the water surface revealed by isotopic dilution spectroscopy. *Nature*, 474:192–195, 2005.

[278] G. Stirnemann, S. Romero-Vargas Castrillon, J. T. Hynes, P. J. Rossky, P. G. Debenedetti, and D. Laage. Non-monotonic dependence of water reorientation dynamics on surface hydrophilicity: Competing effects of the hydration structure and hydrogen-bond strength. *Phys. Chem. Chem. Phys.*, 13(19):911–917, 2011.

[279] Stoberg.W. Hydrodynamics of capillary imbibition under nanoconfinements. *J. Am. Chem. Soc.*, 28(22):14488–14495, 2012.

[280] M. R. Stukan, P. Ligneul, J. P. Crawshaw, and E. S. Boek. Spontaneous imbibition in nanopores of different roughness and wettability. *Langmuir*, 26(16):13342–13352, 2010. PMID: 20695576.

[281] J. W. Suk and J.-H. Cho. Capillary flow control using hydrophobic patterns. *Journal of Micromechanics and Microengineering*, 17(4):N11, 2007.

[282] X. Sun, T. Lin, and J. D. Gezelter. Langevin dynamics for rigid bodies of arbitrary shape. *The Journal of Chemical Physics*, 128(23):234107, 2008.

[283] A. P. Sunda and A. Venkatnathan. Parametric dependence on shear viscosity of spc/e water from equilibrium and non-equilibrium molecular dynamics simulations. *Molecular Simulation*, 39(9):728–733, 2013.

[284] S. Supple and N. Quirke. Rapid imbibition of fluids in carbon nanotubes. *Phys. Rev. Lett.*, 90(21):214501, 2003.

[285] I. M. Svishchev and P. G. Kusalik. Crystallization of liquid water in a molecular dynamics simulation. *Phys. Rev. Lett.*, 73(7):975–979, 1994.

[286] J. Szekely, A. W. Neumann, and Y. K. Chuang. The rate of capillary penetration and the applicability of the washburn equation. *J. Coll. Interface Sci.*, 35(2):273–278, 1970.

[287] J. Szekely, A. W. Neumann, and Y. K. Chuang. The rate of capillary penetration and the applicability of the washburn equation. *J. Coll. Interface Sci.*, 35(2):273–278, 1971.

[288] N. R. Tas, J. Haneveld, H. V. Jansen, M. Elwenspoek, and A. van den Berg. Capillary filling speed of water in nanochannels. *Appl. Phys. Lett.*, 85(15):3274–3276, 2004.

[289] Y. Temiz, R. D. Lovchik, G. V. Kaigala, and E. Delamarche. Lab on a chip devices: How to close and plug the lab. *Microelectronic Engineering*, 132:156 – 175, 2015. Micro and Nanofabrication Breakthroughs for Electronics, MEMS and Life Sciences.

[290] L. H. Thamdrup, F. Persson, H. Bruus, A. Kristensen, and H. Flyvbjerg. Experimental investigation of bubble formation during capillary filling of SiO_2 nanoslits. *Appl. Phys. Lett.*, 91:163505, 2007.

[291] A. P. Thompson. Nonequilibrium molecular dynamics simulation of electroosmotic flow in a charged nanopore. *J. Comput. Phys.*, 119(14):7503–7511, 2003.

[292] J. T. Titantah and M. Karttunen. Water dynamics: Relation between hydrogen bond bifurcations, molecular jumps, local density amp; hydrophobicity. *Scientific Reports*, 3(4), 2013.

[293] G. Tocci, L. Joly, and A. Michaelides. Friction of water on graphene and hexagonal boron nitride from ab initio methods: Very different slippage despite very similar interface structures. *Nano Letters*, 14(12):6872–6877, 2014. PMID: 25394228.

[294] A. Y. Toukmaji and J. A. Board. Ewald summation techniques in perspective: a survey. *Computer Physics Communications*, 95(2):73 – 92, 1996.

[295] S. Toxvaerd and J. C. Dyre. Communication: Shifted forces in molecular dynamics. *The Journal of Chemical Physics*, 134(8):081102, 2011.

[296] K. P. Travis and K. E. Gubbins. Poiseuille flow of Lennard-Jones fluids in narrow slit pores. *J. Chem. Phys.*, 112(4):1984–1994, 2000.

[297] S. Tsuneyuki, M. Tsukada, H. Aoki, and Y. Matsui. First-principles interatomic potential of silica applied to molecular dynamics. *Phys. Rev. Lett.*, 61(7):869–874, 1988.

[298] M. Tuckerman. *Statistical Mechanics: Theory and Molecular Simulation*. Oxford graduate texts. Oxford University Press, 2011.

[299] D. L. Turner. Proton and deuteron exchange rates in water measured by oxygen-17 n.m.r. *Molecular Physics*, 40(4):949–957, 1980.

[300] T. G. Twardeck. Effect of parameter variations on drop placement in an electrostatic ink jet printer. *IBM Journal of Research and Development*, 21(1):31–36, Jan 1977.

[301] S. Vaitheeswaran, H. Yin, and J. C. Rasaiah. Water between plates in the presence of an electric field in an open system. *The Journal of Physical Chemistry B*, 109(14):6629–6635, 2005.

[302] D. Van Der Spoel, E. Lindahl, B. Hess, G. Groenhof, A. E. Mark, and H. J. C. Berendsen. Gromacs: Fast, flexible, and free. *Journal of Computational Chemistry*, 26(16):1701–1718, 2005.

[303] D. van der Spoel, P. J. van Maaren, and H. J. C. Berendsen. A systematic study of water models for molecular simulation: Derivation of water models optimized for use with a reaction field. *J. Chem. Phys.*, 108(24):10220–10230, 1998.

[304] J. W. van Honschoten, N. Brunets, and N. R. Tas. Capillarity at the nanoscale. *Chem. Soc. Rev.*, 39:1096–1114, 2010.

[305] E. Vanden-Eijnden and G. Ciccotti. Second-order integrators for langevin equations with holonomic constraints. *Chemical Physics Letters*, 429(1):310 – 316, 2006.

[306] C. Vega and E. de Miguel. Surface tension of the most popular models of water by using the test-area simulation method. *The Journal of Chemical Physics*, 126(15):154707, 2007.

[307] A. Vegiri and S. V. Schevkunov. A molecular dynamics study of structural transitions in small water clusters in the presence of an external electric field. *J. Chem. Phys.*, 115(9):4175–4185, 2001.

[308] A. Vellaichamy, J. C. Tran, A. D. Catherman, J. E. Lee, J. F. Kellie, S. M. M. Sweet, L. Zamdborg, P. M. Thomas, D. R. Ahlf, K. R. Durbin, G. A. Valaskovic, and N. L. Kelleher. Size-sorting combined with improved nanocapillary liquid chromatographymass spectrometry for identification of intact proteins up to 80 kda. *Analytical Chemistry*, 82(4):1234–1244, 2010.

[309] S. Villette, M. P. Valignat, A. M. Cazabat, L. Jullien, and F. Tiberg. Wetting on the molecular scale and the role of water. a case study of wetting of hydrophilic silica surfaces. *Langmuir*, 12:825–830, 1996.

[310] T. Q. Vo and B. Kim. Transport phenomena of water in molecular fluidic channels. *Scientific Reports*, 6:33881, 2016.

[311] T. Vo-Dinh, B. M. Cullum, and D. L. Stokes. Nanosensors and biochips: frontiers in biomolecular diagnostics. *SAB*, 74(1-3):2–11, 2001.

[312] O. V. Voinov. Hydrodynamics of wetting. *Fluid Dyn.*, 11(5):714–721, 1976.

[313] O. V. Voinov. Asymptotic laws of wetting hydrodynamics. *Doklady Physics*, 50(7):380–384, Jul 2005.

[314] E. Wagemann, E. Oyarzua, J. H. Walther, and H. A. Zambrano. Slip divergence of water flow in graphene nanochannels: the role of chirality. *Phys. Chem. Chem. Phys.*, 19:8646–8652, 2017.

[315] J. H. Walther, R. Jaffe, T. Halicioglu, and P. Koumoutsakos. Carbon nanotubes in water: Structural characteristics and energetics. *J. Phys. Chem. B*, 105:9980–9987, 2001.

[316] J. H. Walther, T. Werder, R. L. Jaffe, and P. Koumoutsakos. Hydrodynamic properties of carbon nanotubes. *Phys. Rev. E*, 69:062201, 2004.

[317] Z. Wang, D. L. Olmsted, M. Asta, and B. B. Laird. Electric potential calculation in molecular simulation of electric double layer capacitors. *Journal of Physics: Condensed Matter*, 28(46):464006, 2016.

[318] V. B. Warshavsky and X. C. Zeng. Effect of an electric field on the surface tension of a dipolar-quadrupolar fluid and its implication for sign preference in droplet nucleation. *Phys. Rev. Lett.*, 89:246104, Nov 2002.

[319] E. W. Washburn. The dynamics of capillary flow. *Phys. Rev.*, 17(3):273–283, 1921.

[320] K. M. Weerakoon-Ratnayake, C. E. O'Neil, F. I. Uba, and S. A. Soper. Thermoplastic nanofluidic devices for biomedical applications. *Lab Chip*, 17:362–381, 2017.

[321] J. H. Weijs, B. Andreotti, and J. H. Snoeijer. Elasto-capillarity at the nanoscale: on the coupling between elasticity and surface energy in soft solids. *Soft Matter*, 9:8494–8503, 2013.

[322] J. H. Weijs, A. Marchand, B. Andreotti, D. Lohse, and J. H. Snoeijer. Origin of line tension for a lennard-jones nanodroplet. *Physics of Fluids*, 23(2):022001, 2011.

[323] B. A. Wells and A. L. Chaffee. Ewald summation for molecular simulations. *Journal of Chemical Theory and Computation*, 11(8):3684–3695, 2015.

[324] T. Werder, J. H. Walther, R. Jaffe, T. Halicioglu, F. Noca, and P. Koumoutsakos. Molecular dynamics simulations of contact angles of water droplets in carbon nanotubes. *Nano Lett.*, 1(12):697–702, 2001.

[325] Winarto, D. Takaiwa, E. Yamamoto, and K. Yasuoka. Structures of water molecules in carbon nanotubes under electric fields. *The Journal of Chemical Physics*, 142(12):124701, 2015.

[326] M. Wisniewska. The structure of electrical double layer of silica in the presence of polyvinyl alcohol (pva) at different temperatures. *Materials Letters*, 64:1611–1613, 2010.

[327] D. Wolf, V. Yamakov, S. Phillpot, A. Mukherjee, and H. Gleiter. Deformation of nanocrystalline materials by molecular-dynamics simulation: relationship to experiments? *Acta Materialia*, 53(1):1 – 40, 2005.

[328] B. Wolfrum, E. Kätelhön, A. Yakushenko, K. J. Krause, N. Adly, M. Hüske, and P. Rinklin. Nanoscale electrochemical sensor arrays: Redox cycling amplification in dual-electrode systems. *Accounts of Chemical Research*, 49(9):2031–2040, 2016. PMID: 27602780.

[329] C. Wu, T. G. Lin, Y. Zhan, Zhikun andLi, S. C. Tung, and W. J. Li. Fabrication of all-transparent polymer-based and encapsulated nanofluidic devices using nano-indentation lithography. *Microsystems Amp Nanoengineering*, 3(16084), 2017.

[330] K. Wu, Z. Chen, J. Li, X. Li, J. Xu, and X. Dong. Wettability effect on nanoconfined water flow. *Proc. Natl. Acad. Sci. USA*, 114(13):3358–3363, 2017.

[331] X. Xia and M. L. Berkowitz. Electric-field induced restructuring of water at a platinum-water interface: A molecular dynamics computer simulation. *Phys. Rev. Lett.*, 74(16):3193–3196, 1995.

[332] K. Xiao, Y. Zhou, X.-Y. Kong, G. Xie, P. Li, Z. Zhang, L. Wen, and L. Jiang. Electrostatic-charge- and electric-field-induced smart gating for water transportation. *ACS Nano*, 10(10):9703–9709, 2016.

[333] Q. Xie, M. A. Alibakhshi, S. Jiao, Z. Xu, M. Hempel, J. Kong, H. G. Park, and C. Duan. Fast water transport in graphene nanofluidic channels. *Nature*, 13(3):238–246, 2018.

[334] W. J. Xie and Y. Q. Gao. A simple theory for the hofmeister series. *The Journal of Physical Chemistry Letters*, 4(24):4247–4252, 2013. PMID: 26296173.

[335] Y. Xue, J. Markmann, H. Duan, J. Weissmüller, and P. Huber. Switchable imbibition in nanoporous gold. *Nature Communications*, 5(4237), 2014.

[336] D. Yang, M. Krasowska, C. Priest, M. N. Popescu, and J. Ralston. Dynamics of capillary-driven flow in open microchannels. *J. Phys. Chem. C*, 115(38):18761–18769, 2011.

[337] Y. Yang, C. Thompson, V. Anderson, and A. Wood. A statistical mechanical model of cell membrane ion channels in electric fields: The mean-field approximation. *Physica A: Statistical Mechanics and its Applications*, 268(3):424 – 432, 1999.

[338] Z. Yao, J.-S. Wang, G.-R. Liu, and M. Cheng. Improved neighbor list algorithm in molecular simulations using cell decomposition and data sorting method. *Computer Physics Communications*, 161(1):27 – 35, 2004.

[339] I.-C. Yeh and M. L. Berkowitz. Dielectric constant of water at high electric fields: Molecular dynamics study. *The Journal of Chemical Physics*, 110(16):7935–7942, 1999.

[340] I.-C. Yeh and G. Hummer. System-size dependence of diffusion coefficients and viscosities from molecular dynamics simulations with periodic boundary conditions. *The Journal of Physical Chemistry B*, 108(40):15873–15879, 2004.

[341] T.-H. Yen. Investigation of the effects of perpendicular electric field and surface morphology on nanoscale droplet using molecular dynamics simulation. *MS*, 38(6):509–517, 2012.

[342] H. A. Zambrano, N. Vasquez, and E. Wagemann. Wall embedded electrodes to modify electroosmotic flow in silica nanoslits. *Phys. Chem. Chem. Phys.*, 18:1202–1211, 2016.

[343] H. A. Zambrano, J. H. Walther, and R. L. Jaffe. Molecular dynamics simulations of water on a hydrophilic silica surface at high air pressures. *J. Mol. Liq.*, pages –, 2014. In Press.

[344] H. A. Zambrano, J. H. Walther, P. Koumoutsakos, and I. F. Sbalzarini. Thermophoretic motion of water nanodroplets confined inside carbon nanotubes. *Nano Lett.*, 9(1):66–71, 2009.

[345] A. A. Zavitsas. Aqueous solutions of calcium ions: hydration numbers and the effect of temperature. *The Journal of Physical Chemistry B*, 109(43):20636–20640, 2005. PMID: 16853671.

[346] H. Zhang, A. A. Hassanali, Y. K. Shin, C. Knight, and S. J. Singer. The water-amorphous silica interface: Analysis of the stern layer and surface conduction. *J. Comput. Phys.*, 134:1–13, 2011.

[347] Y. Zhang, A. Otani, and E. J. Maginn. Reliable viscosity calculation from equilibrium molecular dynamics simulations: A time decomposition method. *Journal of Chemical Theory and Computation*, 11(8):3537–3546, 2015. PMID: 26574439.

[348] Q.-N. Zheng, X.-H. Liu, X.-R. Liu, T. Chen, H.-J. Yan, Y.-W. Zhong, D. Wang, and L.-J. Wan. Bilayer molecular assembly at a solid/liquid interface as triggered by a mild electric field. *Angewandte Chemie International Edition*, 53(49):13395–13399, 2014.

[349] B. Zhmud, F. Tiberg, and K. Hallstensson. Dynamics of capillary rise. *J. Coll. Interface Sci.*, 228:263–269, 2000.

[350] J. Zhou, X. Lu, Y. Wang, and J. Shi. Molecular dynamics study on ionic hydration. *Fluid Phase Equilibria*, 194-197:257 – 270, 2002. Proceedings of the Ninth International Conference on Properties and Phase Equilibria for Product and Process Design.

[351] Y. Zhu, X. Lu, H. Ding, and Y. Wang. Hydration and association of alkaline earth metal chloride aqueous solution under supercritical condition. *Molecular Simulation*, 29(12):767–772, 2003.

[352] D. Zong, H. Hu, Y. Duan, and Y. Sun. Viscosity of water under electric field: Anisotropy induced by redistribution of hydrogen bonds. *The Journal of Physical Chemistry B*, 120(21):4818–4827, 2016.

[353] D. Zong, Z. Yang, and Y. Duan. Wettability of a nano-droplet in an electric field: A molecular dynamics study. *Applied Thermal Engineering*, 122:71 – 79, 2017.